EFFECTS OF SURFACE CHEMISTRY AND SIZE ON IRON OXIDE NANOPARTICLE DELIVERY OF OLIGONUCLEOTIDES

A Dissertation
Presented to
The Academic Faculty

by

Christopher Shen

In Partial Fulfillment
of the Requirements for the Degree
Doctor of Philosophy in the
School of Biomedical Engineering

Georgia Institute of Technology
May 2011

EFFECTS OF SURFACE CHEMISTRY AND SIZE ON IRON OXIDE NANOPARTICLE DELIVERY OF OLIGONUCLEOTIDES

Approved by:

Dr. Shuming Nie, Advisor
School of Biomedical Engineering
Georgia Institute of Technology

Dr. Philip Santangelo
School of Biomedical Engineering
Georgia Institute of Technology

Dr. Ravi Bellamkonda
School of Biomedical Engineering
Georgia Institute of Technology

Dr. Lily Yang
Department of Surgery
Emory University

Dr. Mark Prausnitz
School of Chemical and Biomolecular Engineering
Georgia Institute of Technology

Date Approved: Mar. 14, 2011

To Mom, Dad, Annie

ACKNOWLEDGEMENTS

The work in this dissertation is the culmination of years of not only hard work but also much personal and professional growth. I am indebted to my advisor Dr. Shuming Nie for giving me the opportunity to learn from him. His experience, support, faith, and encouragement have made this dissertation possible. I have learned much during my time in graduate school under his direction and for this I am very appreciative.

I have also received help from a number of former and current lab members. Drs. Yun Xing and Jian Liu worked with me in my initial imaging and profiling studies when I joined the lab. Dr. Xingguang Su was a visiting professor with whom I shared an office for a year. I appreciate her mentorship, friendship and opportunity to practice my Mandarin. I worked together with Dr. Tushar Sathe in the magnetic bead assays and was fortunate enough to spend considerable time with him. I count him as a co-worker, friend, and mentor. Isaac Johnson also assisted in the magnetic bead experiments. Anthony Nicolini and Drs. Hongwei Duan and Min Kuang provided great help in my drug delivery studies. I have had the opportunity to interact with my other labmates—Dr. Aaron Mohs, Dr. Andrew Smith, Dr. Brad Kairdolf, Dr, Hongwei Chen, Dr. Kate Lee, Mary Wen, Dr. Michael Mancini, Shefaet Rahman, Dr. Xi Zhou, Dr. Xiaohua Huang, Dr. Ximei Qian, Dr. Ying Wang, Dr. Yiqing Wang—in one way or another. They have all been a great group of individuals to work with. It was an honor to be numbered among them.

I owe Dr. Hong Yi and Dr. Songli Xu many thanks for their assistance with the TEM and confocal microscope, respectively. Dr. Gary Bassell and Dr. Christina

Gross from Emory Cell Biology also were generous enough to give me training in *in situ* hybridization techniques.

Michelle Denney has worked tirelessly to keep our lab in running order as Program Coordinator. She has always been very prompt in responding to emails, coordinating lab events, and keeping our labs well stocked.

I would also like to thank the TI:GER program at the Georgia Tech College of Management, and in particular Dr. Anne Rector, Margi Berbari, and Dr. Marie Thursby. I learned a lot from the program and it was enriching to gain an additional perspective on technology beyond the work scientists do at the bench. I appreciate their mentorship and professional development.

I thank my home meeting and all the saints for their care, meals, prayer, and portion of Christ.

Lastly, I must thank my family: my mother, Aris, father, Ted, and sister, Annie, have all been a tremendous support from visits, phone calls, to care packages. My parents, in particular, have paid many a literal and figurative price to provide me and my sister an excellent education and upbringing. I am deeply indebted to all their sacrifice, love, and support.

TABLE OF CONTENTS

LIST OF TABLES

LIST OF FIGURES

LIST OF SYMBOLS AND ABBREVIATIONS

2A	Secondary Amine
3A	Tertiary Amine
BCAR3	Breast Cancer Antiestrogen Resistance-3
BSA	Bovine Serum Albumin
c_T	Cycle Threshold
C	Degree Celcius
CCD	Charge-Coupled Device
CdS	Cadmium Sulfide
CdSe	Cadmium Selenide
CNA	Circulating Nucleic Acids
CO_2	Carbon Dioxide
DAPI	4',6-diamidino-2-phenylindole
DDC	N,N'-dicyclohexylcarbodiimide
DLS	Dynamic Light Scattering
DMAP	4-(dimethylamino)pyridine
DNA	Deoxyribonucleic Acid
DPTA	N,N-Dimethyldipropylenetriamine
EDC	1-Ethyl-3-(3-dimethylaminopropyl)carbodiimide
FDA	Food and Drug Administration
FDNA	Fluorescently-labeled DNA
FISH	Fluorescence In Situ Hybridization
FLNA	Fluorescently-Labeled Antagomir
HCl	Hydrochloric Acid

I	Imidazole
IHC	Immunohistochemistry
InAs	Indium Arsenide
InP	Indium Phosphide
IO	Iron Oxide
mRNA	Messenger RNA
miRNA	MicroRNA
MMB	Magnetic Microbead
MOPS	3-(N-morpholino)propanesulfonic acid
MRI	Magnetic Resonance Imaging
NaCl	Sodium Chloride
NaN_3	Sodium Azide
NaOH	Sodium Hydroxide
NCI	National Cancer Institute
NdFeB	Neodymium Magnet
NIH	National Institutes of Health
NTC	No Transfecton Control
ODE	Octadecene
ODA	Octadecylamine
PBS	Phosphate Buffered Saline
PbSe	Lead Selenide
PCR	Polymerase Chain Reaction
pDNA	Plasmid DNA
PEG	Polyethylene Glycol
PEI	Polyethyleneimine
pK_a	Acid Dissociation Constant at Logarithmic Scale

PLGA	Poly(lactic-co-glycolic acid)
pri-miRNA	Primary MicroRNA
QD	Quantum Dot
RES	Reticuloendothelial System
RISC	
RNA	Ribonucleic Acid
RNAi	RNA Interference
siRNA	Small Interfering RNA
SSC	Saline-Sodium Citrate
SNR	Signal to Noise Ratio
SPION	Superparamagnetic Iron Oxide Nanoparticles
TBE	Tris Borate EDTA
TEM	Transmission Electron Microscope
tRNA	Transfer RNA
V	Volts
ZnS	Zinc Sulfide

SUMMARY

The discovery of RNA interference and the increasing understanding of disease genetics have created a new class of potential therapeutics based on oligonucleotides. This therapeutic class includes antisense molecules, small interfering RNA (siRNA), and microRNA modulators such as antagomirs (antisense directed against microRNA) and microRNA mimics, all of which function by altering gene expression at the translational level. While these molecules have the promise of treating a host of diseases from neurological disorders to cancer, a major hurdle is their inability to enter cells on their own, where they may render therapeutic effect. Nanotechnology is the engineering of materials at the nanometer scale and has gained significant interest for nucleic acid delivery due to its biologically relevant length-scale and amenability to multifunctionality. While a number of nanoparticle vehicles have shown promise for oligonucleotide delivery, there remains a lack of understanding of how nanoparticle coating and size affect these delivery processes. This dissertation seeks to elucidate some of these factors by evaluating oligonucleotide delivery efficiencies of a panel of iron oxide nanoparticles with varying cationic coatings and sizes. A panel of uniformly-sized nanoparticles was prepared with surface coatings comprised of various amine groups representing high and low pK_as. A separate panel of nanoparticles with sizes of 40, 80, 150, and 200 nm but with the same cationic coating was also prepared.

Results indicated that both nanoparticle surface coating and nanoparticle hydrodynamic size affect transfection efficiency. Specific particle coatings and sizes were identified that gave superior performance. The intracellular fate of iron oxide

nanoparticles was also tracked by electron microscopy and suggests that they function via the proton sponge effect. The research presented in this dissertation may aid in the rational design of improved nanoparticle delivery vectors for nucleic acid-based therapy.

CHAPTER 1

INTRODUCTION

1.1 Motivation

Cancer remains one of the world's most devastating diseases, with more than 10 million new cases every year [1, 2]. In the United States, it is the second greatest killer, outpaced only by cardiovascular disease, and represents an annual economic burden of over $228 billion [3]. While the death of rate due to other common killers such as heart diseases, cerebrovascular diseases, pneumonia/influenza, has dropped precipitously over the past 50 years, there has been relatively little progress in battling cancer deaths.

This may be due in part to the enormous complexity of the disease. Cancer is caused by uncontrolled proliferation and the inappropriate survival of damaged cells, which results in tumor formation. Control of the processes of cell division, differentiation and death, however, is coordinated by a large number of regulatory factors, damage to whose genes (also known as oncogenes and tumor suppressor genes) is selected for in cancer [4]. This genetic damage is by no means homogeneous; it can involve many different mutations on many different genes. In addition, disease results not from any single mutation but from the gradual accumulation of genetic damage. The somatic acquisition of large numbers of mutations coupled with the variability in the host's genetic constitution produces a disease of enormous heterogeneity and complexity—so much so that it may not be an exaggeration to suggest that 100 breast cancer patients represent 100 distinct diseases [5].

This complex genetic nature of cancer suggests that traditional methods of characterizing tumors by gross visual information—such as size of tumor, degree of spread, general histological characterization, along with limited biochemical assays—and traditional methods of treatment—such as broad exposure to cytotoxic chemotherapeutics—is inadequate. The success of new methods that dissect cancer heterogeneity by assaying a panel of genetic biomarkers for personalized and more accurate disease diagnosis/prognosis, and the success of new biologic drugs that treat cancer with molecular specificity, underscore the importance of genetomolecular analysis and intervention [6-12].

Nucleic acids represent important diagnostic and therapeutic biomolecular targets in cancer. Studies have shown that cancer-related cell-free DNA can be detected in blood and other biological fluids as a noninvasive method for cancer diagnosis and profiling [13, 14]. RNA-based profiling has also shown promise in classifying cancers into clinically relevant subtypes [15, 16]. In the realm of therapeutics, siRNA and other oligonucleotide drugs seek to treat cancer by interacting directly with the genes responsible for disease progression [17, 18].

The potential use of nucleic acids for cancer applications is still limited by issues such as sensitivity, specificity, and effective delivery methods. Nanotechnology, which involves the engineering of materials at the nanoscale, promises to overcome these limitations. The size regime of nanotechnology is on the same scale as biologically relevant molecules and structures, enabling the design of materials that interact specifically with biology at a fundamental level. Unique properties of materials at the nanoscale that are not present in their bulk phases also present opportunities for improving sensitivity and specificity of biomedical assays and interventions [19].

1.2 Dissertation Organization

This dissertation will explore the use of two types of nanoparticles—semiconductor quantum dots and iron oxide nanoparticles—for nucleic acid-based assays. These technologies will be used for two specific applications: DNA detection in solution, which may be extended for noninvasive genetic analysis of biological fluids for cancer diagnosis and prognosis, and intracellular oligonucleotide delivery, which may yield insights in the use of nanotechnology for the clinical application of oligonucleotide drugs.

This dissertation has been organized into 7 chapters. This chapter has given a broad overview of cancer as a heterogeneous disease and presents some motivation for the development of new methods for the diagnosis and treatment of cancer.

Chapter 2 will provide some background on quantum dots and iron oxide nanoparticles, the two types of nanoparticles that will be explored in this dissertation for use in cancer applications. We will then describe the biological applications for which these technologies will be used: DNA detection and oligonucleotide delivery. For DNA detection, circulating DNA will be discussed as a target for detection. Its potential utility in the management of cancer throughout the treatment process will be developed. For oligonucleotide delivery, we will describe the tremendous promise oligonucleotide drugs present for the treatment of cancer as well as many other diseases, but also the limitation that currently exists in their widespread application: the need for a delivery vehicle.

Chapter 3 describes a method we have developed for detecting DNA sequences in an optical assay involving single magnetic microbeads coated with

quantum dots as a fluorescent reporter. The superior optical properties exhibited by QDs combined with the advantage of using magnetic beads for magnetic enrichment and isolation enable sensitive target detection.

Chapters 4, 5, and 6 will describe our investigation of iron oxide nanoparticles for delivery of antagomir, one type of oligonucleotide drug. We prepare a panel of 12 SPIONs all containing different amine coatings in Chapter 4. We describe our reaction procedure and characterize the prepared particles as well as their DNA binding properties.

In Chapter 5, we will use the 12 particles prepared in Chapter 4 to deliver antagomir to antagonize a cancer-related microRNA. Transfection efficiencies for the 12 particles are reported and we identify one that exhibits superior delivery. We also use one of these particles to study the intracellular delivery process through TEM and fluorescent imaging.

Chapter 6 evaluates how nanoparticle size affects intracellular antagomir transfection. We prepare SPIONs with diameters of 40, 80, 150, and 200nm and use them to transfect cells. Transfection efficiencies are reported as well as supporting data from TEM and fluorescence imaging experiments.

We close in Chapter 7 with conclusions from our studies and propose future directions based on these findings.

Appendix A will present data from the use of quantum dots for antagomir transfection, with may yield some insights when combined with the data presented in the body of this dissertation.

1.3 References

1. Peer, D., et al., *Nanocarriers as an emerging platform for cancer therapy.* Nature Nanotechnology, 2007. **2**(12): p. 751-760.

2. Stewart, B.W.K., P, *World Cancer Report*. 2003: Geneva.

3. *Cancer Facts and Figures 2009*. 2009, American Cancer Society: Atlanta, GA.

4. Esquela-Kerscher, A. and F.J. Slack, *Oncomirs - microRNAs with a role in cancer.* Nature Reviews Cancer, 2006. **6**(4): p. 259-269.

5. Nevins, J.R. and A. Potti, *Mining gene expression profiles: expression signatures as cancer phenotypes.* Nature Reviews Genetics, 2007. **8**(8): p. 601-609.

6. Simon, R., *Diagnostic and prognostic prediction using gene expression profiles in high-dimensional microarray data.* British Journal of Cancer, 2003. **89**(9): p. 1599-1604.

7. Sommer, A. and B. Haendler, *Androgen receptor and prostate cancer: Molecular aspects and gene expression profiling.* Current Opinion in Drug Discovery & Development, 2003. **6**(5): p. 702-711.

8. Yanagisawa K, X.B., Carbone DP and Caprioli RM, *Molecular Fingerprinting in Human Lung Cancer.* Clinical Lung Cancer, 2003(5): p. 113-118.

9. Golub, T.R., et al., *Molecular classification of cancer: Class discovery and class prediction by gene expression monitoring.* Science, 1999. **286**(5439): p. 531-537.

10. Alizadeh, A.A., et al., *Distinct types of diffuse large B-cell lymphoma identified by gene expression profiling.* Nature, 2000. **403**(6769): p. 503-511.

11. Yan, L., K. Hsu, and R.A. Beckman, *Antibody-based therapy for solid tumors.* Cancer Journal, 2008. **14**(3): p. 178-183.

12. Hurley, L.H., *DNA and its associated processes as targets for cancer therapy.* Nature Reviews Cancer, 2002. **2**(3): p. 188-200.

13. Dong, S.M., et al., *Detecting colorectal cancer in stool with the use of multiple genetic targets.* Journal of the National Cancer Institute, 2001. **93**(11): p. 858-865.

14. Fleischhacker, M. and B. Schmidt, *Circulating nucleic acids (CNAs) and cancer - A survey.* Biochimica Et Biophysica Acta-Reviews on Cancer, 2007. **1775**(1): p. 181-232.

15. Li, W.X., et al., *Diagnostic and prognostic implications of microRNAs in human hepatocellular carcinoma.* International Journal of Cancer, 2008. **123**(7): p. 1616-1622.

16. Lu, J., et al., *MicroRNA expression profiles classify human cancers.* Nature, 2005. **435**(7043): p. 834-838.

17. Behlke, M.A., *Progress towards in vivo use of siRNAs.* Molecular Therapy, 2006. **13**(4): p. 644-670.

18. Leung, R.K.M. and P.A. Whittaker, *RNA interference: from gene silencing to gene-specific therapeutics.* Pharmacology & Therapeutics, 2005. **107**(2): p. 222-239.

19. Nie, S.M., et al., *Nanotechnology applications in cancer.* Annual Review of Biomedical Engineering, 2007. **9**: p. 257-288.

CHAPTER 2

BACKGROUND

The promise of nanotechnology for both cancer detection and therapy is quite compelling. The length scale of nanoparticles is on the same order as many biological molecules such as DNA and large proteins, making them ideally suited to probe individual molecules and interact with biological processes on a fundamental level [1, 2]. Moreover, nanoparticles often exhibit unique properties that are not available in their bulk materials [2, 3]. These unique properties can make nanoparticles particularly advantageous for certain applications. Both quantum dots and iron oxide nanoparticles have already found important uses in imaging, diagnosis, and therapy. In this chapter, we provide a brief overview of QDs and iron oxide nanoparticles. We then introduce the fields of nucleic acid detection and oligonucleotide therapies, two areas where nanotechnology can be harnessed to improve human health.

2.1 Semiconductor Quantum Dots

Quantum dots (QDs) are semiconducting nanoparticles with unique optical properties which differ from their bulk material properties. They can be synthesized from various types of semiconductor material such as II-VI (e.g. CdS, CdSe), III-V (e.g. InP, InAs), or IV-VI (e.g. PbSe) [4]. CdSe QDs capped with a thin layer of ZnS are the most frequently used, however, for biological experiments as the band-gap energy of CdSe spans the visible region (400-800nm) of the electromagnetic spectrum [5-7]. Due to quantum confinement effects at the nanoscale, QDs may be

tuned by size or composition to emit light at varying wavelengths. They are very bright and photostable, being about 10-100 times brighter and 100-1000 times more photostable in comparison to organic dyes or fluorescent proteins [8]. Their broad, continuous absorption spectra and narrow emission spectra also allow for multiple colors to be simultaneously excited using a single excitation source (Figure 2.1). These properties enable QDs to be used for sensitive and quantitative multiplexed detection and make them ideal candidates for biomolecular imaging.

Indeed, QDs have been used for a variety of biological applications including immunohistochemistry, live cell imaging, drug delivery, and other bioanalytical assays requiring fluorescence [9-15]. Highlighting the unique features of these particles, Fountaine et al demonstrated the use of up to five different colored QDs for the simultaneous staining and imaging of five clinically relevant protein targets in cancer tissue [11]. The superior brightness and photostability of QDs also enabled Dahan et al to image the diffusion dynamics of single glycine receptors on neuronal membranes of living cells tagged by single quantum dots [16].

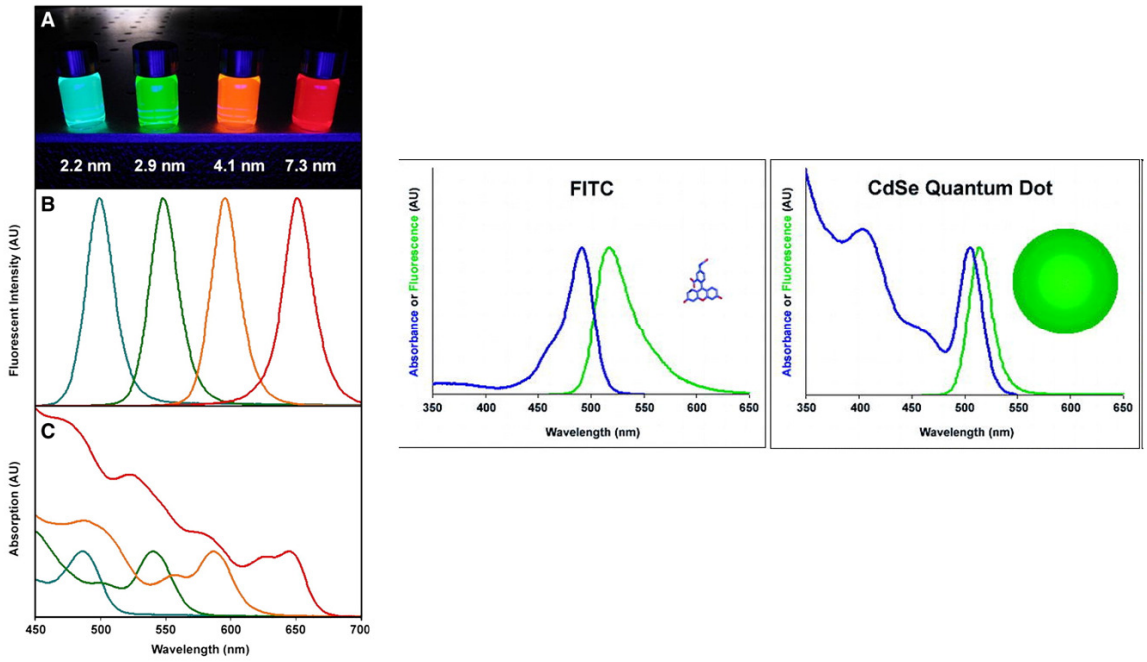

Figure 2.1: Spectral properties of quantum dots. Panel on left illustrates the size-dependent nature of QD fluorescence. Panel on right demonstrates superior optical properties of QDs relative to chemical dyes [17]. Note that the emission peak is more narrow and symmetric for the QD spectrum, and the absorption band extends far into the ultraviolet region. The size differences of FITC and QD are also shown [18].

2.2 Iron Oxide Nanoparticles

Iron oxide nanoparticles, also called superparamagnetic iron oxide nanoparticles (SPIONs) are another class of nanoparticles that offer attractive possibilities for biomedicine due to their unique properties. First, they are relatively nontoxic and have already been FDA approved for in vivo imaging as a magnetic resonance imaging (MRI) contrast agent [19]. Second, they can be synthesized over a relatively large size range, from a few nanometers up to tens of nanometers [19, 20]. Larger particles can be synthesized as clusters of smaller particles. Third, IO nanoparticles are paramagnetic and can thus be manipulated by an external magnetic field. This property means that they are magnetic only in the presence of an external field. Once the external magnetic field is removed, the nanoparticles lose

their magnetism. This enables a variety of applications such as the enrichment and purification of molecules or cells or even magnetically assisted drug delivery where an external magnetic field is placed outside the body near the site of intended particle accumulation after drug-loaded IO nanoparticles are injected systemically [21-23]. Fourth, IO nanoparticles can used as hyperthermia agents to kill tumors by heat. This can occur by the transfer of energy from an exciting time-varying magnetic field to the nanoparticle[24, 25].

Besides these applications of magnetic separation, drug delivery, and hyperthermia treatments, a major use of IO nanoparticles is as a magnetic resonance imaging (MRI) contrast agent. MRI relies on the counterbalance between the exceedingly small magnetic moment on a proton and the exceedingly large number of protons present in biological tissue, which leads to a measurable effect in the presence of large magnetic fields [19, 26, 27]. This signal can be captured by applying a time-varying magnetic field in a plane perpendicular to the first field, causing a coherent response from the net magnetic moment of the protons. Once this second oscillating field is turned off, the relaxation of the coherent response is measured. Due to their superparamagnetism, Iron oxide nanoparticles can be used to enhance MRI contrast by reducing this relaxation time, improving diagnostic sensitivity and specificity [28, 29]. For cancer imaging, they have been used to assist the identification of malignant lymph nodes, liver tumors, and brain tumors [19, 30-32].

2.3 DNA and RNA Detection

DNA and RNA are both important molecules used for detection and diagnosis of diseases such as cancer. Cancer is a genetic disease and is characterized by

aberrations that can give rise to genetic mutations, microsatellite alterations, chromosomal inversion, deletion, or recombination and promoter hypermethylation [33]. These can give rise at the RNA level to mutated genetic transcripts or altered expression of normal genes [34]. Both DNA and RNA, therefore, present themselves as promising targets for cancer detection, diagnosis/prognosis, therapy, and surveillance of therapeutic response.

It is known that when cancer is discovered early, patients live longer, require less extensive treatment, and, in general, fare much better than patients with more advanced cancer [35, 36]. Moreover, it has been found that nucleic acids in the plasma, serum, and other biological fluids of cancer patients contain a fraction that is of tumor origin [33, 37]. These so-called circulating nucleic acids (CNAs) present a promising opportunity to detect cancer through an in vitro blood assay. Such a test could have profound benefits not only for early detection of cancer but also, after detection, for disease prognosis and monitoring of therapeutic efficacy as CNAs have been found to have value for these applications as well [38-41]. Figure 2.2 illustrates how methods to detect DNA can be utilized throughout disease progression to assess risk of disease development by inherited genetic predispositions, to detect disease at its earliest stages, to diagnose disease, to predict disease course and outcome, and to monitor response of disease to treatment.

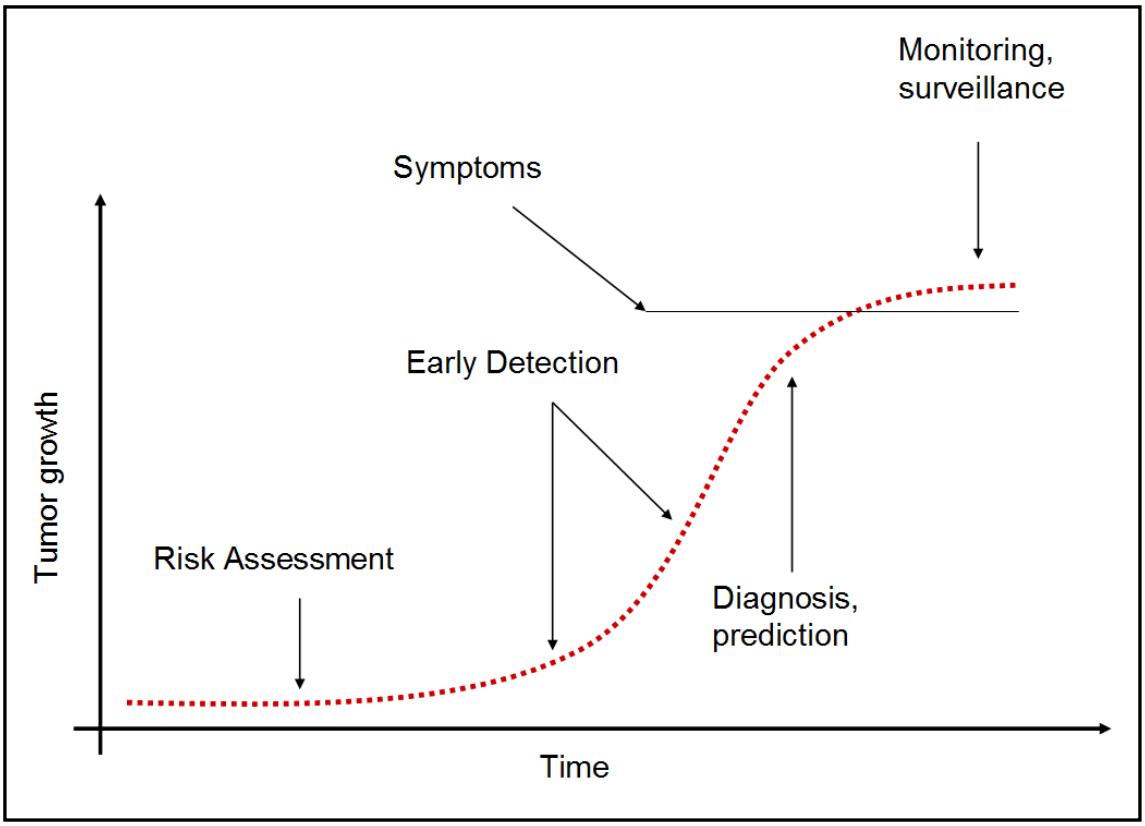

Figure 2.2: Appropriate biomarkers may be able to define risks and identify the early stages of tumor development, assist in tumor detection and diagnosis, verify stratification of patients for treatment, predict outcomes of the disease, and help in surveillance for disease recurrence [35].

2.4 Oligonucleotide Therapies

Oligonucleotide therapies such as antisense, siRNA, and microRNA have gained enormous attention in the past two decades as potential means to treat a wide host of intractable diseases. As many diseases such as genetic disorders, degenerative diseases, infections, and malignancies have a genetic basis, the promise of these molecules lies in their ability to modulate disease genetics, though at the RNA level. Discovered in the late 1970s, antisense molecules are generally single-stranded DNA fragments of 8-50 nucleotides in length that bind to messenger RNA through Watson-Crick base pairing [42]. The two molecules form a DNA-RNA

heteroduplex which is recognized by RNase H, which then cleaves the RNA strand and releases the intact DNA strand. While mRNA degradation is the major mode of action, some antisense oligonucleotides have been shown to effect translational arrest or alternative splicing [43]. The early discovery of antisense has led to its being the best understood class of therapeutic oligonucleotide, accounting for the majority of drugs in development.

Discovered in the late 1990s, siRNA are chemically synthesized double-stranded RNA sequences of 19-23 base pairs with a two nucleotide overhang on the 5'-phosphorylated end and an unphosphorylated 3'-end [44-46]. They knock down gene expression through the RNA interference mechanism. Briefly, the double-stranded siRNA is loaded into a protein-RNA complex known as the RNA induced silencing complex (RISC). RISC separates the two strands of the siRNA, discards the sense strand, and directs the antisense strand to bind to a target mRNA. Knockdown is achieved by mRNA cleavage by the enzyme Argonaute 2 [47, 48].

MicroRNA are similar to siRNA in that they are also double-stranded sequences of RNA about 20-22 base pairs in length that regulate gene expression through the RNAi pathway [49]. Like siRNA, miRNA are loaded onto the RISC complex, brought to a complementary mRNA, and signal that mRNA's cleavage or translational arrest. miRNA, however, are also distinct in a number of ways. First, miRNA are endogenous agents in cellular regulation whereas siRNA are chemically synthesized. The former are transcribed as parts of longer transcripts known as primary miRNA (pri-miRNA), processed into shorter segments (pre-miRNA) by the enzyme Drosha, then processed again by Dicer to remove a stem-loop to become the mature miRNA (Figure 2.3) [50]. Second, evidence exists that some miRNA are

responsible for regulating several mRNA transcripts whereas most siRNA are designed to knock down only one gene [51].

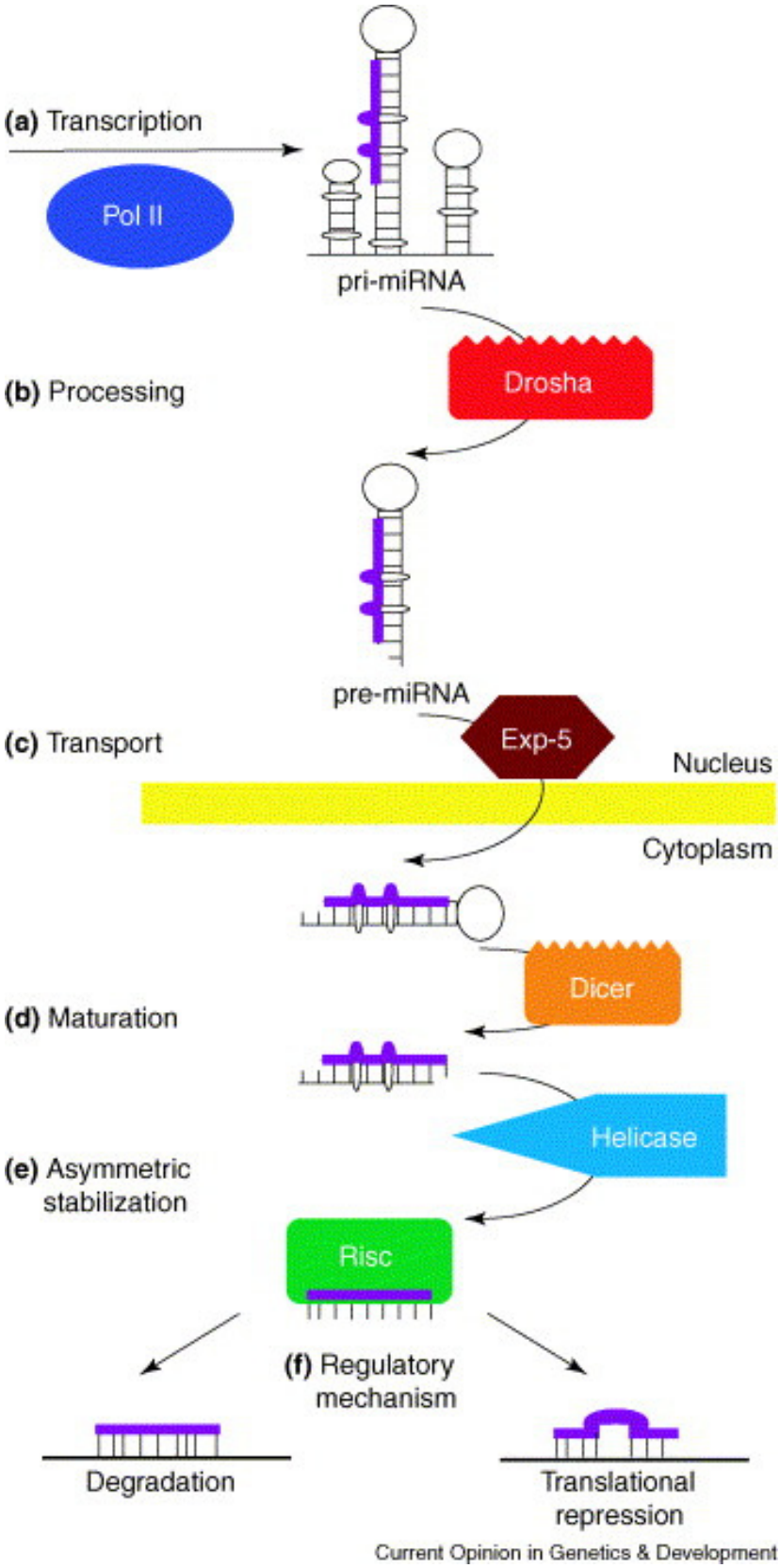

Figure 2.3: Developmental pathway of miRNA [50].

The therapeutic potential of miRNAs exists in the fact that they have been found to be fundamental gene regulators controlling proliferation, differentiation, and apoptosis during development and have been implicated in a large host of diseases including cancer [49, 52-56]. As cancer gene regulators, miRNAs function as both oncogenes and tumor supressors. Antisense molecules may thus be delivered to inhibit overexpressed miRNA (e.g. oncogenes) and miRNA mimics may be delivered to increase miRNA that are weakly expressed (e.g. tumor suppressors). For the sake of clarity, antisense molecules directed towards miRNA will hereafter be referred to as antagomirs [57].

2.5 Oligonucleotide Delivery

While oligonucleotides hold great therapeutic promise, a major issue is delivery as they are prone to degradation by serum nucleases, may stimulate innate immune response, and—owing to the negative charge of their phosphate backbone and hydrophilicity—are unable to traverse the anionic cell membrane [4, 58-64]. Viral vectors, benefitting from evolutionary optimization, have a high transfection efficiency; however, fundamental problems related to toxicity, immunogenicity, and scale-up procedures have encouraged the investigation of alternative nonviral approaches such as cationic lipids, dendrimers, polymers, and other nanoparticles [65]. These nonviral vectors exhibit relatively inferior, though still significant, efficiency and have improved toxicity profiles. Cationic polymers, in particular, are a promising nonviral approach due to their ability to be extensively modified and to other advantageous features for pharmaceutical products including reproducibility of preparation and stability for long-term storage [66].

In order to efficiently deliver oligonucleotides, polymer vectors must achieve a number of important steps (Figure 2.4). First, they must bind to, or complex with, the oligonucleotide. For the case of cationic polymers, this typically occurs through electrostatic interaction. Second, the polymer-oligonucleotide complex must enter the cell. This can occur through either targeted or nontargeted means. For targeted entry, the polymer is conjugated to a ligand or other targeting agent that will bind to cell-surface receptors to effect receptor-mediated endocytosis. For nontargeted entry, cellular internalization still occurs through endocytosis although the exact mechanism is still not understood [67, 68]. Generally, untargeted polymer complexes still maintain a slight positive charge even upon binding of the DNA/RNA, causing it to associate with the anionic cell membrane, which should assist in internalization. Finally, the oligonucleotide must be able to escape from the endosome. Endosomal escape can occur in several ways including incorporation of the lysosomotropic agent chloroquine or membrane-destabilizing peptides such as the N-terminal peptides of Rhinovirus VP-1 [69, 70]. Alternatively, incorporation of amine groups may exploit the so-called “proton sponge effect” [71]. Briefly, initial internalization is followed by sequential intracellular trafficking into a variety of low pH endomembrane compartments, including endosomes and lysosomes [72]. As the endosomal pH lowers (pH 5.0-6.2) amines with low pK_a values start to be protonated and thus buffer the acidic environment [73, 74]. To counter this buffering capacity, cells pump H^+ to acidify the endosomal compartment. This, however, is accompanied by endosomal Cl^- accumulation, which causes osmotic swelling and/or lysis of the endosome [75].

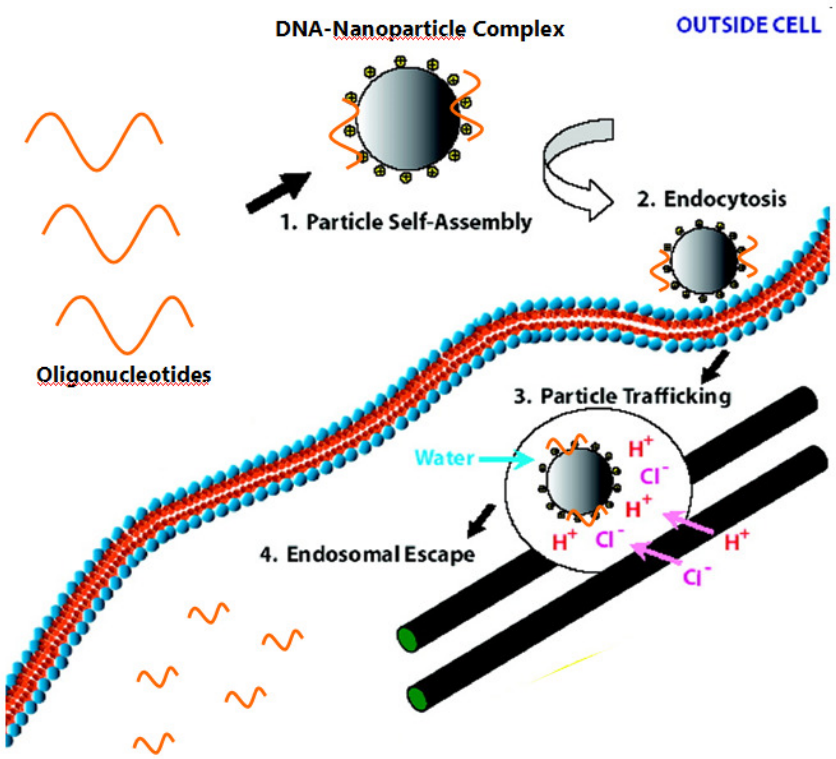

Figure 2.4: Mechanism of nanoparticle delivery of oligonucleotides. Adapted from Anderson et al [76].

As a next step from pure cationic polymer vectors, several groups have developed cationic polymer-coated inorganic nanoparticles as multifunctional delivery vehicles. There are several advantages to this approach. First, because inorganic nanoparticles are typically rigid with a well-defined structure, they afford the ability to engineer delivery vehicles with carefully controlled sizes and shapes to optimize biological interaction [77-80]. Second, they can serve as a scaffold upon which multiple functionalities, such as drugs, targeting agents, cationic amines, and pH buffering groups can be attached. Third, the inorganic nanoparticles themselves may exhibit unique properties that may be exploited to improve therapeutic performance. For instance, semiconductor nanoparticles (i.e. quantum dots) exhibit fluorescent properties that may be used for simultaneous drug delivery and optical

imaging for monitoring of delivery [81, 82]. Mesoporous silica nanoparticles can be used for simultaneous small-molecule drug and nucleic acid delivery by interiorly loading the particles with nanovalves and drugs for on-demand drug release while loading the surface of the particles with cationic polymer and nucleic acids [83]. Iron oxide nanoparticles exhibit superparamagnetic, hyperthermia and magnetic resonance properties that confer use for magnetically-assisted drug delivery, thermal ablation therapy, and magnetic resonance imaging [84]. Gold nanoparticles exhibit optical and photothermal properties that can be used for monitoring of delivery as well as for photothermal therapy [85].

2.6 References

1. Smith, A.M. and S.M. Nie, *Chemical analysis and cellular imaging with quantum dots.* Analyst, 2004. **129**(8): p. 672-677.

2. Obonyo, O., et al., *Quantum dots synthesis and biological applications as imaging and drug delivery systems.* Critical Reviews in Biotechnology, 2010. **30**(4): p. 283-301.

3. Sun, C., J.S.H. Lee, and M.Q. Zhang, *Magnetic nanoparticles in MR imaging and drug delivery.* Advanced Drug Delivery Reviews, 2008. **60**(11): p. 1252-1265.

4. Marques, J.T. and B.R.G. Williams, *Activation of the mammalian immune system by siRNAs.* Nature Biotechnology, 2005. **23**(11): p. 1399-1405.

5. Dabbousi, B.O., et al., *(CdSe)ZnS core-shell quantum dots: Synthesis and characterization of a size series of highly luminescent nanocrystallites.* Journal of Physical Chemistry B, 1997. **101**(46): p. 9463-9475.

6. Hines, M.A. and P. Guyot-Sionnest, *Synthesis and characterization of strongly luminescing ZnS-Capped CdSe nanocrystals.* Journal of Physical Chemistry, 1996. **100**(2): p. 468-471.

7. Peng, X.G., et al., *Epitaxial growth of highly luminescent CdSe/CdS core/shell nanocrystals with photostability and electronic accessibility.* Journal of the American Chemical Society, 1997. **119**(30): p. 7019-7029.

8. Smith, A.M., et al., *Bioconjugated quantum dots for in vivo molecular and cellular imaging.* Advanced Drug Delivery Reviews, 2008. **60**(11): p. 1226-1240.

9. Xing, Y., et al., *Bioconjugated quantum dots for multiplexed and quantitative immunohistochemistry.* Nature Protocols, 2007. **2**(5): p. 1152-1165.

10. Wu, X.Y., et al., *Immunofluorescent labeling of cancer marker Her2 and other cellular targets with semiconductor quantum dots.* Nature Biotechnology, 2003. **21**(1): p. 41-46.

11. Fountaine, T.J., et al., *Multispectral imaging of clinically relevant cellular targets in tonsil and lymphoid tissue using semiconductor quantum dots.* Modern Pathology, 2006. **19**(9): p. 1181-1191.

12. Giepmans, B.N.G., et al., *Correlated light and electron microscopic imaging of multiple endogenous proteins using Quantum dots.* Nature Methods, 2005. **2**(10): p. 743-749.

13. Gao, X.H., et al., *In vivo cancer targeting and imaging with semiconductor quantum dots.* Nature Biotechnology, 2004. **22**(8): p. 969-976.

14. Han, M.Y., et al., *Quantum-dot-tagged microbeads for multiplexed optical coding of biomolecules.* Nature Biotechnology, 2001. **19**(7): p. 631-635.

15. Liang, R.Q., et al., *An oligonucleotide microarray for microRNA expression analysis based on labeling RNA with quantum dot and nanogold probe.* Nucleic Acids Research, 2005. **33**(2).

16. Dahan, M., et al., *Diffusion dynamics of glycine receptors revealed by single-quantum dot tracking.* Science, 2003. **302**(5644): p. 442-445.

17. Smith, A.M., et al., *Multicolor quantum dots for molecular diagnostics of cancer.* Expert Review of Molecular Diagnostics, 2006. **6**(2): p. 231-244.

18. Smith, A.M., X.H. Gao, and S.M. Nie, *Quantum dot nanocrystals for in vivo molecular and cellular imaging.* Photochemistry and Photobiology, 2004. **80**(3): p. 377-385.

19. Pankhurst, Q.A., et al., *Applications of magnetic nanoparticles in biomedicine.* Journal of Physics D-Applied Physics, 2003. **36**(13): p. R167-R181.

20. Guardia, P., et al., *Controlled Synthesis of Iron Oxide Nanoparticles over a Wide Size Range.* Langmuir, 2010. **26**(8): p. 5843-5847.

21. Scarberry, K.E., et al., *Magnetic nanoparticle-peptide conjugates for in vitro and in vivo targeting and extraction of cancer cells.* Journal of the American Chemical Society, 2008. **130**(31): p. 10258-10262.

22. Plank, C., et al., *The magnetofection method: Using magnetic force to enhance gene delivery.* Biological Chemistry, 2003. **384**(5): p. 737-747.

23. Gupta, A.K. and M. Gupta, *Cytotoxicity suppression and cellular uptake enhancement of surface modified magnetic nanoparticles.* Biomaterials, 2005. **26**(13): p. 1565-1573.

24. Sonvico, F., et al., *Folate-conjugated iron oxide nanoparticles for solid tumor targeting as potential specific magnetic hyperthermia mediators: Synthesis, physicochemical characterization, and in vitro experiments.* Bioconjugate Chemistry, 2005. **16**(5): p. 1181-1188.

25. Fortin, J.P., et al., *Size-sorted anionic iron oxide nanomagnets as colloidal mediators for magnetic hyperthermia.* Journal of the American Chemical Society, 2007. **129**(9): p. 2628-2635.

26. Livingston, J., *Driving Force: The Natural Magic of Magnets*. 1996, Cambridge: Harvard University Press.

27. Elster, A.a.B., J, *Questions and Answers in Magnetic Resonance Imaging*. 2001, St. Louis, USA: Mosby.

28. Neuberger, T., et al., *Superparamagnetic nanoparticles for biomedical applications: Possibilities and limitations of a new drug delivery system.* Journal of Magnetism and Magnetic Materials, 2005. **293**(1): p. 483-496.

29. Mornet, S., et al., *Magnetic nanoparticle design for medical diagnosis and therapy.* Journal of Materials Chemistry, 2004. **14**(14): p. 2161-2175.

30. Michel, S.C.A., et al., *Preoperative breast cancer staging: MR imaging of the axilla with ultrasmall superparamagnetic iron oxide enhancement.* Radiology, 2002. **225**(2): p. 527-536.

31. Semelka, R.C. and T.K.G. Helmberger, *Contrast agents for MR imaging of the liver.* Radiology, 2001. **218**(1): p. 27-38.

32. Enochs, W.S., et al., *Improved delineation of human brain tumors on MR images using a long-circulating, superparamagnetic iron oxide agent.* Jmri-Journal of Magnetic Resonance Imaging, 1999. **9**(2): p. 228-232.

33. Fleischhacker, M. and B. Schmidt, *Circulating nucleic acids (CNAs) and cancer - A survey.* Biochimica Et Biophysica Acta-Reviews on Cancer, 2007. **1775**(1): p. 181-232.

34. Knudson, A.G., *GENETICS OF HUMAN CANCER.* Annual Review of Genetics, 1986. **20**: p. 231-251.

35. Levenson, V.V., *Biomarkers for early detection of breast cancer: What, when, and where?* Biochimica Et Biophysica Acta-General Subjects, 2007. **1770**(6): p. 847-856.

36. Etzioni, R., et al., *The case for early detection.* Nature Reviews Cancer, 2003. **3**(4): p. 243-252.

37. Dong, S.M., et al., *Detecting colorectal cancer in stool with the use of multiple genetic targets.* Journal of the National Cancer Institute, 2001. **93**(11): p. 858-865.

38. Chan, K.C.A. and Y.M.D. Lo, *Circulating tumour-derived nucleic acids in cancer patients: potential applications as tumour markers.* British Journal of Cancer, 2007. **96**(5): p. 681-685.

39. Swarup, V. and M.R. Rajeswari, *Circulating (cell-free) nucleic acids - A promising, non-invasive tool for early detection of several human diseases.* Febs Letters, 2007. **581**(5): p. 795-799.

40. Mehra, N., et al., *Circulating mitochondrial nucleic acids have prognostic value for survival in patients with advanced prostate cancer.* Clinical Cancer Research, 2007. **13**(2): p. 421-426.

41. Fiegl, H., et al., *Circulating tumor-specific DNA: A marker for monitoring efficacy of adjuvant therapy in cancer patients.* Cancer Research, 2005. **65**(4): p. 1141-1145.

42. Bennett, C.F. and E.E. Swayze, *RNA Targeting Therapeutics: Molecular Mechanisms of Antisense Oligonucleotides as a Therapeutic Platform.* Annual Review of Pharmacology and Toxicology, 2010. **50**: p. 259-293.

43. Sazani, P. and R. Kole, *Therapeutic potential of antisense oligonucleotides as modulators of alternative splicing.* Journal of Clinical Investigation, 2003. **112**(4): p. 481-486.

44. Elbashir, S.M., et al., *Duplexes of 21-nucleotide RNAs mediate RNA interference in cultured mammalian cells.* Nature, 2001. **411**(6836): p. 494-498.

45. Amarzguioui, M., J.J. Rossi, and D. Kim, *Approaches for chemically synthesized siRNA and vector-mediated RNAi.* Febs Letters, 2005. **579**(26): p. 5974-5981.

46. Fire, A., et al., *Potent and specific genetic interference by double-stranded RNA in Caenorhabditis elegans.* Nature, 1998. **391**(6669): p. 806-811.

47. Liu, J.D., et al., *Argonaute2 is the catalytic engine of mammalian RNAi.* Science, 2004. **305**(5689): p. 1437-1441.

48. Meister, G., et al., *Human Argonaute2 mediates RNA cleavage targeted by miRNAs and siRNAs.* Molecular Cell, 2004. **15**(2): p. 185-197.

49. Calin, G.A. and C.M. Croce, *MicroRNA signatures in human cancers.* Nature Reviews Cancer, 2006. **6**(11): p. 857-866.

50. Pasquinelli, A.E., S. Hunter, and J. Bracht, *MicroRNAs: a developing story.* Current Opinion in Genetics & Development, 2005. **15**(2): p. 200-205.

51. Lim, L.P., et al., *Microarray analysis shows that some microRNAs downregulate large numbers of target mRNAs.* Nature, 2005. **433**(7027): p. 769-773.

52. Kloosterman, W.P. and R.H.A. Plasterk, *The diverse functions of MicroRNAs in animal development and disease.* Developmental Cell, 2006. **11**(4): p. 441-450.

53. Esquela-Kerscher, A. and F.J. Slack, *Oncomirs - microRNAs with a role in cancer.* Nature Reviews Cancer, 2006. **6**(4): p. 259-269.

54. Garzon, R., et al., *MicroRNA expression and function in cancer.* Trends in Molecular Medicine, 2006. **12**(12): p. 580-587.

55. Croce, C.M. and G.A. Calin, *miRNAs, cancer, and stem cell division.* Cell, 2005. **122**(1): p. 6-7.

56. Hammond, S.M., *MicroRNAs as oncogenes.* Current Opinion in Genetics & Development, 2006. **16**(1): p. 4-9.

57. Krutzfeldt, J., et al., *Silencing of microRNAs in vivo with 'antagomirs'.* Nature, 2005. **438**(7068): p. 685-689.

58. Mislick, K.A. and J.D. Baldeschwieler, *Evidence for the role of proteoglycans in cation-mediated gene transfer.* Proceedings of the National Academy of Sciences of the United States of America, 1996. **93**(22): p. 12349-12354.

59. Mounkes, L.C., et al., *Proteoglycans mediate cationic Liposome-DNA complex-based gene delivery in vitro and in vivo.* Journal of Biological Chemistry, 1998. **273**(40): p. 26164-26170.

60. de Fougerolles, A., et al., *Interfering with disease: a progress report on siRNA-based therapeutics.* Nature Reviews Drug Discovery, 2007. **6**(6): p. 443-453.

61. Bumcrot, D., et al., *RNAi therapeutics: a potential new class of pharmaceutical drugs.* Nature Chemical Biology, 2006. **2**(12): p. 711-719.

62. Kleinman, M.E., et al., *Sequence- and target-independent angiogenesis suppression by siRNA via TLR3.* Nature, 2008. **452**(7187): p. 591-U1.

63. Judge, A.D., et al., *Sequence-dependent stimulation of the mammalian innate immune response by synthetic siRNA.* Nature Biotechnology, 2005. **23**(4): p. 457-462.

64. Hornung, V., et al., *Sequence-specific potent induction of IFN-alpha by short interfering RNA in plasmacytoid dendritic cells through TLR7.* Nature Medicine, 2005. **11**(3): p. 263-270.

65. Verma, I.M. and N. Somia, *Gene therapy - promises, problems and prospects.* Nature, 1997. **389**(6648): p. 239-242.

66. Christie, R.J., N. Nishiyama, and K. Kataoka, *Minireview: Delivering the Code: Polyplex Carriers for Deoxyribonucleic Acid and Ribonucleic Acid Interference Therapies.* Endocrinology, 2010. **151**(2): p. 466-473.

67. Opalinska, J.B. and A.M. Gewirtz, *Nucleic-acid therapeutics: Basic principles and recent applications.* Nature Reviews Drug Discovery, 2002. **1**(7): p. 503-514.

68. Mintzer, M.A. and E.E. Simanek, *Nonviral Vectors for Gene Delivery.* Chemical Reviews, 2009. **109**(2): p. 259-302.

69. Deduve, C., et al., *LYSOSOMOTROPIC AGENTS.* Biochemical Pharmacology, 1974. **23**(18): p. 2495-&.

70. Wagner, E., *Application of membrane-active peptides for nonviral gene delivery.* Advanced Drug Delivery Reviews, 1999. **38**(3): p. 279-289.

71. Behr, J.P., *The proton sponge: A trick to enter cells the viruses did not exploit.* Chimia, 1997. **51**(1-2): p. 34-36.

72. Juliano, R., et al., *Biological Barriers to Therapy with Antisense and siRNA Oligonucleotides.* Molecular Pharmaceutics, 2009. **6**(3): p. 686-695.

73. Ohkuma, S. and B. Poole, *FLUORESCENCE PROBE MEASUREMENT OF INTRALYSOSOMAL PH IN LIVING CELLS AND PERTURBATION OF PH BY VARIOUS AGENTS.* Proceedings of the National Academy of Sciences of the United States of America, 1978. **75**(7): p. 3327-3331.

74. Kulkarni, R.P., et al., *Single cell kinetics of intracellular, nonviral, nucleic acid delivery vehicle acidification and trafficking.* Bioconjugate Chemistry, 2005. **16**(4): p. 986-994.

75. Sonawane, N.D., F.C. Szoka, and A.S. Verkman, *Chloride accumulation and swelling in endosomes enhances DNA transfer by polyamine-DNA polyplexes.* Journal of Biological Chemistry, 2003. **278**(45): p. 44826-44831.

76. Green, J.J., R. Langer, and D.G. Anderson, *A combinatorial polymer library approach yields insight into nonviral gene delivery.* Accounts of Chemical Research, 2008. **41**(6): p. 749-759.

77. Jiang, W., et al., *Nanoparticle-mediated cellular response is size-dependent.* Nature Nanotechnology, 2008. **3**(3): p. 145-150.

78. Chithrani, B.D. and W.C.W. Chan, *Elucidating the mechanism of cellular uptake and removal of protein-coated gold nanoparticles of different sizes and shapes.* Nano Letters, 2007. **7**(6): p. 1542-1550.

79. Chithrani, B.D., A.A. Ghazani, and W.C.W. Chan, *Determining the size and shape dependence of gold nanoparticle uptake into mammalian cells.* Nano Letters, 2006. **6**(4): p. 662-668.

80. Cho, E.C., et al., *The Effects of Size, Shape, and Surface Functional Group of Gold Nanostructures on Their Adsorption and Internalization by Cells.* Small, 2010. **6**(4): p. 517-522.

81. Yezhelyev, M.V., et al., *Proton-sponge coated quantum dots for siRNA delivery and intracellular imaging.* Journal of the American Chemical Society, 2008. **130**(28): p. 9006-9012.

82. Wang, S.H., et al., *Positively charged and pH self-buffering quantum dots for efficient cellular uptake by charge mediation and monitoring cell membrane permeability.* Nanotechnology, 2009. **20**(42).

83. Xia, T.A., et al., *Polyethyleneimine Coating Enhances the Cellular Uptake of Mesoporous Silica Nanoparticles and Allows Safe Delivery of siRNA and DNA Constructs.* Acs Nano, 2009. **3**(10): p. 3273-3286.

84. Arruebo, M., et al., *Magnetic nanoparticles for drug delivery.* Nano Today, 2007. **2**(3): p. 22-32.

85. Huang, X.H., et al., *Cancer cell imaging and photothermal therapy in the near-infrared region by using gold nanorods.* Journal of the American Chemical Society, 2006. **128**(6): p. 2115-2120.

CHAPTER 3

CANCER-ASSOCIATED DNA DETECTION BY QUANTUM DOT NANOCRYSTALS ON SINGLE MAGNETIC MICROBEADS

3.1 Introduction

Cancer is the second greatest cause of death in the United States after heart disease [1]. In the fight against this disease, an important conclusion has been made: Early detection of cancer is critical for successful intervention and survival [2]. According to data reported by the NCI Surveillance Epidemiology and End Results (SEER) Program, patients having noticeable tumors have high five-year survival rates (91.1% for skin melanoma and 88.6% for breast cancer) whereas those having tumors of internal organs have low five-year survival rates (10.8% for liver & intrahepatic bile duct and 5% for pancreas). Such a high disparity in outcomes between cancer in observable sites and in internal organs indicates how frequently tumor detection depends on either direct inspection (e.g. skin melanoma) or enhanced imaging (e.g. mammography for breast cancer) and highlights the need for improved methods to detect cancer at its earliest stages [3].

The discovery of tumor-related DNA in blood and other biological fluids presents a potential assay to noninvasively detect cancer at early stages [4, 5]. Leon et al demonstrated that cancer patients had much higher circulating DNA concentrations than those suffering from non-malignant diseases. Moreover, in some cases, the levels of circulating DNA would decrease after successful anticancer therapy [6, 7]. Since this discovery, further studies have been performed demonstrating that cancer-related genetic mutations (such as N-ras in

myelodysplastic syndrome and K-ras in pancreatic and colorectal cancer) [8-10], DNA rearrangements [4], and microsatellite alterations [11, 12], could all be detected in the serum of patients.

Magnetic microbead (MMB) technology is a promising technology for detecting molecules such as circulating nucleic acids (CNA). They are usually embedded with superparamagnetic iron oxides such that they can be mixed readily with biological samples and only exhibit magnetic properties—and thus be used for sample purification/collection—in the presence of an external magnetic field. They have already been used in a number of studies for purifying and enriching specific proteins and nucleic acid sequences in solution with high specificity [13-18].

Most MMB studies involving the capture and analysis of biological targets, however, have relied upon traditional fluorescent dyes, which suffer from relatively poor photostability and photobrightness. Fluorescent nanoparticles such as quantum dots (QDs), however, have improved brightness and photostability that enable their use in ultrasensitive detection formats [19-22]. Indeed, QDs are so bright that individual particles can be observed through a fluorescent microscope [23].

We present here a bead-based sandwich assay wherein free cancer-related DNA in solution is collected and enriched by MMBs. QDs are then used as a reporter dye to detect captured DNA on the MMBs. Standard fluorescence microscopy, spectroscopy, and image analysis are used to analyze and quantify single beads and determine target concentration based on total fluorescence intensity. The advantage of this method is that it combines the ability of MMBs to enrich low concentration targets with the superior optical properties of QDs to enable sensitive DNA detection at sub-picomolar concentrations.

3.2 Methods

Materials

Streptavidin-coated 655 nm emitting quantum dots were purchased from Invitrogen (Foster City, CA). Streptavidin-coated magnetic microbeads (~1um in diameter) were purchased from Bangs Labs. DNA probes were purchased from IDT (Coralville, IA) and sequences were as follows: Probe 1 5'-GTTCAGTTTCTCGGGAAAAAAAAAAA-biotin triethylene glycol -3'; Probe 2 5' -biotin triethylene glycol-AAAAAAAAAACTCCTCCAGCTCCT – 3'; BCAR3 Target Probe: 5'- CCCGAGAAACTGAAGAAGGAGCTGGAGGA - 3'

QD and Magnetic Bead Conjugation

To determine the optimal amount of DNA probe that should be conjugated to the quantum dots, 2 ul of 1 uM streptavidin QDs with emission maxima of 655 nm were incubated with varying amounts of Probe 1 for 2 hours at room temperature. As the manufacturer estimates ~16 available biotin-binding sites per QD, an excess (10 ul of 200 ng/ml) of free biotin was then added to each reaction mixture to saturate any unoccupied biotin-binding sites on the QDs. Electrophoresis was then performed to verify successful conjugation of probe to QD using a 0.8% agarose/0.1% Tween-20 in 1X TBE buffer. Gels were fun for 20 minutes at 105 V. In subsequent experiments 1:1.5 molar ratio of QD:Probe 1 was used.

MMBs were conjugated to Probe 2 by incubating 510,000 beads with a 20-fold excess of biotinylated Probe 2 to biotin-binding site per MMB in 0.1M borate buffer (pH 8) in a 1.5 ml Eppendorf Tube. The mixture was incubated for 2 hours with rotation on a Labquake rotator (Barnstead/Thermolyne). Beads were then pulled out of solution by placing on a 1.5 Tesla NdFeB permanent magnet (MCE Products,

Torrance, CA) and washed 3 times in 0.1 M borate buffer. An excess of free streptavidin was the added to prevent any unbound Probe 2 from being captured by QDs in subsequent steps. Beads were applied to a magnet and washed an additional 3 times in 0.1 M borate buffer.

DNA Detection

For DNA detection, an appropriate amount of BCAR3 target was added to a tube containing 1 ml of hybridization buffer (2.82 ul salmon sperm DNA (Invitrogen), 2.56 ul E.Coli tRNA (Roche), 20 ul 50X Denhardt's in 1XSSC/0.2%BSA/0.1%NaN_3). This was allowed to prehybridize for 2 hours at room temperature. All of the Probe 1-conjugated QDs and 100,000 beads of the Probe 2-conjugated MMBs were then added to the reaction mixture and allowed to hybridize overnight on a Labquake rotator (Barnstead/Thermolyne). Particles were then washed once for 10 min in 1XSSC/0.2%BSA/0.1%NaN_3, twice for 30 min in 0.5XSSC/0.2%BSA/0.1%NaN_3, and finally 3 times briefly in 0.1M borate buffer.

Data Acquisition and Analysis

The bead suspension was volume reduced to 10-20 ul by magnetic separation and placed between two glass coverslips (no. 1 coverglass, Corning Inc., Corning, NY) for imaging on an Olympus IX-71 microscope (Center Valley, PA) that was equipped with a mercury lamp for excitation, a Nikon D70 color digital camera, and a 100X objective (NA 1.25, oil). True color fluorescence images were obtained by using 488-nm exicitation and a long pass filter (505nm, Chroma Technology Corp., Brattleboro, VT). The fluorescence spectra of pure QDs were recorded by using a standard fluorometer (FluoMax; Jobin Yvon, Edison, NJ). Fluorescence spectra of single beads containing QDs were recorded by using a spectrophotometer

(SpectraPro 150, Roper Scientific, Trenton, NJ) attached to the side port of the microscope. All images were analyzed by using NIH Image J software [24].

3.3 Results and Discussion

The procedure for the DNA detection assay is shown in Figure 3.1. In this procedure, 655nm emission quantum dots and magnetic microbeads are conjugated to oligononucleotide Probes 1 and 2, respectively, that are designed to sandwich a biologically relevant target sequence, a 29-mer portion of BCAR3. BCAR3 (Breast Cancer Antiestrogen Resistance-3), is a member of the novel Src homology 2 (SH2)-containing protein family that may promote an epithelial-mesenchymal transition in breast cancer cells [25-27]. It was first identified in a screen for genes whose overexpression conferred resistance to antiestrogens and may thus aid in therapeutic strategy decisions for breast cancer patients [28, 29]. Hybridization of this target sequence with the two oligonucleotide probes causes the QDs to surround the MMBs. After magnetic separation and enrichment, these complexes can then be imaged using a fluorescence microscope and the QD fluorescence emission on each MMB quantified. The fluorescence measurements are averaged over several beads and the amount of target oligonucleotide in solution can be inferred by the level of QD fluorescence per microbead.

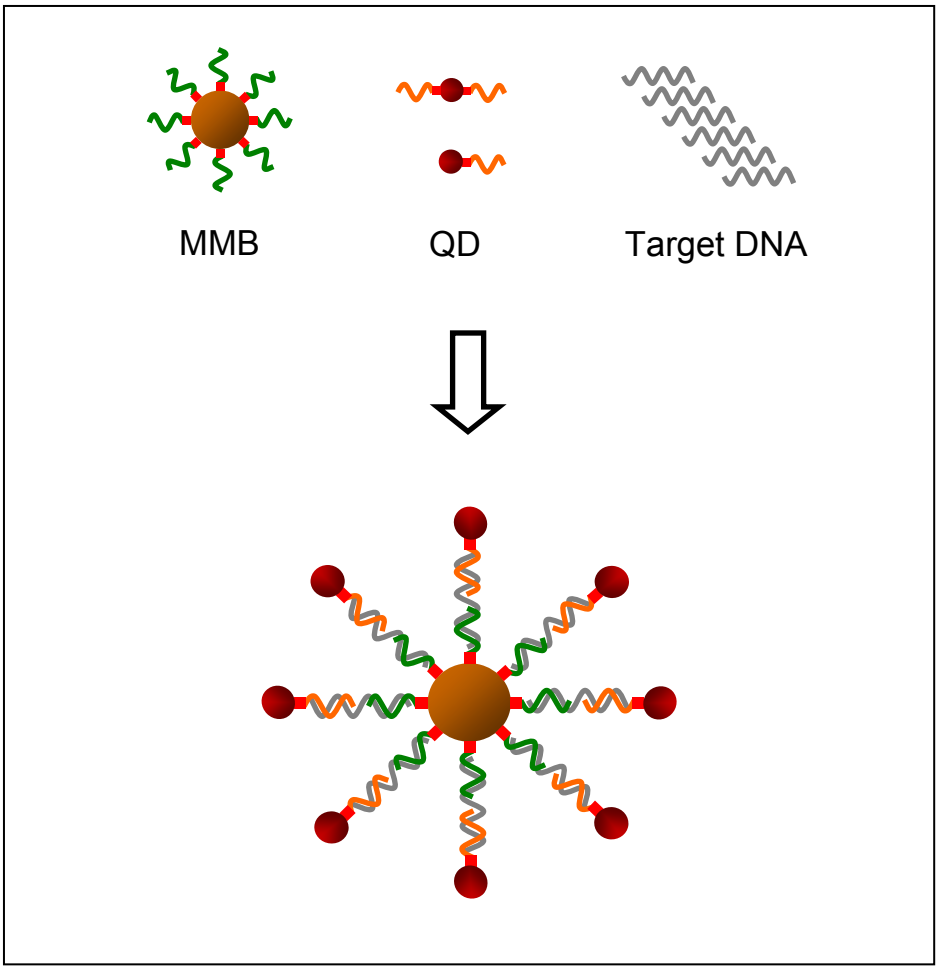

Figure 3.1: Schematic illustration of sandwich assay using magnetic microbeads and quantum dots to detect BCAR3 DNA fragment.

Probe Conjugation

QD-Probe 1 conjugation must be controlled to ensure proper binding of the particles. Having too many probes conjugated per QD can give rise to several undesired effects. First, it can cause aggregation of QD/beads with QDs crosslinking multiple microbeads, making difficult the ability to accurately measure fluorescence from single beads. Second, there is the potential for multiple target DNA to bind to a single QD. This could lead to some target DNA not being detected either because steric issues would prevent them from binding to an MMB or because multiple target DNA bridge the same QD-MMB pair. Ideally, each QD would have one Probe 1

attached such that each QD docked onto an MMB would represent a single target molecule in solution.

To control the amount of Probe 1 conjugated per QD particle, a gel migration assay was performed. Streptavidin-conjugated QDs were incubated with biotin-labeled Probe 1 in 5:1, 2:1, 1:1, 1:1.5, 1:2, 1:5, and 1:10 QD:Probe 1 molar ratios and the migration patterns of the conjugated complexes were evaluated by gel electrophoresis. As QDs are conjugated to Probe 1, the negative charge from the DNA should cause the particles to migrate further down the gel towards the cathode. Figure 3.2 shows that starting with a 5:1 QD:Probe 1 ratio, most of the QDs do not exhibit any enhanced migration relative to the lane containing QDs alone. There is a faint smear further down the lane, however, which corresponds to some of the particles having bound some DNA. As the amount of Probe 1 incubated per QD is increased, the band corresponding to unconjugated QD fades and the QDs migrate further and further down the gel.

Interestingly, a faint discrete band (see arrow) appears in the 5:1 lane just below the band corresponding to unconjugated QDs that increases in intensity as the amount of DNA probe is increased, reaching a maximum at a 1:1.5 QD:Probe 1 ratio. Seeing as this band appears at a 5:1 ratio, it may correspond to QDs with only one Probe 1 attached, consistent with other reports of discrete electrophoresis bands arising from discrete numbers of oligonucleotides conjugated onto nanoparticles [30, 31]. We thus decided to conjugate QDs at a 1:1.5 QD:Probe 1 molar ratio for subsequent experiments.

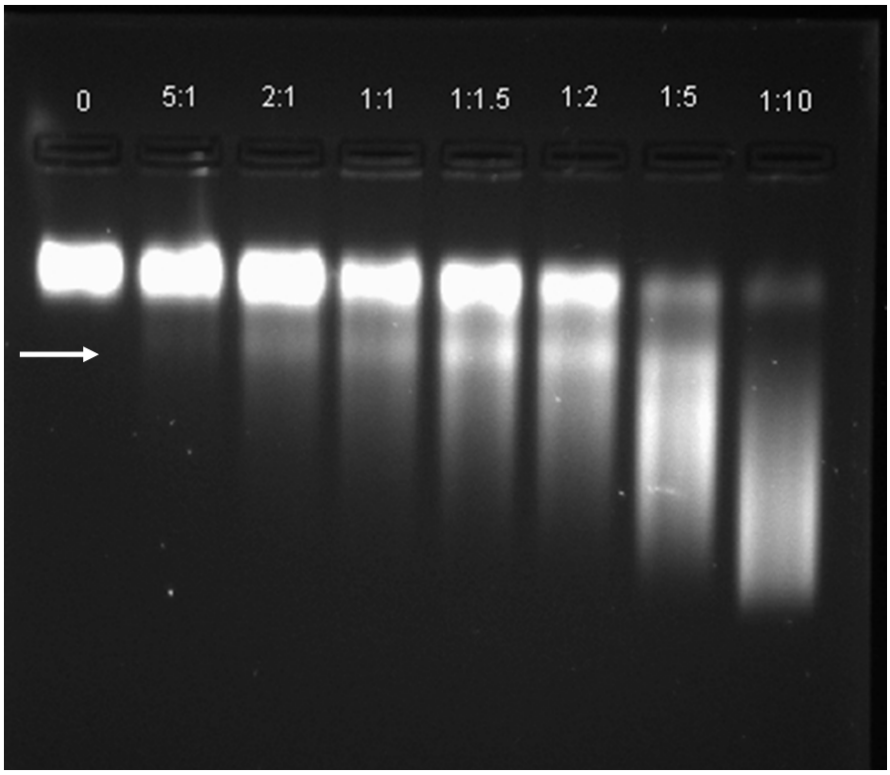

Figure 3.2: Gel mobility assay demonstrating QD-Probe1 conjugation. Streptavidin-conjugated QDs were incubated with biotin-Probe1 at various ratios. Arrow points out faint discrete band that may correspond to QDs conjugated to a single Probe1. Ratios are QD:Probe1 feed ratios. 0 = QDs alone without Probe1.

Assay Optimization

Because quantum dots and oligonucleotides can both exhibit nonspecific binding and hybridization, for target detection experiments we also wanted to evaluate several conditions to optimize signal to noise ratio. We evaluated target detection under conditions of differing temperatures as well as blocking buffers, while keeping all other variables constant. For temperature, we performed the sandwich assay at both room temperature as well as at a slightly elevated temperature of 30C, which should decrease some nonspecific hybridization of DNA (e.g. between probe 1 and probe 2 directly without target DNA bridging the two). We also performed a blocking step on the beads whereby we exposed the MMBs to a

mixture of blocking agents prior to adding the target oligonucleotide or Probe 1-conjugated QDs. For blocking buffer, we evaluated both 0.2% BSA mixtures containing or not containing Denhardt's Solution, which contains Ficoll 400 and polyvinilpyrolidone to minimize nonspecific interaction of oligonucleotides with substrates and is frequently used in *in situ* hybridization experiments. Figure 3.3 shows our results for this optimization study. There was a statistically significant improvement in the signal-to-noise ratio (SNR) when the temperature was increased to 30C versus room temperature. No statistically significant difference was observed, however, with the addition of Denhardt's Solution. Interestingly the increase in SNR at 30C was accompanied by an increase in overall signal. This indicates that the slight increase in temperature decreased nonspecific binding of oligonucleotide pairs that inhibit tethering of the QDs to the MMBs, such as homodimers.

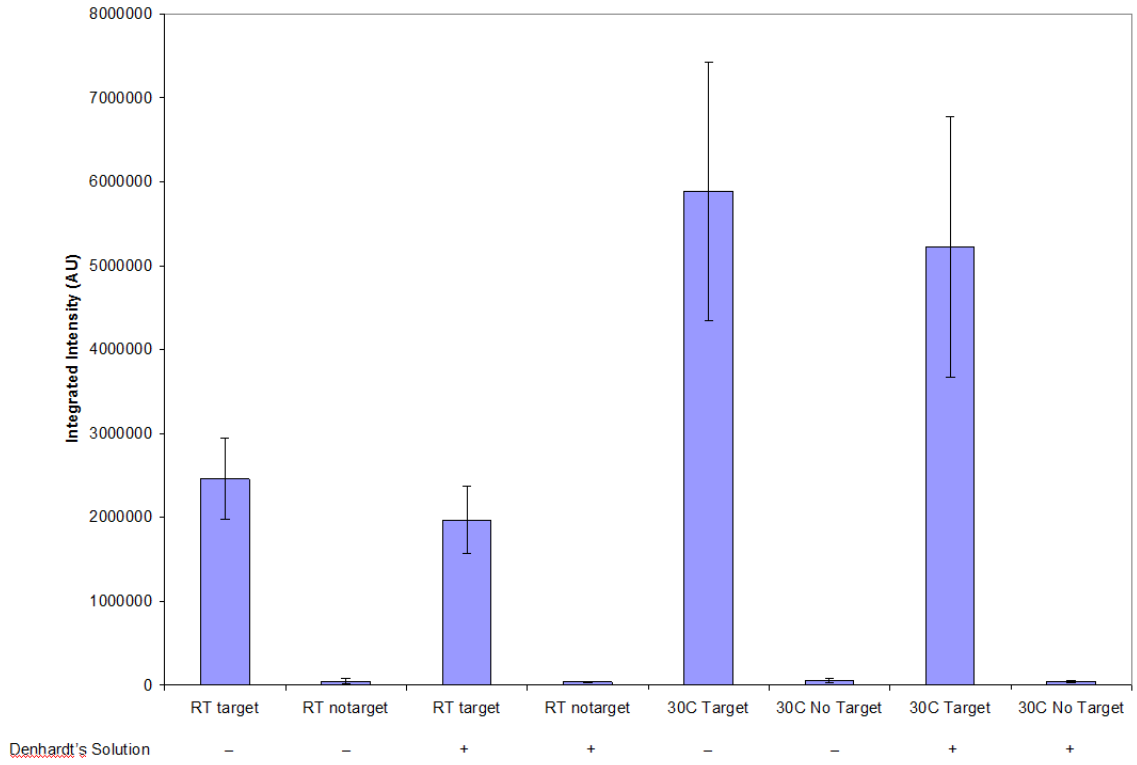

	RT		30C	
Denhardt's Solution	-	+	-	+
SNR	53.6 ± 10.4	49.7 ± 10.1	103.9 ± 27.1	121.2 ± 36.0

Figure 3.3: Signal-to-noise under varying temperature and incubation buffer conditions. SNR was improved by performing sandwich assay at 30C versus RT. Addition or absence of Denhardt's Solution did not result in a statistically significant difference.

DNA Detection

Having optimized the SNR for the bead assay, we performed the experiment on a range of target DNA concentrations (20 fM to 2 pM) to investigate the sensitivity of the assay. Figure 3.4 shows that a decrease in target oligonucleotide concentration is accompanied by a decrease in QD fluorescence signal. This decrease is also observable through fluorescence images of representative beads. It should be noted that even with blocking and washing, beads incubated with QD

alone and no target oligonucleotide had a non-zero signal. In fact a faint QD signal could be detected on the bead surface in fluorescence images of this sample (Figure 3.4C). This became the limiting factor for detection sensitivity as we were able to obtain a statistically significant signal for concentrations as low as 200 fM. While there was an observable difference in signal for the sample containing 20 fM target versus that containing no target, this difference was not statistically significant (p-value = .11 using the 2-tailed t-test).

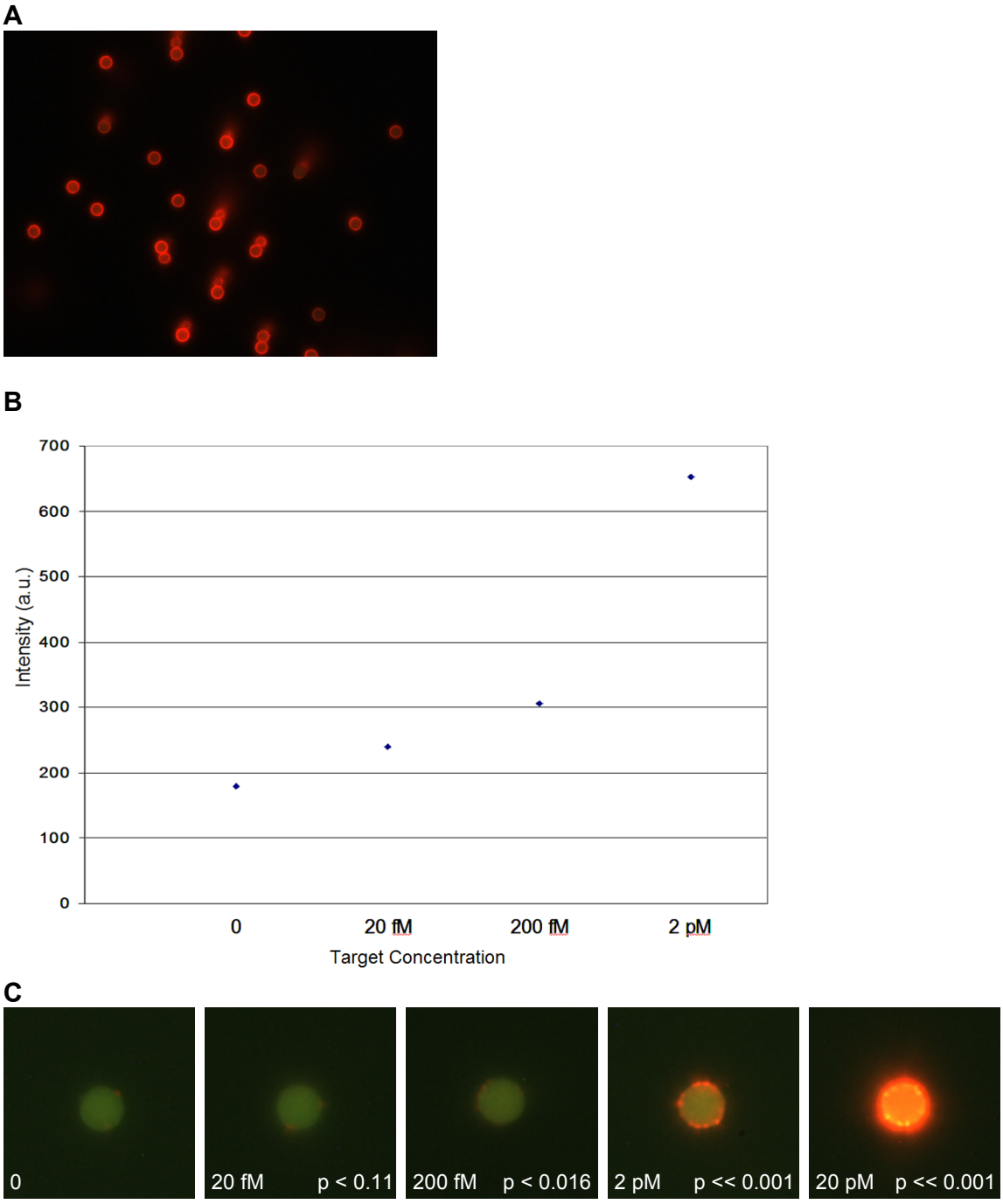

Figure 3.4: Single MMB hybridization assay for BRCA1 detection using QDs. (A) Representative image showing uniform coating of QDs on MMBs. (B) and (C) Results of assay when incubated with varying target DNA concentrations.

A 200 fM concentration of target DNA represents approximately 100 target DNA, and hence ideally 100 QDs per MMB. Of course, the actual number of QDs tethered to each bead by a target DNA may not be 100 for the 200 fM target concentration case, potentially due to a variety of reasons. First, there will be a population of QDs that are conjugated to more than one Probe 1. QD-Probe 1 conjugation was performed at a 1:1.5 molar ratio. Gel electrophoresis experiments have demonstrated that while a discrete band appears indicating what may be a 1:1 conjugation ratio, a smear still exists, indicating a heterogeneous population. QDs with more than one Probe 1 attached may either tether to the magnetic beads through more than one site or may otherwise simply sequester target DNA that will be unable to be bound to beads due to steric or other influences. Second, there is the possibility that after conjugation and purification, some of the conjugated probes may detach from either the QD or MMB. Free oligonucleotide probes will hybridize to target oligos and compete with QD- or MMB-bound probes. Lastly, as the concentrations of probes and target DNA are relatively low, there is the possibility that hybridization just does not occur as not all molecules are able to find each other. This could be resolved by increasing concentrations of Probe 1-bound QDs or of Probe 2-bound MMBs, but higher concentrations could also lead to increased nonspecific binding.

We have demonstrated in this study a method to semi-quantitatively detect a cancer-associated DNA sequence in solution. We were able to achieve detection sensitivity to as low as 200 fM. Below this level, signal did not differ significantly from that observed from nonspecific interactions. The detection limit of this method may be improved by using fewer MMBs or by further optimizing the assay to lower nonspecific interactions. This assay has potential applications in disease diagnosis

and monitoring of therapeutic response as oligonucleotide biomarkers as detected in bodily fluids have demonstrated such clinical value [32, 33].

3.4 References

1. *Cancer Facts and Figures 2009*. 2009, American Cancer Society: Atlanta, GA.

2. Etzioni, R., et al., *The case for early detection.* Nature Reviews Cancer, 2003. **3**(4): p. 243-252.

3. Levenson, V.V., *Biomarkers for early detection of breast cancer: What, when, and where?* Biochimica Et Biophysica Acta-General Subjects, 2007. **1770**(6): p. 847-856.

4. Swarup, V. and M.R. Rajeswari, *Circulating (cell-free) nucleic acids - A promising, non-invasive tool for early detection of several human diseases.* Febs Letters, 2007. **581**(5): p. 795-799.

5. Dong, S.M., et al., *Detecting colorectal cancer in stool with the use of multiple genetic targets.* Journal of the National Cancer Institute, 2001. **93**(11): p. 858-865.

6. Chan, K.C.A. and Y.M.D. Lo, *Circulating tumour-derived nucleic acids in cancer patients: potential applications as tumour markers.* British Journal of Cancer, 2007. **96**(5): p. 681-685.

7. Leon, S.A., et al., *FREE DNA IN SERUM OF RHEUMATOID-ARTHRITIS PATIENTS.* Journal of Rheumatology, 1977. **4**(2): p. 139-143.

8. Sorenson, G.D., et al., *SOLUBLE NORMAL AND MUTATED DNA-SEQUENCES FROM SINGLE-COPY GENES IN HUMAN BLOOD.* Cancer Epidemiology Biomarkers & Prevention, 1994. **3**(1): p. 67-71.

9. Vasioukhin, V., et al., *POINT MUTATIONS OF THE N-RAS GENE IN THE BLOOD-PLASMA DNA OF PATIENTS WITH MYELODYSPLASTIC SYNDROME OR ACUTE MYELOGENOUS LEUKEMIA.* British Journal of Haematology, 1994. **86**(4): p. 774-779.

10. Hibi, K., et al., *Molecular detection of genetic alterations in the serum of colorectal cancer patients.* Cancer Research, 1998. **58**(7): p. 1405-1407.

11. Chen, X.Q., et al., *Microsatellite alterations in plasma DNA of small cell lung cancer patients.* Nature Medicine, 1996. **2**(9): p. 1033-1035.

12. Nawroz, H., et al., *Microsatellite alterations in serum DNA of head and neck cancer patients.* Nature Medicine, 1996. **2**(9): p. 1035-1037.

13. Tagle, D.A., et al., *MAGNETIC BEAD CAPTURE OF EXPRESSED SEQUENCES ENCODED WITHIN LARGE GENOMIC SEGMENTS.* Nature, 1993. **361**(6414): p. 751-753.

14. Wang, J., et al., *Magnetic bead-based label-free electrochemical detection of DNA hybridization.* Analyst, 2001. **126**(11): p. 2020-2024.

15. Agrawal, A., T. Sathe, and S.M. Nie, *Single-bead immunoassays using magnetic microparticles and spectral-shifting quantum dots.* Journal of Agricultural and Food Chemistry, 2007. **55**(10): p. 3778-3782.

16. Diehl, F., et al., *BEAMing: single-molecule PCR on microparticles in water-in-oil emulsions.* Nature Methods, 2006. **3**(7): p. 551-559.

17. Diehl, F., et al., *Detection and quantification of mutations in the plasma of patients with colorectal tumors.* Proceedings of the National Academy of Sciences of the United States of America, 2005. **102**(45): p. 16368-16373.

18. Xu, H., et al., *Magnetically assisted DNA assays: high selectivity using conjugated polymers for amplified fluorescent transduction.* Nucleic Acids Research, 2005. **33**(9).

19. Agrawal, A., et al., *Counting single native biomolecules and intact viruses with color-coded nanoparticles.* Analytical Chemistry, 2006. **78**(4): p. 1061-1070.

20. Smith, A.M. and S.M. Nie, *Chemical analysis and cellular imaging with quantum dots.* Analyst, 2004. **129**(8): p. 672-677.

21. Smith, A.M., X.H. Gao, and S.M. Nie, *Quantum dot nanocrystals for in vivo molecular and cellular imaging.* Photochemistry and Photobiology, 2004. **80**(3): p. 377-385.

22. Alivisatos, P., *The use of nanocrystals in biological detection.* Nature Biotechnology, 2004. **22**(1): p. 47-52.

23. Dahan, M., et al., *Diffusion dynamics of glycine receptors revealed by single-quantum dot tracking.* Science, 2003. **302**(5644): p. 442-445.

24. Rasband, W.S., *ImageJ 1.42q*, NIH.

25. Gotoh, T., et al., *p130(Cas) regulates the activity of AND-34, a novel Ra1, Rap1, and R-Ras guanine nucleotide exchange factor.* Journal of Biological Chemistry, 2000. **275**(39): p. 30118-30123.

26. Near, R.I., et al., *AND-34/BCAR3 differs from other NSP homologs in induction of anti-estrogen resistance, cyclin D1 promoter activation and altered breast cancer cell morphology.* Journal of Cellular Physiology, 2007. **212**(3): p. 655-665.

27. Makkinje, A., et al., *AND-34/BCAR3 regulates adhesion-dependent p130Cas serine phosphorylation and breast cancer cell growth pattern.* Cellular Signalling, 2009. **21**(9): p. 1423-1435.

28. Schuh, N.R., et al., *BCAR3 Regulates Src/p130(Cas) Association, Src Kinase Activity, and Breast Cancer Adhesion Signaling.* Journal of Biological Chemistry, 2010. **285**(4): p. 2309-2317.

29. van Agthoven, T., et al., *Identification of BCAR3 by a random search for genes involved in antiestrogen resistance of human breast cancer cells.* Embo Journal, 1998. **17**(10): p. 2799-2808.

30. Pellegrino, T., et al., *Gel electrophoresis of gold-DNA nanoconjugates.* Journal of Biomedicine and Biotechnology, 2007.

31. Tholouli, E., et al., *Imaging of multiple mRNA targets using quantum dot based in situ hybridization and spectral deconvolution in clinical biopsies.* Biochemical and Biophysical Research Communications, 2006. **348**(2): p. 628-636.

32. Mehra, N., et al., *Circulating mitochondrial nucleic acids have prognostic value for survival in patients with advanced prostate cancer.* Clinical Cancer Research, 2007. **13**(2): p. 421-426.

33. Fiegl, H., et al., *Circulating tumor-specific DNA: A marker for monitoring efficacy of adjuvant therapy in cancer patients.* Cancer Research, 2005. **65**(4): p. 1141-1145.

CHAPTER 4

SYNTHESIS AND CHARACTERIZATION OF AMINE-FUNCTIONALIZED IRON OXIDE NANOPARTICLES

4.1 Introduction

With the completion of the human genome project and the increasing understanding of the genetic basis of disease, enormous interest has emerged in the possibility of treating disease at the genetic level. Among promising therapeutic agents, oligonucleotides such as siRNA, antisense, and microRNA antagonists and mimics stand out for their superior specificity and ease of use [1, 2]. Antisense has already entered clinical practice while numerous clinical trials of siRNA and microRNA-based drugs are underway [3, 4].

There is a widespread consensus in the field that the full potential of oligonucleotides as therapeutic agents will not be realized until better methodologies for targeted delivery to cells and tissues are developed. Numerous approaches have been developed over the years including chemical modification of the oligonucleotide [5, 6], viral vectors [7, 8], polymer carriers [9, 10], and nanoparticles [11-13]. Oligonucleotide modification and viral vectors are both relatively costly and time-consuming strategies. Viral vectors, in particular, also suffer from high toxicity and immunogenicity. Polymeric carriers such as cationic compounds are relatively cost-efficient, have low toxicity, and have potential for large-scale production, making them promising candidates for oligonucleotide delivery. Nanoparticle delivery vehicles make use of polymeric carriers by employing them as a coating over an

inorganic nanoparticle that may be used for targeting and tracking, thus creating a multifunctional delivery system.

Cationic polymers have emerged as a leading candidate for oligonucleotide delivery given its advantages of biocompatibility, low cost, scalability, and versatility (can load any oligonucleotide cargo by simple mixing). Moreover, they can be used to coat a nanoparticle for multifunctionality. A major limitation in their use, however, is their relatively lower transfection efficiency relative to viruses. Numerous studies have been published to date demonstrating utility of a wide variety of polymeric carriers but little has been done to directly compare polymers to evaluate factors for rational design [14-19].

Cationic polymers successfully deliver oligonucleotides due to a variety of properties. They bind DNA/RNA through electrostatic interaction, facilitate cell internalization through electrostatic adsorption on the cell membrane, and provide proton buffering capacity for endosomal escape through the proton sponge effect [20-22].

The amine groups responsible for these cationic and proton buffering capacities, however, need to be balanced. The polymer needs to have many high pK_a ($pK_a > 7$) amine groups to provide a strong cationic charge for oligonucleotide binding but not too strong for intracellular release. These high pK_a amines, however, need to be balanced with lower pK_a amines that provide proton buffering capacity. Past studies examining this balance by testing combinatorial libraries of polymers containing varying ratios of high pK_a and low pK_a cationic groups have only examined plasmid DNA (pDNA) rather an oligonucleotides [23, 24]. Moreover, these studies covered free polymers rather than polymer-coated inorganic nanoparticles. These distinctions are important because pDNA is significantly larger than

oligonucleotides and must be delivered to the nucleus rather than to the cytoplasm [25]. Also, free polymers will have amine functional groups located somewhat uniformly throughout the entire polymer whereas polymer-coated nanoparticles may have amine functional groups only on the surface of the particle, which may affect how the particles interact with the biological environment.

In this chapter, we will prepare iron oxide nanoparticles containing combinations of high pK_a and low pK_a amines. We will begin by evaluating the pH behavior of these amine molecules. The amines will then be reacted with iron oxide nanoparticles to create a panel of SPIONs containing different amine combinations. These particles will be characterized and their ability to bind DNA will be evaluated in preparation for in vitro transfection studies to be performed in Chapter 5.

4.2 Methods

Materials

Water-soluble 50 nm iron oxide nanoparticles with a glucuronic acid matrix coating were purchased from Chemicell Inc (Berlin, Germany). Particles had a core size of approximately 10 nm (from TEM) and an overall hydrodynamic size of approximately 40 nm (from DLS), which were independently obtained. Secondary amine (N-Methyl-1,3-diaminopropane), tertiary amine (3-(dimethylamino)-1-propylamine), imidazole (1-(3-Aminopropyl)imidazole), DPTA (N,N-Dimethyldipropylenetriamine), and EDC (1-Ethyl-3-(3-dimethylaminopropyl)carbodiimide) were purchased from Sigma-Aldrich (St. Louis, MO). Fluorescein-labeled DNA with the sequence 5'-6FAM-ACCCAGTAGCCAGATGTAGCT-3' was purchased from Sigma.

Particle Conjugation

Glucuronic acid-coated iron oxide nanoparticles were conjugated to amine molecules by carbodiimide reaction. 50 ul of 50 nm particles were added to a 750,000-fold molar excess of amine molecules to particles in 0.2 M borate buffer. The pH was adjusted for each reaction mixture to approximately pH 5.5 after addition of amines. EDC was then added and the reaction mixture was allowed to incubate at room temperature for 1 hour. The pH of the mixture was raised to >8 by addition of NaOH to quench any O-acylisourea intermediates and incubated for 10 minutes. The zeta potential was then measured for each particle sample (Zetasizer Nano ZS90, Malvern Instruments, Worcestershire, UK). Sequential lowering the pH to 5.5, addition of EDC, raising the pH > 8, and zeta potential measurement was repeated until the zeta potential stabilized for all samples, indicating saturation of the nanoparticle surface with amines. DLS measurements of iron oxide samples were also determined for each sample using the Zetasizer Nano instrument.

TEM Imaging

For TEM observation of unconjugated nanoparticles, 5 uL of the samples were pipetted onto a carbon TEM grid. The solvents were slowly wicked away with filter paper after 15 minutes and the grids were then counterstained with a 1% phophotungstic acid solution (pH adjusted to 6) for 30 seconds. The staining solution was slowly wicked away and allowed to dry. Grids were then imaged by TEM (H-600, Hitachi, Japan) operating at an acceleration voltage of 80 kV.

DNA Binding

For DNA binding studies, 6pmol of fluorescein-labeled DNA was incubated in 1X MOPS buffer (pH 7) with varying amounts of amine-conjugated SPION. The

particles and DNA were allowed to complex overnight (12-18hours) at 4C. For aggregation/particle sizing experiments, the hydrodynamic sizes of the complexes were then determined by DLS. For DNA binding capacity experiments, the complexes were mixed with a 5X bromophenol blue loading buffer (400 ul solution prepared by mixing 200 ul 10X MOPS, 150 ul 1% bromophenol blue in water, and 50 ul 50% glycerol) and loaded onto a 0.8% agarose/0.1% Tween-20 gel in 1X MOPS. Gels were run for 15min at 120V in a and subsequently imaged with a UV transillumination system (BioRad, Hercules, CA).

4.3 Results and Discussion

Amine Molecules

Studies have shown that polymers containing amine groups are useful as vectors for cellular delivery of nucleic acids both for their ability to complex DNA and to effect cytoplasmic entry by the proton sponge effect. Different amine molecules, however, have different charge and buffering properties that may influence performance as oligonucleotide transfecting agents. Past studies examining different amine groups have supported the notion that a combination of both cationic and pH buffering groups may produce an optimal delivery vehicle for plasmid DNA [24, 26-28]. Leong et al. demonstrated that the transfection efficiency of a polymer containing only high pK_a amines could be enhanced 85-fold when co-delivered with chloroquine, a lysosomotropic agent, suggesting that endosomal escape was the rate-limiting step for this polymer [26]. Putnam et al. demonstrated that increasing the imidazole content of high pKa amine-containing polymers could enhance delivery; however polymers containing only imidazole showed some but suboptimal transfection efficiency, presumably due to weak pDNA binding [24].

To study the utility of various types of amine molecules, a total of four different amine-containing molecules were evaluated: a secondary amine molecule (2A), a tertiary amine molecule (3A), a molecule containing both secondary and tertiary amines (DPTA), and an imidazole- containing molecule (I) (Figure 4.1). Secondary and tertiary amines both have high pK_as in the range of pH 8-10, with tertiary amines having a slightly lower pK_a than secondary amines. Imadazoles have relatively low pK_as (pH 6-7).

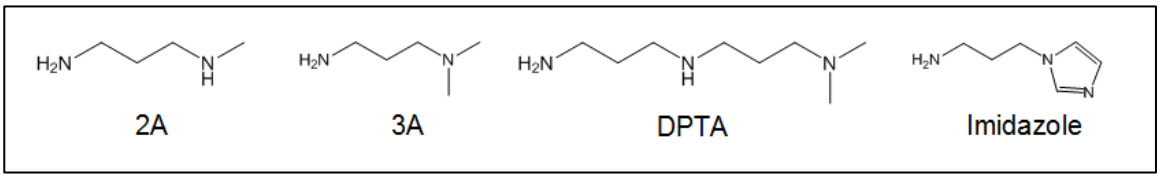

Figure 4.1: Molecular structures of amine molecules to be conjugated to nanoparticles. 2A = N-Methyl-1,3-diaminopropane; 3A = 3-(dimethylamino)-1-propylamine; DPTA = N,N-Dimethyldipropylenetriamine; Imidazole = 1-(3-Aminopropyl)imidazole

Figure 4.2 shows titration curves of the free molecules. Free amines were placed in pure water. The solution had an initially high pH due to the basic properties of the amine molecules. As HCl was added to the solution, the pH only exhibited small decreases as the amines were able to buffer pH through nitrogen protonation. Once the buffering capacity of the amine molecules are reached (i.e. when all the nitrogens are protonated) additional acid added to the solution will cause the pH to drop sharply. Interestingly the secondary and tertiary amines have very similar titration curves. They have relatively high pK_as, around pH 9, consistent with data reported in the literature. The titration curves show that at physiological pH

conditions, these molecules will have very little buffering capacity, as most of the nitrogens will be protonated, but will also thus be highly cationic.

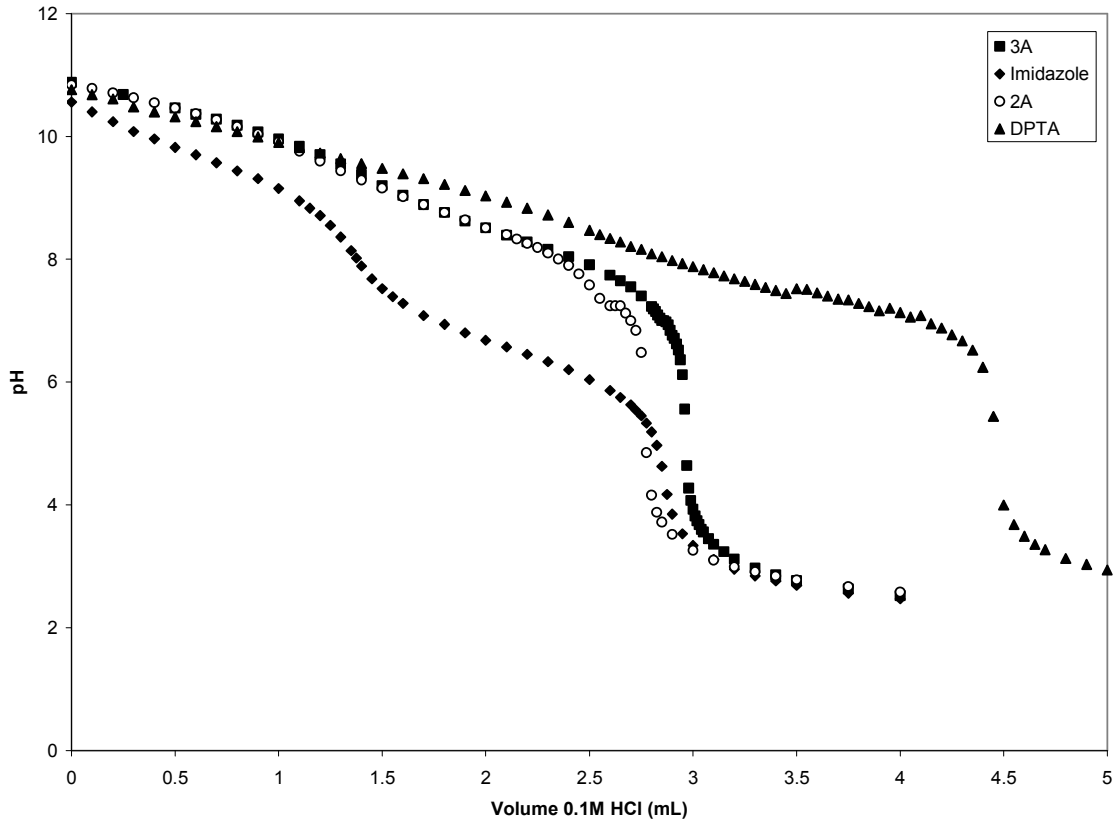

Figure 4.2: Titration curves for amine molecules.

The titration curve for imidazole has two sharp drops, corresponding to the different pKas of the two nitrogens in the five-membered ring. The first nitrogen has a high pK_a, around pH 9, similar to the pK_as of the secondary and tertiary amines. The second nitrogen, however, has a lower pK_a, around pH 6.5-7. Imidazole will thus have some cationic nature, due to one nitrogen, but will also have a significant proton buffering capacity due to the second nitrogen. As we go down titration the

curve from physiological pH the pH does not change significantly with additional acid. It is only at around pH 5.5 that the buffering capacity of imidazole is exhausted.

Although DPTA has two amine groups (besides the primary amine), like imidazole, the pKas for the secondary and tertiary amines are similar enough that two pH drops are not observed. Instead, only one is observed. The relative shape of DPTA's titration curve is very similar to that of 2A and 3A. The pKa is observed to be similar, although perhaps slightly lower, at around pH 8.5-9 with a sharp pH drop occurring at around pH 6.5-7, which is also slightly lower than for 2A or 3A. DPTA is thus still primarily a cationic molecule with much less buffering capacity than imidazole. The fact that it has both a 2A and 3A, however, will be useful in investigating the effect of additional cationic groups on oligonucleotide transfection.

The titration data is consistent with the expected pK_as for each of the molecules and highlights the weak buffering capacity of the 2A, 3A, and DPTA molecules at endosomal pH (pH 5-6.2). Imidazole, on the other hand, has a high buffering capacity at this pH. 2A, 3A, and DPTA, however, are highly cationic whereas imidazole is less so. Because the secondary and tertiary amine molecules have very similar titration curves, we decided to use only one of the two, 3A, for subsequent studies.

Iron Oxide Nanoparticles

Commercially available carboxyl-coated iron oxide nanoparticles were used as the base delivery vehicle to which the amine groups were attached. Particles were composed of magnetite (Fe_3O_4) with a glucuronic acid polymer matrix coating which contain carboxyl groups available for conjugation. TEM indicated the magnetite core was approximately 10 nm in diameter (Figure 4.3). DLS

measurements showed the particles had a significantly higher hydrodynamic diameter of 38.8 nm. The difference in TEM and DLS sizes can be attributed to a relatively thick polymer coating. Particles had a charge of -20.2 mV, consistent with an anionic carboxyl coating.

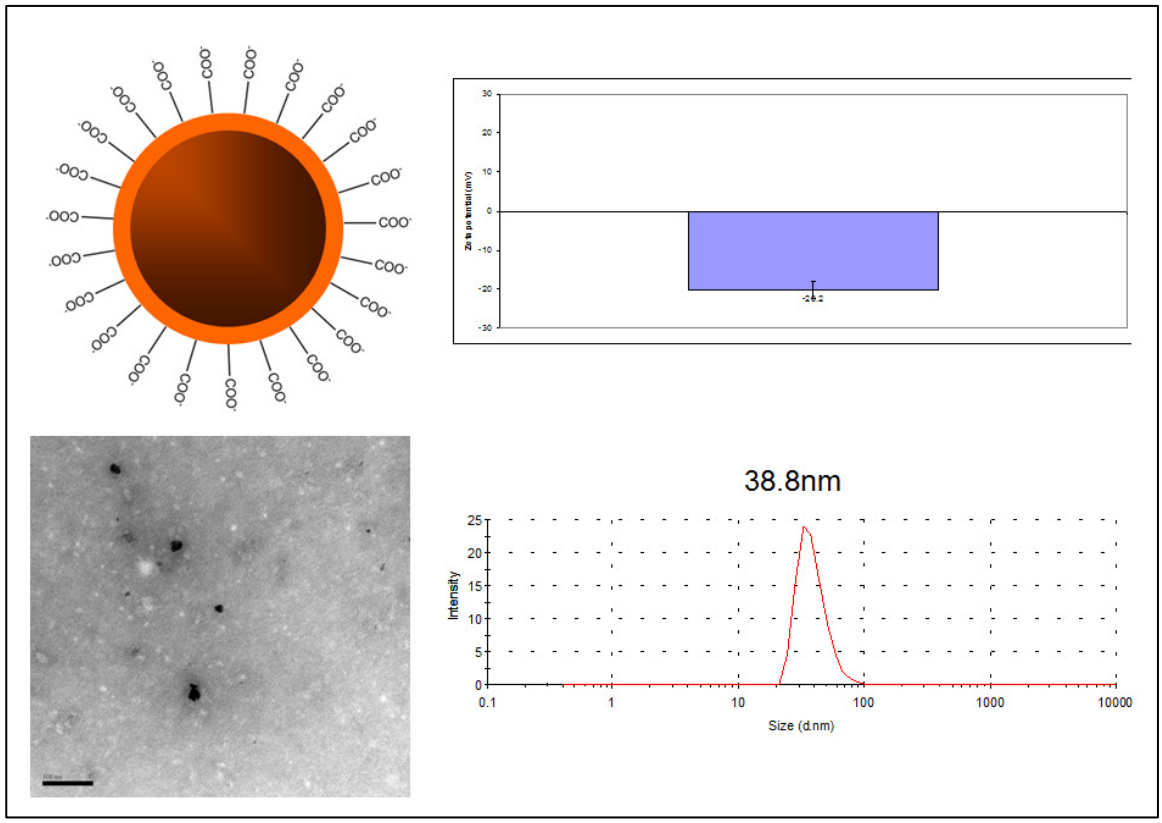

Figure 4.3: Characterization of unconjugated iron oxide particles. Schematic image showing particles coated carboxyl groups. Zeta potential of was -20.2mV. TEM and DLS data are also shown. Scale bar on TEM = 100 nm.

Amine-Nanoparticle Conjugation

Three amine molecules—3A, DPTA, and I—were combined in pairs in ratios of 25%/75%, 50%/50%, and 75%/25% (Table 4.1). These amine combinations, along with the pure amines themselves, were then reacted in excess with commercially available carboxyl-coated iron oxide nanoparticles using carbodiimide

chemistry (EDC) to generate a panel of 12 different nanoparticle coatings (Figure 4.4). EDC is frequently used to conjugate biomolecules such as antibodies and small molecule ligands to nanoparticles for targeting purposes. The chemistry, however, is difficult to control and does not give a 100% yield. This is appropriate for conjugating targeting molecules to nanoparticles because the amount of molecules conjugated is not as important as that molecules are conjugated at all; but this becomes an issue for this study because we want to know the composition of the nanoparticle surface. Performing the reaction only one time would yield a surface coating that is a mixture of amines and carboxyls in unknown ratios. To prevent having an unknown carboxyl composition, the reaction was repeated iteratively until almost all carboxyls were reacted.

Pure amines		100%3A	100%DPTA	100%I
Combinations	I/3A	25%I/75%3A	50%I/50%3A	75%I/25%3A
	I/DPTA	25%I/75%2DPTA	50%I/50%2DPTA	75%I/25%2DPTA
	3A/DPTA	25%3A/75%DPTA	50%3A/50%DPTA	75%3A/25%DPTA

Table 4.1: The 12 particle coatings to be prepared and evaluated.

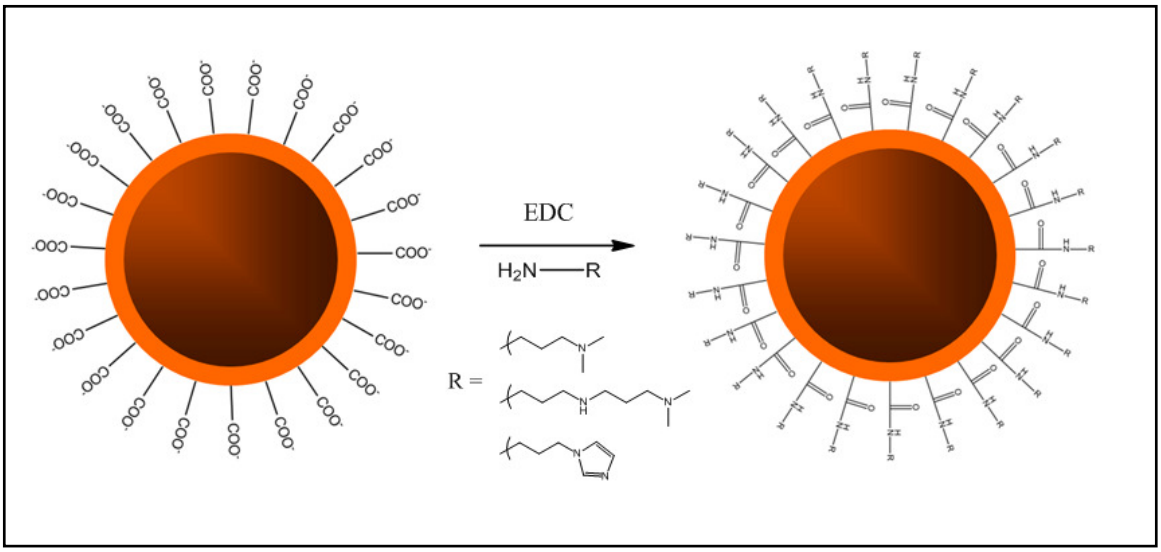

Figure 4.4: Reaction scheme for conjugating amine molecules onto SPIONs.

The extent of reaction was monitored by measuring zeta potential. Because carboxyl groups are anionic and amine groups are cationic, the surface charge will increase as the reaction progresses. Over iterative reactions, the charge should eventually plateau at a positive value, indicating saturation of the iron oxide surface with amines. Figure 4.5 shows our results. Unconjugated nanoparticles had a surface charge of -20.2 mV, consistent with the anionic character of the carboxylic acid coating. As the amines were conjugated the zeta potential became positive and eventually plateued around +20mV.

Interestingly, there did not appear to be a significant difference in the plateau charges for the different particles. As was discussed earlier, imidazole is less cationic than tertiary amines and would be expected to have a lower positive charge. It should be noted, however, that the zeta measurements were performed in deoinized water (pH 5). This acidic pH is below the pK_a of all amine molecules tested and thus all amines should be fully protonated, eliminating charge differences due to

differing pK_a. Also of note, there did not seem to be a large difference in saturated surface charge for the amine coatings with only one amine group per molecule (3A) versus those with two amine groups per molecule (DPTA or I). This is may be due to the fact that zeta measures only the surface charge. The second amine of DPTA and imidazole may be buried deeply enough to not significantly affect the zeta.

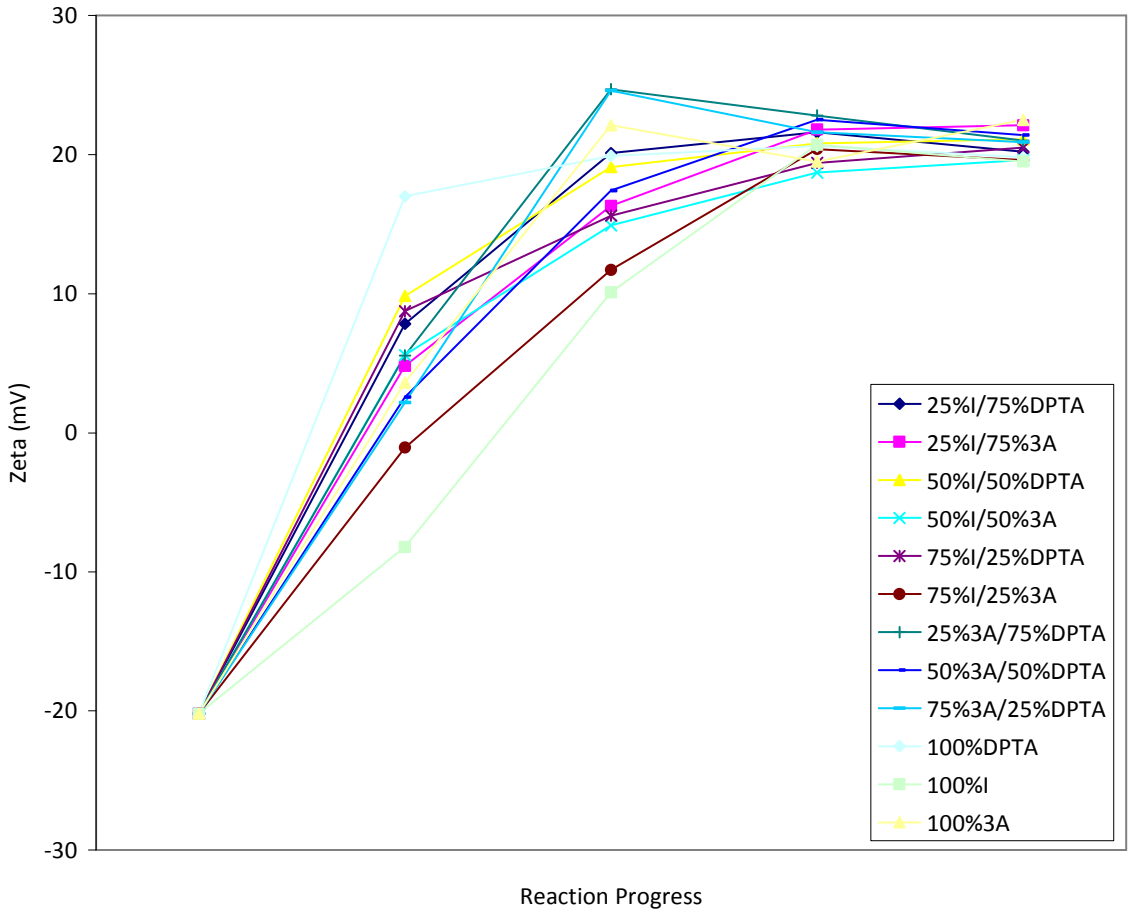

Figure 4.5: Zeta potential measurements to evaluate extent of amine reaction onto SPIONs. Zeta saturation was taken to indicate saturation of particle surface with amines.

Hydrodynamic sizes of reacted particles were determined by dynamic light scattering to see if differences in composition affected size (Figure 4.6). While there was some variability in particle sizes, the differences were within measurement error. Coating composition thus did not seem to affect particle size and particles remained discrete at around 35-40 nm. Interestingly, size did not change appreciably after amine conjugation, which involved a charge reversal. The sizes of the different amine particles also did not seem to differ significantly, even though some particles (DPTA-coated) had twice the number of cations of other particles (3A-coated).

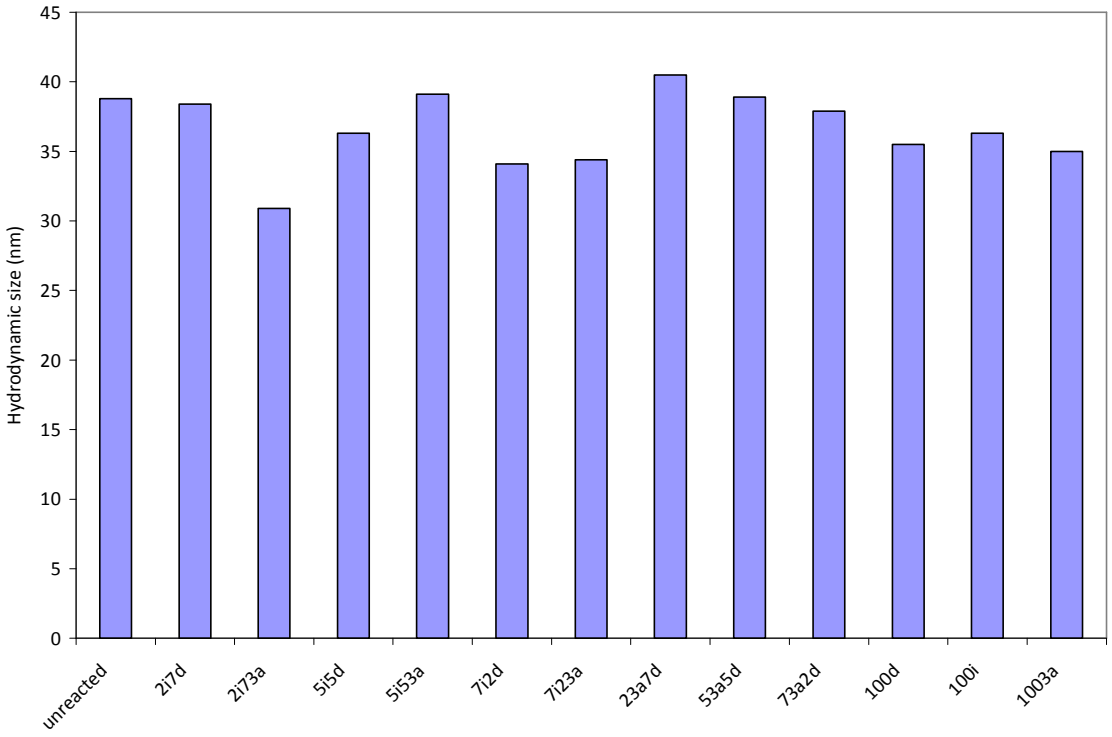

Figure 4.6: Dynamic light scattering measurements of amine-conjugated SPIONs.

DNA-Nanoparticle Binding

With the particles prepared and characterized, we investigated the DNA binding properties of the particles. For transfection to occur, the iron oxide nanoparticles need to bind to the DNA oligonucleotides. As stated before, the advantage of using amines is they are cationic and can be used to bind DNA electrostatically by its negatively charged phosphate groups. To study oligonucleotide binding properties, particles were incubated with a fluorescein-labeled DNA oligonucleotide at DNA-IO ratios of 500:1, 200:1, 100:1, 50:1, 20:1, and 10:1. The DNA oligonucleotide contained 21 bases and had sequence identicality to the DNA used for transfection in the following chapter. After incubating the nanoparticles and DNA, samples were loaded onto an agarose gel and electrophoresis was performed. Results for all 12 nanoparticle samples are shown in Figure 4.7.

The first lane in all gels contains only fluorescein-labeled DNA. As expected, the DNA migrates down the gel towards the cathode due to its negatively charged phosphate groups. The remaining bands contain an identical amount of DNA but have increasing amounts of nanoparticles to match the labeled ratios. At a 500:1 DNA:IO ratio, the DNA band is still present, indicating that most of the DNA is unbound. As the relative amount of DNA to nanoparticle is decreased, the DNA band starts to disappear, indicating DNA binding by the iron oxide. At a 200:1 ratio, many of the gels contain a smear, possibly due to electrostatic interaction of the particles with the DNA that is strong enough to retard but not completely bind the oligonucleotides. At a 50:1 ratio, DNA seems to be completely bound for all nanoparticle samples tested. Indeed, while a 100:1 ratio seems sufficient in most of the gels, a faint band does appear for some, particularly for the particles having a

high imidazole content (e.g. 100I and 75 I/25 3A). It should be noted that at low DNA-IO ratios, the DNA band migrated towards the anode whereas the iron oxide cores remained inside the well. The polymer coating was thus probably stripped off of the nanoparticles cores while remaining bound to the DNA.

Determining DNA binding capacity by this method is important both for ascertaining the amount of iron oxide needed to fully bind DNA for our transfection studies in the next chapter as well as for giving some idea of the relative DNA binding strengths of the particles. The data may suggest that the particles containing high levels of imidazole have somewhat weaker oligonucleotide binding potentially due to its lower cationic properties relative to 3A or DPTA at the neutral pH at which these experiments were performed. More importantly, however, the data shows that the DNA binding capacity of all particles tested is at least 50 oligonucleotides per particle. We will thus use this ratio for future *in vitro* cellular experiments.

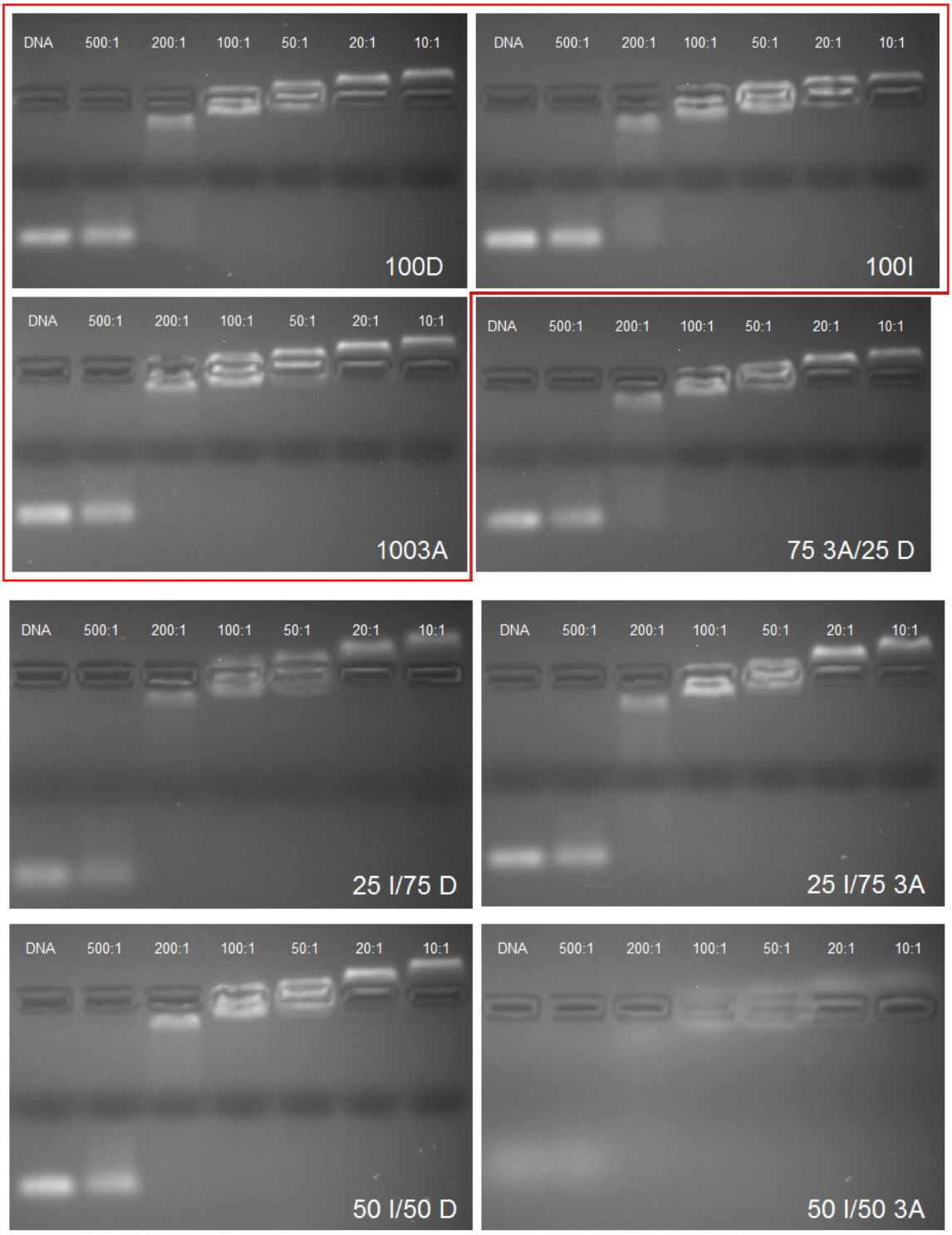

Figure 4.7: Gel electrophoresis assays showing oligonucleotide loading onto amine-coated SPIONs. Three gels in red box at top indicate particles containing only one type of amine each. Numbers preceding D/I/3A indicate percentages of each amine molecule on the coating.

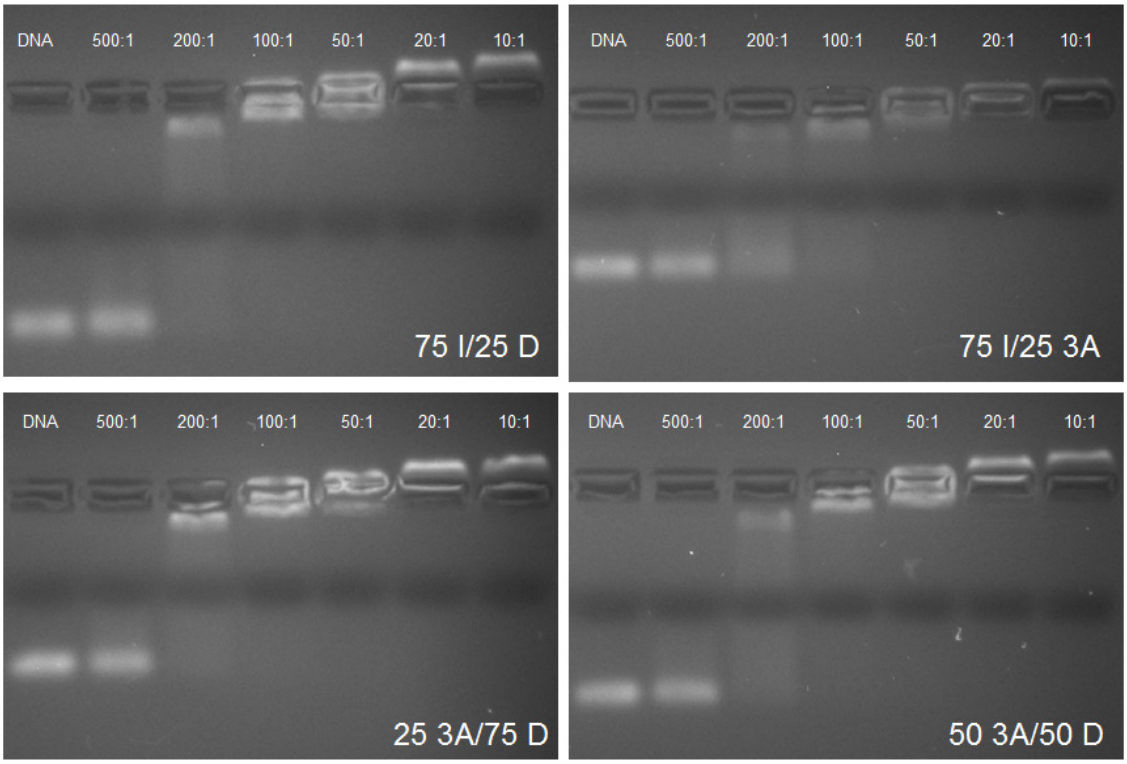

Figure 4.7 (continued)

Having performed the DNA binding experiments and having determined the binding capacity of our particles, we wanted to verify that addition of the DNA does not cause the iron oxide nanoparticles to aggregate. Because the positive and negative charges exist throughout both the iron oxide nanoparticles and DNA, respectively, there is the potential for a single DNA to be bound by multiple nanoparticles, causing aggregation, which may compromise later cellular experiments. Aggregation is particularly likely when using high DNA:IO ratios such as the 50:1 that the gel experiments suggested. To assay for particle aggregation in the presence of DNA, DNA and 100%3A iron oxide nanoparticles were again incubated at various ratios. The hydrodynamic sizes of the complexes were then determined by DLS. Figure 4.8 shows that for all ratios tested, including a 100:1 DNA:IO ratio, no aggregation was observed. Hydrodynamic sizes of DNA:IO

complexes did not differ significantly from the size of pure 100%3A particles alone. Any differences in size among the samples tested were within standard error.

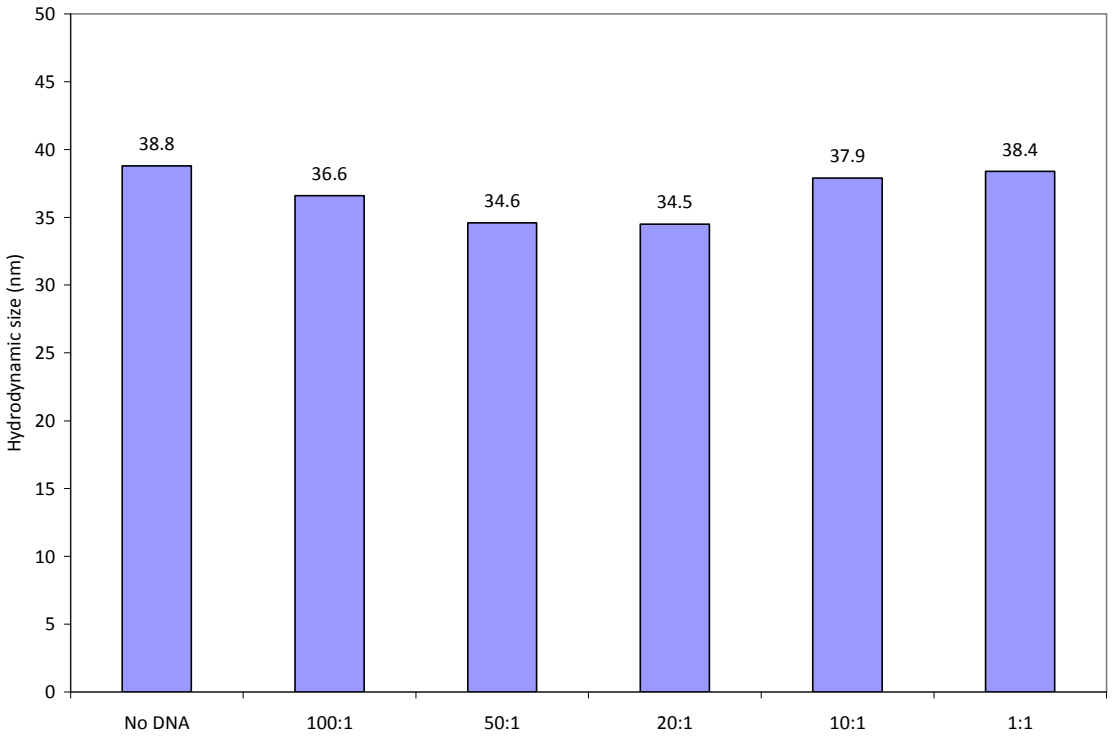

Figure 4.8: Dynamic light scattering measurements of DNA-SPION complexes. DNA loading did not cause aggregation of particles. X-axis labels indicate DNA:SPION ratios.

We have demonstrated in this chapter that we can prepare different amine-coated SPIONs using EDC reaction. We have confirmed successful reaction by measuring the zeta potential and observing its increase to around +20 mV. Conjugated particles were stable and discrete, demonstrated by their hydrodynamic diameters being unchanged from their preconjugated forms. Further, they remained stable even after addition of negatively-charged oligonucleotides. Gel binding studies

indicate that all particles had oligonucleotide binding capacities of at least 50 DNA/SPION.

4.4 References

1. Lee, S.H., et al., *Amine-functionalized gold nanoparticles as non-cytotoxic and efficient intracellular siRNA delivery carriers.* International Journal of Pharmaceutics, 2008. **364**(1): p. 94-101.

2. Juliano, R., et al., *Biological Barriers to Therapy with Antisense and siRNA Oligonucleotides.* Molecular Pharmaceutics, 2009. **6**(3): p. 686-695.

3. de Fougerolles, A., et al., *Interfering with disease: a progress report on siRNA-based therapeutics.* Nature Reviews Drug Discovery, 2007. **6**(6): p. 443-453.

4. Wahid, F., et al., *MicroRNAs: Synthesis, mechanism, function, and recent clinical trials.* Biochimica Et Biophysica Acta-Molecular Cell Research, 2010. **1803**(11): p. 1231-1243.

5. Yu, B., et al., *Targeted Delivery Systems for Oligonucleotide Therapeutics.* Aaps Journal, 2009. **11**(1): p. 195-203.

6. Krutzfeldt, J., et al., *Silencing of microRNAs in vivo with 'antagomirs'.* Nature, 2005. **438**(7068): p. 685-689.

7. Xia, H.B., et al., *siRNA-mediated gene silencing in vitro and in vivo.* Nature Biotechnology, 2002. **20**(10): p. 1006-1010.

8. Qin, X.F., et al., *Inhibiting HIV-1 infection in human T cells by lentiviral-mediated delivery of small interfering RNA against CCR5.* Proceedings of the National Academy of Sciences of the United States of America, 2003. **100**(1): p. 183-188.

9. Roth, C.M. and S. Sundaram, *Engineering synthetic vectors for improved DNA delivery: Insights from intracellular pathways.* Annual Review of Biomedical Engineering, 2004. **6**: p. 397-426.

10. Mintzer, M.A. and E.E. Simanek, *Nonviral Vectors for Gene Delivery.* Chemical Reviews, 2009. **109**(2): p. 259-302.

11. Yezhelyev, M.V., et al., *Proton-sponge coated quantum dots for siRNA delivery and intracellular imaging.* Journal of the American Chemical Society, 2008. **130**(28): p. 9006-9012.

12. Song, W.J., et al., *Gold Nanoparticles Capped with Polyethyleneimine for Enhanced siRNA Delivery.* Small, 2010. **6**(2): p. 239-246.

13. Xia, T.A., et al., *Polyethyleneimine Coating Enhances the Cellular Uptake of Mesoporous Silica Nanoparticles and Allows Safe Delivery of siRNA and DNA Constructs.* Acs Nano, 2009. **3**(10): p. 3273-3286.

14. Meyer, M., et al., *Synthesis and Biological Evaluation of a Bioresponsive and Endosomolytic siRNA-Polymer Conjugate.* Molecular Pharmaceutics, 2009. **6**(3): p. 752-762.

15. Wu, Y., et al., *The investigation of polymer-siRNA nanoparticle for gene therapy of gastric cancer in vitro.* International Journal of Nanomedicine, 2010. **5**: p. 129-136.

16. Zhu, C.H., et al., *Co-delivery of siRNA and paclitaxel into cancer cells by biodegradable cationic micelles based on PDMAEMA-PCL-PDMAEMA triblock copolymers.* Biomaterials, 2010. **31**(8): p. 2408-2416.

17. Arima, H. and K. Motoyama, *Recent Findings Concerning PAMAM Dendrimer Conjugates with Cyclodextrins as Carriers of DNA and RNA.* Sensors, 2009. **9**(8): p. 6346-6361.

18. Rudzinski, W.E. and T.M. Aminabhavi, *Chitosan as a carrier for targeted delivery of small interfering RNA.* International Journal of Pharmaceutics, 2010. **399**(1-2): p. 1-11.

19. Convertine, A.J., et al., *Development of a novel endosomolytic diblock copolymer for siRNA delivery.* Journal of Controlled Release, 2009. **133**(3): p. 221-229.

20. Sonawane, N.D., F.C. Szoka, and A.S. Verkman, *Chloride accumulation and swelling in endosomes enhances DNA transfer by polyamine-DNA polyplexes.* Journal of Biological Chemistry, 2003. **278**(45): p. 44826-44831.

21. Haensler, J. and F.C. Szoka, *POLYAMIDOAMINE CASCADE POLYMERS MEDIATE EFFICIENT TRANSFECTION OF CELLS IN CULTURE.* Bioconjugate Chemistry, 1993. **4**(5): p. 372-379.

22. Behr, J.P., *GENE-TRANSFER WITH SYNTHETIC CATIONIC AMPHIPHILES - PROSPECTS FOR GENE-THERAPY.* Bioconjugate Chemistry, 1994. **5**(5): p. 382-389.

23. Green, J.J., R. Langer, and D.G. Anderson, *A combinatorial polymer library approach yields insight into nonviral gene delivery.* Accounts of Chemical Research, 2008. **41**(6): p. 749-759.

24. Wong, S.Y., N. Sood, and D. Putnam, *Combinatorial Evaluation of Cations, pH-sensitive and Hydrophobic Moieties for Polymeric Vector Design.* Molecular Therapy, 2009. **17**(3): p. 480-490.

25. Gary, D.J., N. Puri, and Y.Y. Won, *Polymer-based siRNA delivery: Perspectives on the fundamental and phenomenological distinctions from polymer-based DNA delivery.* Journal of Controlled Release, 2007. **121**(1-2): p. 64-73.

26. Wang, J., et al., *Polyphosphoramidate gene carriers: effect of charge group on gene transfer efficiency.* Gene Therapy, 2004. **11**(12): p. 1001-1010.

27. Putnam, D., et al., *Polymer-based gene delivery with low cytotoxicity by a unique balance of side-chain termini.* Proceedings of the National Academy of Sciences of the United States of America, 2001. **98**(3): p. 1200-+.

28. Chen, D.J., et al., *Structure-function relationships of gene delivery vectors in a limited polycation library.* Journal of Controlled Release, 2005. **103**(1): p. 273-283.

CHAPTER 5

A COMBINATORIAL EVALUATION OF AMINE COATINGS FOR NANOPARTICLE DELIVERY OF ANTAGOMIR

5.1 Introduction

MicroRNA are short, processed, RNA molecules around 22 nucleotides in length that can control gene function through mRNA degradation, translation inhibition or chromatin-based silencing mechanisms [1, 2]. Discovered in the 1990's, this class of biomolecule has gained attention as an important regulator as more than 1000 have been identified in humans so far [3]. The potential involvement of miRNA in human disease might be inferred from even the first studies of miRNA function. The lin-4 and let-7 phenotypes observed in *C. elegans* can be described as proliferative defects and the roles of bantam and miR-14 in *D. melanogaster* also points to defects in proliferation [4-8]. Indeed, miRNA have been found to be involved in development, proliferation, differentiation, and apoptosis, all functions important in several diseases, including cancer [9-12]. MicroRNAs have been found to play oncogenic and tumor suppressor roles [13] and are de-regulated in many primary human tumors [14-17]. These studies suggest that miRNA may be promising as a therapeutic target. In fact, both miRNA antagomirs and mimics have been reported in the literature [18-21]. As for other oligonucleotide drugs, miRNA-based drugs require a delivery method for their full promise to be realized [22].

In this chapter, we will use the panel of SPIONs prepared in Chapter 4 and evaluate their efficacy in delivering an antagomir against a cancer-related microRNA,

miR-222. This represents the first study demonstrating the use of nanoparticles for delivering antagomirs into cells. Results will shed light on optimal amine combinations for antagomir delivery, which could have implications for delivery of other oligonucleotides such as siRNA and antisense. We will also use TEM and fluorescence microscopy techniques to visualize the transfection process.

5.2 Methods

DNA Transfection

PC-3 cells were grown in RPMI 1640 buffer and plated on a 96-well plate at about 5000 cells/well. Delivery agents were prepared by the following. IO nanoparticles were incubated with LNA antagomirs against miR-222 at a 1:50 IO:LNA ratio overnight in PBS. Antagomirs had the sequence 5'-accCagTagCcaGatGtaGct-3' where capitalized bases are LNA-modified (Integrated DNA Technologies, Coralville, IA). PEI-LNA complexes were prepared by incubating PEI with LNA at an N:P ratio of 8 overnight. Following overnight incubation, complexes were diluted in Opti-MEM (Invitrogen). LNA transfection by Lipofectamine 2000 was also performed according to the manufacturer's instructions, with liposome complexes prepared the day of transfection.

After 24 hours of cell growth on the 96-well plate, cells were washed in PBS and delivery agents were added to yield a 40nM LNA concentration in Opti-MEM buffer (Invitrogen). Cells were incubated with delivery agents for 4hrs before washing in PBS. Twenty-four hours post-transfection, cells were lysed and RNA enriched for short sequences was collected using the miRvana RNA Isolation Kit (Ambion). All transfections were carried out in triplicate.

Real-time PCR and Data Analysis

RNA samples were reverse transcribed using the Taqman® MicroRNA Reverse Transcription Kit (Applied Biosystems, Foster City, CA). Real-time PCR was the performed on the reverse transcription product using the TaqMan MicroRNA Assay according to the manufacturer's instructions (Applied Biosystems). Data was normalized by U6B small nuclear RNA as an endogenous control (RNU6B, from Applied Biosystems, Foster City, CA). After normalizing expression data to RNU6B, data was further normalized to no transfection control. Student t-test was performed to test for significance.

TEM Imaging

For TEM examination of the monolayer cells, cells cultured in 6-well tissue culture plates were incubated with antagomir-nanoparticle complexes for four hour before being replaced with full media. Cells were fixed 24 hours post-transfection by incubating overnight in 2.5% glutaraldehyde in 0.1 M cacodylate buffer (pH 7.2) at 4C. Cells were then washed with the same buffer and post-fixed in 1% buffered osmium tetroxide, dehydrated through a graded ethanol series to 100%, and embedded in Eponate 12 resin (Ted Pella Inc., Redding, CA). Ultrathin sections were cut on a Leica UC6rt Ultramicrotome (Leica Microsystems, Bannockburn, IL) at 70-80nm, and counter-stained with 4% aqueous uranyl acetate and 2% lead citrate. Sections were examined using a Hitachi H-7500 transmission electron microscope (Hitachi High Technologies of America, Inc., Pleasanton, CA) equipped with a Gatan BioScan CCD camera.

Bulk Fluorescence Measurements

Bulk absorbance measurements were performed using a spectrophotometer (Shimadzu UV-2401PC, Kyoto, Japan). Bulk emission measurements were performed using a standard fluorometer (FluoMax, Jobin Yvon, Edison, NJ). Fluorescence quenching of TYE665-labeled antagomir by SPIONs was performed by comparing emissions of a volume of fluorescent antagomir-SPION complex and a volume of free fluorescent antagomir with equal concentration.

Fluorescence Imaging

For fluorescence imaging studies, nanoparticle-LNA complexes were prepared and transfection performed as per the Transfection method described above, except using a TYE665-conjugated LNA oligonucleotide in place of the regular LNA and growing cells in LabTek II chamber slides rather than a 96-well plate. Cells were washed in 1X PBS 4 hours after nanoparticle-LNA complex exposure and then incubated with full medium. Twenty-four hours post-transfection, cells were washed twice briefly in PBS and fixed and permeabilized for 20 min in 4% paraformaldehyde supplemented with 0.1% Triton X-100. After briefly washing twice in PBS, blocking buffer (5% goat serum/2% BSA in 1X PBS) was added for 1 hour. Cells were washed again twice for 5 min each in 0.2% BSA/1X PBS before adding primary antibody against LAMP1 (Abgent, San Diego, CA) at a 6.25 ug/ml concentration diluted in 1% BSA/1X PBS for 45 minutes. Cells were washed 2X5 min again in 0.2% BSA/1X PBS and then incubated in Alexa Fluor 568-conjugated goat anti-rabbit secondary antibody (Invitrogen, Carlsbad, CA) at a 5ug/ml concentration in 2% BSA/1X PBS. Cells were then washed 2X5min in PBS before DAPI counterstaining. Slides were then mounted and coverslipped for imaging on a

Zeiss LSM 510 META confocal microscope. Images were analyzed using NIH Image J software [23].

5.3 Results and Discussion

To study the transfection efficiencies of our panel of nanoparticles, PC-3 prostate cancer cells were incubated with complexes of antagomir against miR-222 with each of the nanoparticles. miR-222 is a putative oncogenic microRNA that negatively regulates the p27 tumor suppressor protein [24]. Past studies have identified miR-222 overexpression in a variety of cancers, the majority of which is also known to be characterized by p27 loss or mutations. miR-222 overexpression has been identified in glioblastoma [25, 26], prostate carcinoma [24], solid tumors of the colon, pancreas, and stomach [27, 28], and are strongly-upregulated in papillary thyroid carcinoma and chronic lymphocytic leukemia [24, 29-31]. In a cell line model, miR-222 was found to be overexpressed in the PC-3 cellular model of aggressive prostate carcinoma, as compared with LNCaP and 22Rν1 cell line models of slowly growing carcinomas. Antagonism of miR-222 in PC-3 caused a reduction in clonogenicity [24].

The antagomir used had perfect complementarity to miR-222 and contained a number of locked nucleic acid (LNA) modified nucleotides (Figure 5.1). LNA nucleotides are chemically modified DNA nucleotides with a *2'-O,4'-C*-methylene bridge in the ribose ring (Figure 5.1B). This bridge conformationally locks the C3'-endo sugar conformation, which is ideal for RNA recognition [32, 33] (Figure 5.1A). LNA modifications increase the melting temperature of the antagomir:RNA duplex, which is important because binding strength is relatively weak for unmodified DNA:RNA duplexes with such short lengths [34, 35]. We designed our LNA

according to recommendations of spacing LNA-modified nucleotides at every third base and limited the number of LNA-modifications to keep the melting temperature from being too high, which could increase nonspecific binding [36, 37] (Figure 5.1C).

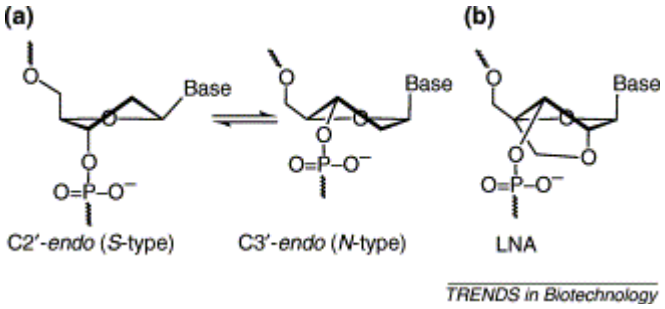

(c)

```
miR-222     3′- ugg guc auc ggu cua cau cga -5′
antagomir   5′- acc Cag Tag Cca Gat Gta Gct -3'
```

Figure 5.1: Chemical structures of LNA-modified nucleotides and miR-222 antagomir. (A) C2'-endo and C3'-endo conformations of ribose ring. C3'-endo is ideal for base pairing with RNA. (B) LNA structure showing ribose locked in C3'-endo conformation. (C) Sequences of miR-222 and miR-222 antagomir. LNA-modified bases are capitalized.

Antagomir Transfection

With the probe designed, nanoparticle-antagomir complexes were incubated with PC-3 cells. The real-time PCR results are shown in Figure 5.2. Data was normalized to the no transfection control. The data shows that the different particles had different transfection efficiencies, with miR-222 expression levels being 20-70% that of the control. Polyethyleneimine (PEI), the current standard polymeric gene delivery vector, had a miR-222 expression of around 73% of control, similar to the efficiencies reported by others for this compound [38]. 100%I coated nanoparticles seemed to perform the best, with a transfection efficiency of close to 80%. In

contrast, the particles containing 100%D and 100%3A seemed to perform the worst, with efficiencies around 50%. Interestingly, 100%D and 100%3A did not exhibit a statistically significant difference in transfection efficiency. The remaining particles seemed to vary in between these two values. It should be noted that all the particles performed as well as or better than PEI.

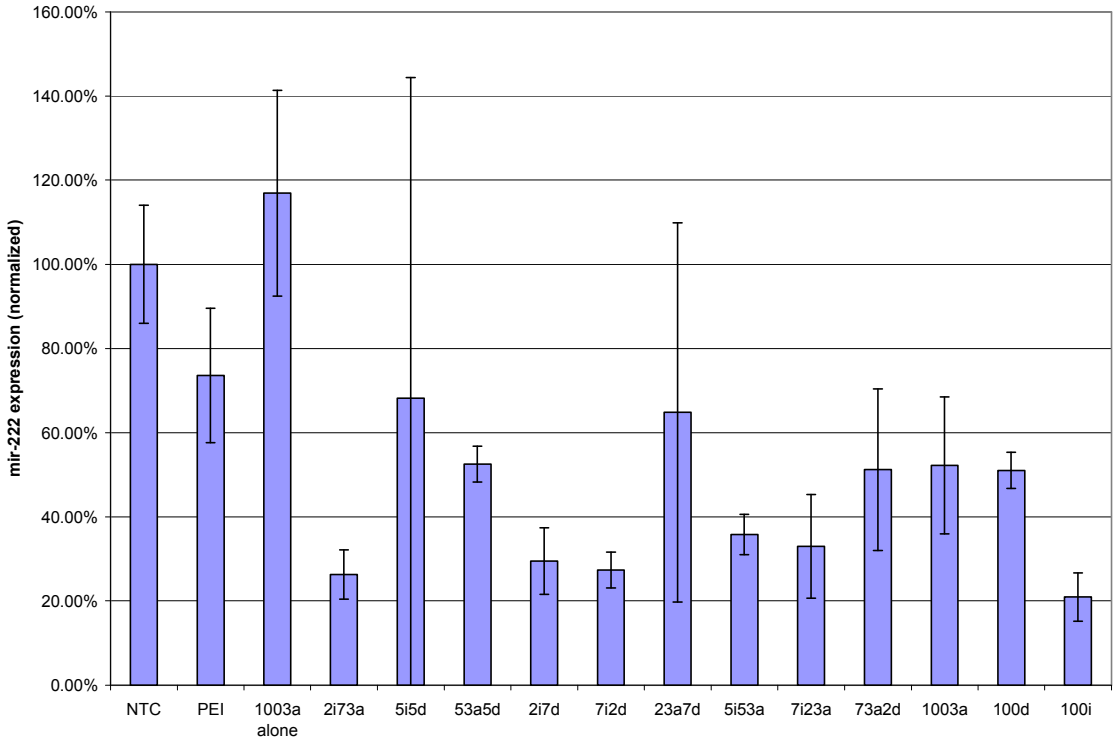

Figure 5.2: MiR-222 expression after antagomir transfection with amine-coated SPIONs. Data shows comparative c_T values, with RNU6B as endogenous control, normalized to NTC. NTC = no transfection control.

The data shows that imidazole performs better than either tertiary amine or DPTA, suggesting that the enhanced proton buffering ability inherent to imidazole enhances transfection. Moreover, the additional cationic group present on DPTA does not seem to significantly affect miR-222 antagonism. This is further illustrated

in Figure 5.3, which compares the relative transfection efficiencies of binary combinations of amines of different ratios. Figure 5.3A shows that 100%DPTA gives a relatively high miR-222 expression. As imidizole is added, replacing DPTA, miR-222 expression appears to decrease, reaching a minimum at 100%I. The expression difference between 100%DPTA and 100%I is statistically significant. While there may be a decrease in expression as imidazole is increased, the differences among the intermediate groups were mostly not statistically significant. Hence, it is not possible to conclude whether incremental improvements in miR-222 antagonism could be observed with incremental increases in imidizole content. We can conclude, however, that 100%I performs better than 100%D.

Similarly, Figure 5.2B shows the effect of increasing imidazole content relative to tertiary amine. Again, 100%3A gives a relatively high miR-222 expression which is improved with addition of imidazole. In fact, 100%I has about half the miR-222 expression of 100%3A, with the difference being statistically significant. The intermediate particles containing a mixture of imidazole and tertiary amine did not exhibit statistically significant differences from one another or from the single amine particles.

While the addition of proton buffering groups enhances miRNA antagonism, the addition of cationic groups appears to have no effect. Figure 5.3C shows the effect of replacing 3A by DPTA. These two molecules differ only by the fact that DPTA contains an additional secondary amine, which should increase the cationic character of this molecule, relative to 3A. Moving left to right on Figure 5.3C, 3A is replaced by DPTA, meaning that additional secondary amines are added onto the particles. MiR-222 expression, however, remains relatively constant at 50-60% and no statistically significant differences are observed.

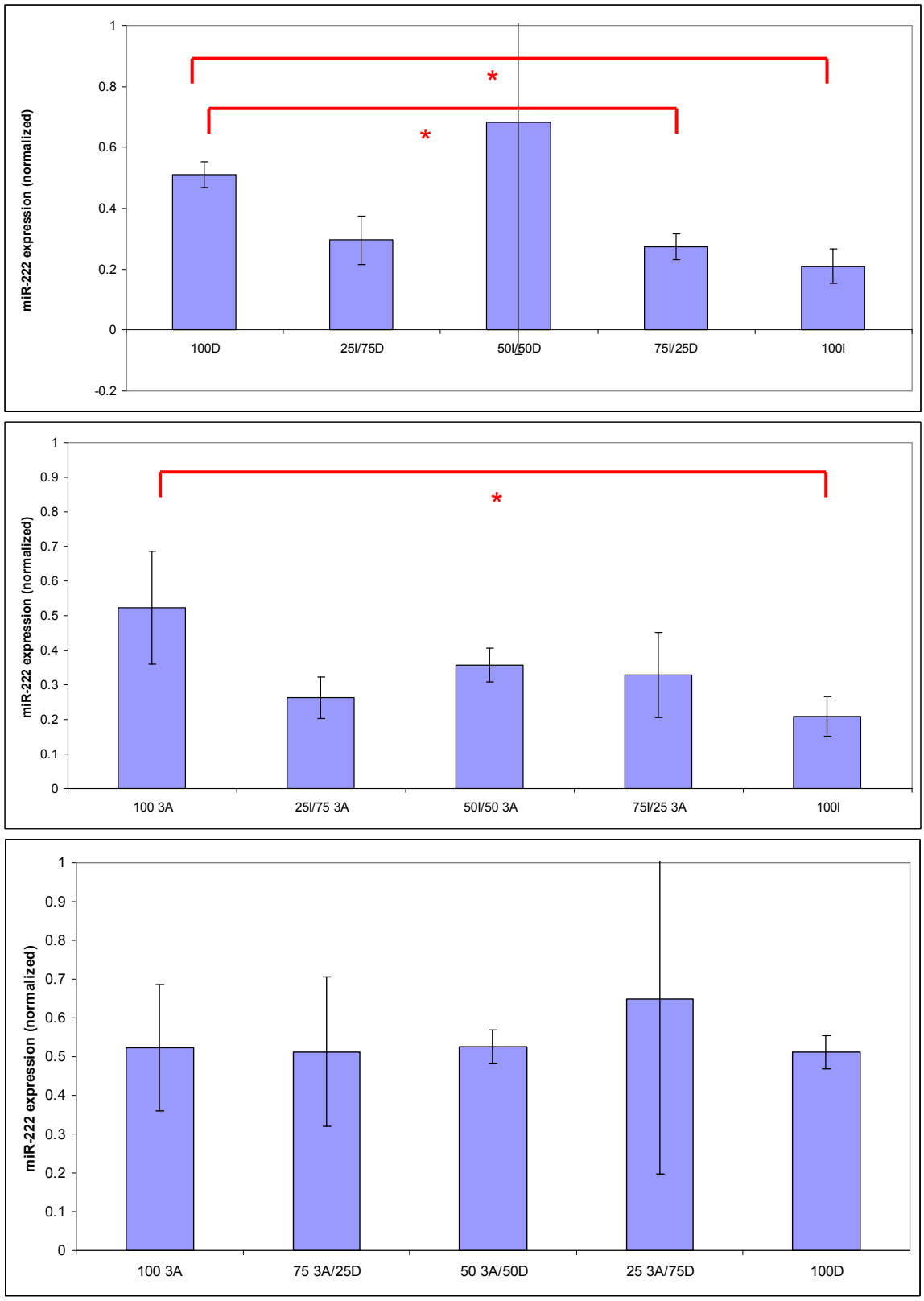

Figure 5.3: MiR-222 expression after antagomir transfection grouped by SPION type. * indicates $p < 0.05$.

TEM Imaging

Having verified the efficacy of the iron oxide nanoparticles on microRNA antagonism, we investigated the transfection process further by electron microscopy. We selected 100%D as a model particle and incubated them with PC-3 cells again. Cells were fixed 24 hours after nanoparticle exposure and imaged by TEM. Images show that the particles successfully entered cells and were consistently localized in endosomes. Figure 5.4A shows an electron micrograph of a portion of one cell. Several distinct dark regions containing electron-dense material can be seen. Figures 5.4B and C are enlarged images showing regions of Figure 5.4A. Large amounts of iron oxide nanoparticles can be clearly seen localized in late endosomal compartments, which can be identified by the slightly darker shade endued by counter-staining. The numbers of particles inside the endosomes varied considerably from endosome to endosome. Nevertheless, it appeared that endosomes containing nanoparticles had some tearing or rupturing, as indicated by arrows. Normal endosomes are typically uniformly gray in color; however we observed several which had lighter spots near the endosome perimeter (Figure 5.4B and D), which may indicate some leakage of its contents. Moreover, the perimeter of many of the endosomes seemed to be torn. This was especially apparent in the bottom endosome in Figure 5.4C and in those in 5.4D, taken from another cell from the same sample. While apparent tearing and rupturing was observed extensively for endosomes containing nanoparticles—presumably due to the proton sponge effect—nanoparticles were not clearly observed to leak outside endosomes into the cell cytosol, even at 24 hours post iron oxide exposure, which was the point at which the cells were fixed.

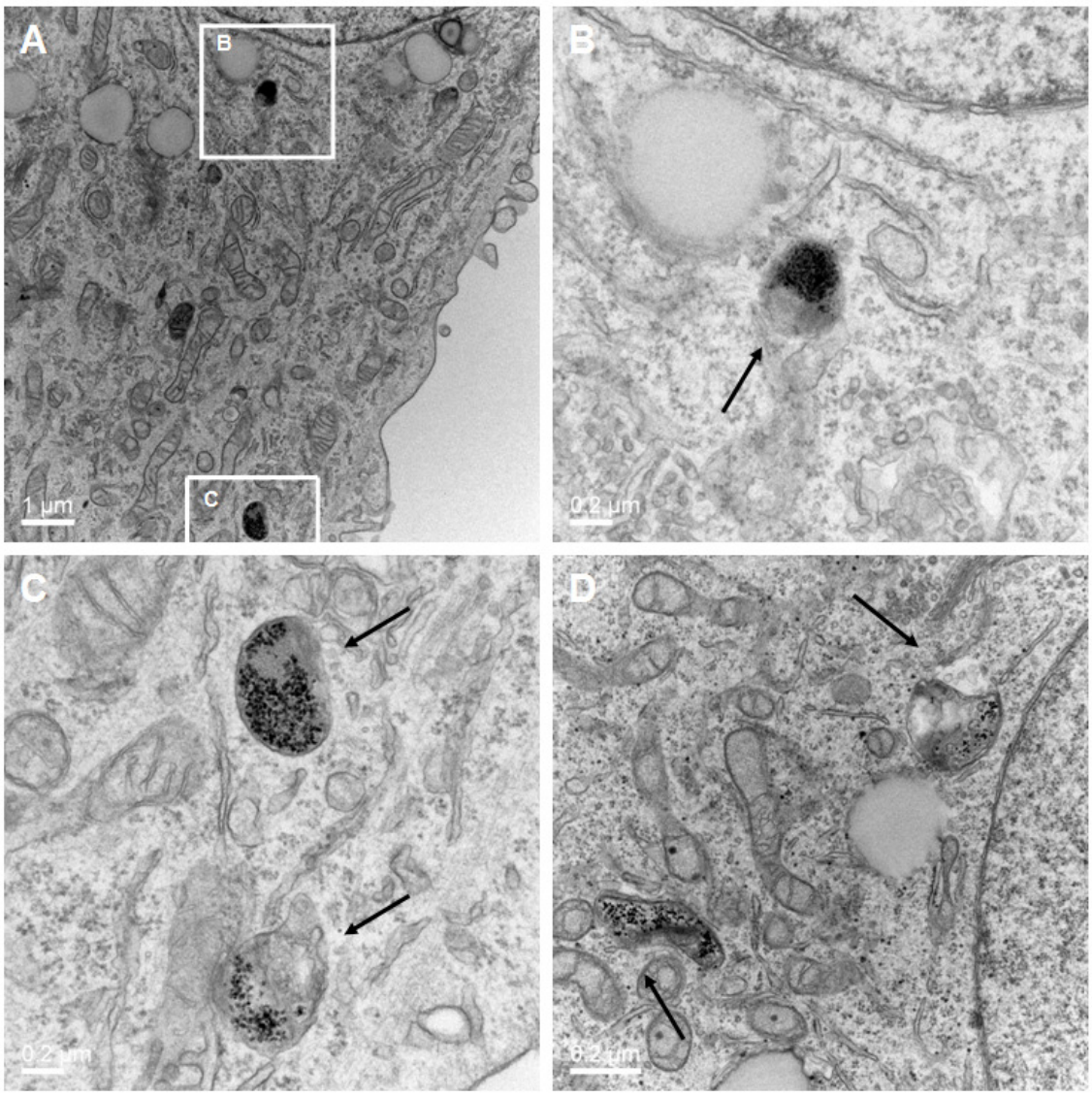

Figure 5.4: TEM images of PC-3 cells after transfection with 100%DPTA SPION. (B) and (C) are enlarged sections of (A). (D) represents another cell in the same sample. Arrows indicate sites of apparent endosomal breakage.

This observation was somewhat surprising because for the antagomirs to have an effect, they must escape from endosomes and enter the cytosol where they can bind to target microRNA. If the nanoparticles themselves did not leave endosomes, this would mean that the antagomirs had to dissociate from nanoparticles from within the endosome and migrate out themselves into the cytosol.

Fluorescence Imaging

We were able to determine the fate of the nanoparticles by TEM but the fate of the antagomirs was unclear. We thus used TYE665-conjugated antagomirs that were otherwise identical to those used in the transfection experiments and used them to follow antagomir fate through fluorescent imaging. TYE665 has similar spectra properties to Cy5 with a maximum absorbance at 557 nm and maximum emission at 563 nm. During delivery, fluorescently-labeled antagomirs (FLNA) will be electrostatically associated to 100%D iron oxide nanoparticles. Iron oxides, however, have a relatively broad and high absorption that includes the wavelength range of TYE665 emission (Figure 5.5). Because of the close association of the nanoparticles and antagomirs, it is possible that the iron oxides quench emission of the dye. This would prevent fluorescent imaging of the antagomir for as long as it is associated with the nanoparticle.

We thus incubated fluorescently-labeled antagomirs with 100%D iron oxide nanoparticles and assayed any change in emission intensity. Figure 5.6 shows the emission of antagomirs alone along with the emission of antagomirs incubated with 100%DPTA nanoparticles. Results show that emission is significantly decreased when the antagomirs are associated with the iron oxides. Indeed, integrated emission decreases by around 95% after nanoparticle association. We thus expect that when associated to a delivery vector, antagomirs will not be visible by fluorescent imaging. Fluorescent signals should thus correspond to antagomirs that have been unloaded from their nanoparticle delivery vectors.

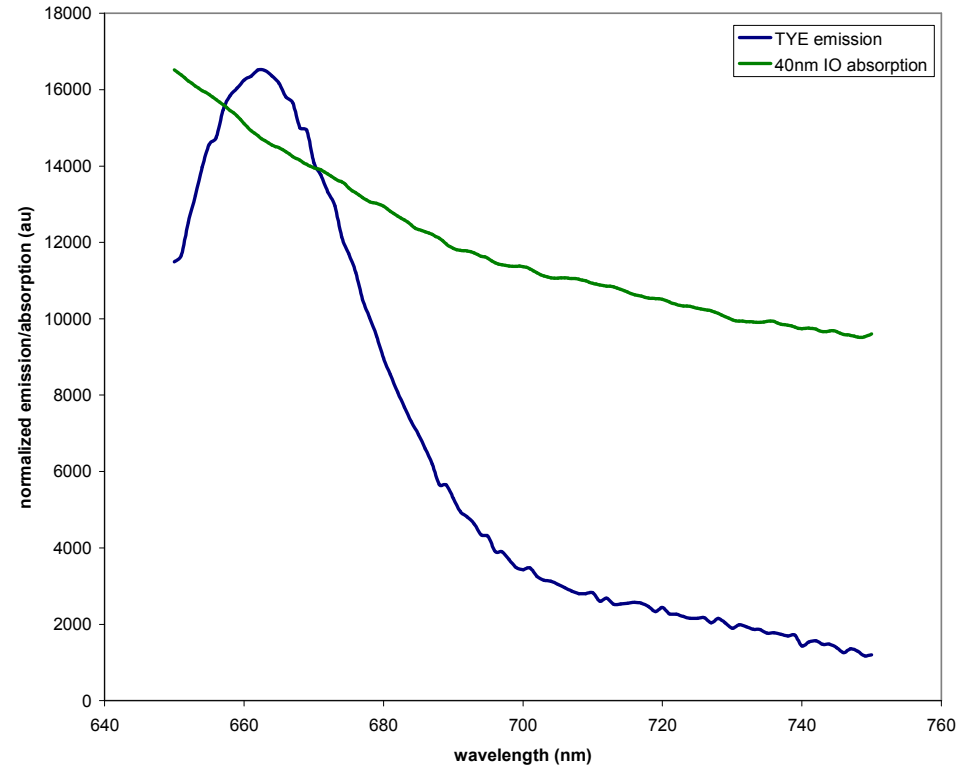

Figure 5.5: FLNA emission and 40nm SPION absorbance spectra.

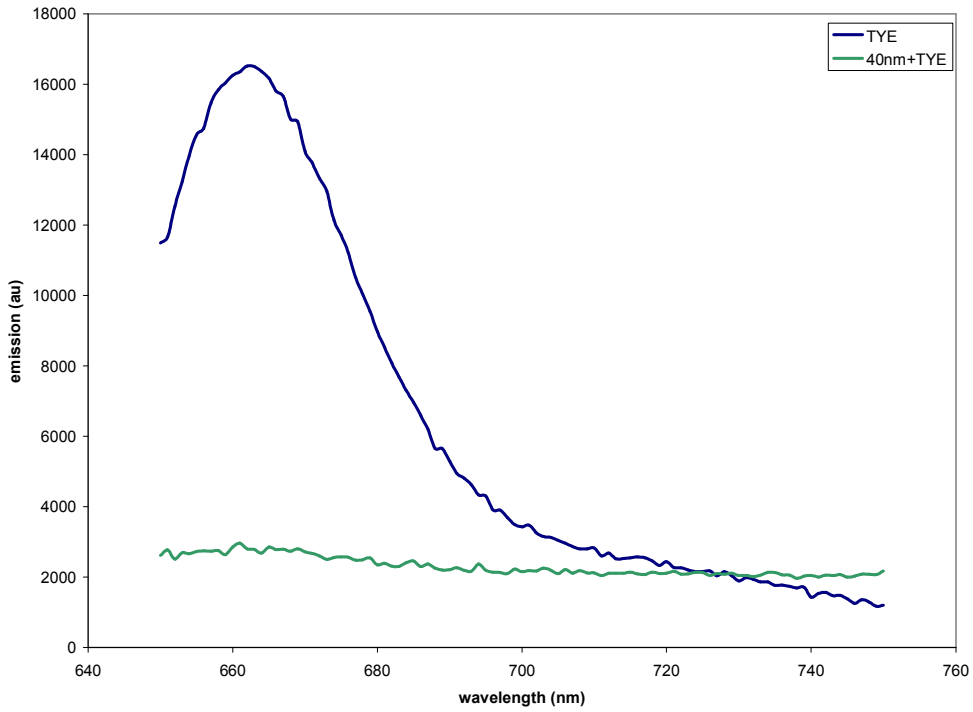

Figure 5.6: Emission of free FLNA and FLNA complexed with 100% DPTA SPION.

Fluorescently-labeled antagomirs were thus delivered in complex with 100%DPTA iron oxide nanoparticles. Cell samples were fixed at various points in time and imaged to see localization of the oligonucleotide probes. Figure 5.7A shows composite images of DAPI (blue) and TYE665 (red) filters at 5min, 2 hours, 4 hours, and 24 hours after introduction of the delivery complexes to PC-3 cells. Consistent with our result showing quenching of the fluorescent tag by the iron oxide carrier, shortly after delivery no signal was detected. If no quenching were to occur, we would have expected to observe TYE665 signal along the perimeter of the cell at the 5 min time point as the particle-probe complexes should bind electrostatically to the negatively charged plasma membrane, similar to the results observed in Appendix A. Indeed, no TYE665 signal was observed in the 5min, 2 hour, or 4 hour time points. At 24 hours, however, red signals could be detected inside the cells. Figure 5.7B shows an enlarged region of the 24 hour image from Figure 5.7A, overlaid with a LAMP1 lysosomal stain (green). Red signals—corresponding to the fluorescently tagged antagomir—are visible, indicating dissociation of the antagomir from the iron oxide nanoparticle. In addition, this signal does not colocalize with the green lysosomal stain, indicating that the oligonucleotides have escaped from the ruptured endosomes. In sum, this data suggests that antagomirs are able to dissociate from their nanoparticle carriers inside the cell and migrate out of ruptured endosomal compartments into the cell cytosol. This intracellular dissociation takes place at least 4 hours post transfection.

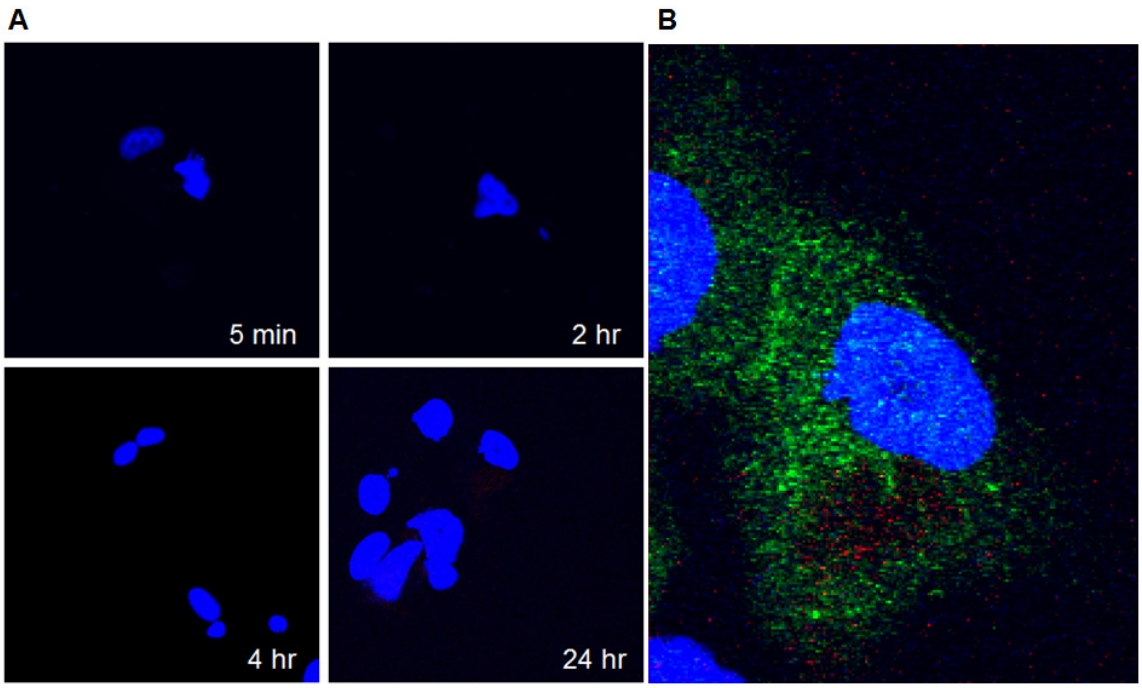

Figure 5.7: Confocal imaging of cells transfected with 100% DPTA SPION and FLNA. (A) Imaging of cells fixed at different time points showing only DAPII (blue) and FLNA (red) channels. (B) Zoom in of 24hr image with LAMP1 (green) overlay.

In conclusion, we have demonstrated the efficacy of amine-coated iron oxide nanoparticles for the intracellular delivery of antagomirs against miR-222. The particles are able to enter cells and become sequestered in endosomal compartments. They are able to rupture endosomes, presumably through the proton-sponge effect, but do not seem to leave the endosomes themselves. Instead, the antagomirs appear to dissociate from their nanoparticle carriers and escape alone into the cytosol where they may antagonize their microRNA targets. Overall we have observed target microRNA expression to decrease up to around 75%. Differences in miR-222 antagonism were observed for particles containing different amine coatings, with imidazole-containing particles performing superior to tertiary amine- or DPTA-containing particles. The exact reason for this observed performance difference is

yet unclear although it is probably owing to the chemical properties of imidazole, with its relatively lower pK_a and thus improved proton buffering ability and lower cationic charge at neutral pH. These properties may render imidazole an enhanced ability to rupture endosomes through the proton sponge effect or to release antagomirs into the cell relative to its higher pK_a counterparts.

5.4 References

1. Subramanian, S., et al., *MicroRNA expression signature of human sarcomas.* Oncogene, 2008. **27**(14): p. 2015-2026.

2. Doench, J.G. and P.A. Sharp, *Specificity of microRNA target selection in translational repression.* Genes & Development, 2004. **18**(5): p. 504-511.

3. *miRBase, Release 16*. March 1, 2011]; Available from: http://www.mirbase.org/index.shtml.

4. Miska, E.A., *How microRNAs control cell division, differentiation and death.* Current Opinion in Genetics & Development, 2005. **15**(5): p. 563-568.

5. Ambros, V. and H.R. Horvitz, *HETEROCHRONIC MUTANTS OF THE NEMATODE CAENORHABDITIS-ELEGANS.* Science, 1984. **226**(4673): p. 409-416.

6. Chalfie, M., H.R. Horvitz, and J.E. Sulston, *MUTATIONS THAT LEAD TO REITERATIONS IN THE CELL LINEAGES OF C-ELEGANS.* Cell, 1981. **24**(1): p. 59-69.

7. Brennecke, J., et al., *Principles of MicroRNA-target recognition.* Plos Biology, 2005. **3**(3): p. 404-418.

8. Xu, P.Z., et al., *The Drosophila MicroRNA mir-14 suppresses cell death and is required for normal fat metabolism.* Current Biology, 2003. **13**(9): p. 790-795.

9. He, L. and G.J. Hannon, *Micrornas: Small RNAs with a big role in gene regulation.* Nature Reviews Genetics, 2004. **5**(7): p. 522-531.

10. Calin, G.A. and C.M. Croce, *MicroRNA signatures in human cancers.* Nature Reviews Cancer, 2006. **6**(11): p. 857-866.

11. Bartel, D.P., *MicroRNAs: Genomics, biogenesis, mechanism, and function.* Cell, 2004. **116**(2): p. 281-297.

12. Harfe, B.D., *MicroRNAs in vertebrate development.* Current Opinion in Genetics & Development, 2005. **15**(4): p. 410-415.

13. Esquela-Kerscher, A. and F.J. Slack, *Oncomirs - microRNAs with a role in cancer.* Nature Reviews Cancer, 2006. **6**(4): p. 259-269.

14. He, L., et al., *A microRNA polycistron as a potential human oncogene.* Nature, 2005. **435**(7043): p. 828-833.

15. Calin, G.A., et al., *Frequent deletions and down-regulation of micro-RNA genes miR15 and miR16 at 13q14 in chronic lymphocytic leukemia.* Proceedings of the National Academy of Sciences of the United States of America, 2002. **99**(24): p. 15524-15529.

16. Calin, G.A., et al., *MicroRNA profiling reveals distinct signatures in B cell chronic lymphocytic leukemias.* Proceedings of the National Academy of Sciences of the United States of America, 2004. **101**(32): p. 11755-11760.

17. Lu, J., et al., *MicroRNA expression profiles classify human cancers.* Nature, 2005. **435**(7043): p. 834-838.

18. Wang, X., et al., *MicroRNA-122a functions as a novel tumor suppressor downstream of adenomatous polyposis coli in gastrointestinal cancers.* Biochemical and Biophysical Research Communications, 2009. **387**(2): p. 376-380.

19. Krutzfeldt, J., et al., *Silencing of microRNAs in vivo with 'antagomirs'.* Nature, 2005. **438**(7068): p. 685-689.

20. Elmen, J., et al., *LNA-mediated microRNA silencing in non-human primates.* Nature, 2008. **452**(7189): p. 896-U10.

21. Daige, C.L., et al., *MicroRNA mimics as cancer therapeutics.* Proceedings of the American Association for Cancer Research Annual Meeting, 2010. **51**: p. 983.

22. Wang, V. and W. Wu, *MicroRNA-Based Therapeutics for Cancer.* Biodrugs, 2009. **23**(1): p. 15-23.

23. Rasband, W.S., *ImageJ 1.42q*, NIH.

24. Galardi, S., et al., *miR-221 and miR-222 expression affects the proliferation potential of human prostate carcinoma cell lines by targeting p27(Kip1)*.* Journal of Biological Chemistry, 2007. **282**(32): p. 23716-23724.

25. Ciafre, S.A., et al., *Extensive modulation of a set of microRNAs in primary glioblastoma.* Biochemical and Biophysical Research Communications, 2005. **334**(4): p. 1351-1358.

26. le Sage, C., et al., *Regulation of the p27(Kip1) tumor suppressor by miR-221 and miR-222 promotes cancer cell proliferation.* Embo Journal, 2007. **26**(15): p. 3699-3708.

27. Lee, E.J., et al., *Expression profiling identifies microRNA signature in pancreatic cancer.* International Journal of Cancer, 2007. **120**(5): p. 1046-1054.

28. Volinia, S., et al., *A microRNA expression signature of human solid tumors defines cancer gene targets.* Proceedings of the National Academy of Sciences of the United States of America, 2006. **103**(7): p. 2257-2261.

29. Felicetti, F., et al., *The promyelocytic leukemia zinc finger-microRNA-221/-222 pathway controls melanoma progression through multiple oncogenic mechanisms.* Cancer Research, 2008. **68**(8): p. 2745-2754.

30. He, H.L., et al., *The role of microRNA genes in papillary thyroid carcinoma.* Proceedings of the National Academy of Sciences of the United States of America, 2005. **102**(52): p. 19075-19080.

31. Murakami, Y., et al., *Comprehensive analysis of microRNA expression patterns in hepatocellular carcinoma and non-tumorous tissues.* Oncogene, 2006. **25**(17): p. 2537-2545.

32. Koshkin, A.A., et al., *LNA (Locked Nucleic Acids): Synthesis of the adenine, cytosine, guanine, 5-methylcytosine, thymine and uracil bicyclonucleoside monomers, oligomerisation, and unprecedented nucleic acid recognition.* Tetrahedron, 1998. **54**(14): p. 3607-3630.

33. Singh, S.K., et al., *LNA (locked nucleic acids): synthesis and high-affinity nucleic acid recognition.* Chemical Communications, 1998(4): p. 455-456.

34. Wienholds, E., et al., *MicroRNA expression in zebrafish embryonic development.* Science, 2005. **309**(5732): p. 310-311.

35. Valoczi, A., et al., *Sensitive and specific detection of microRNAs by northern blot analysis using LNA-modified oligonucleotide probes.* Nucleic Acids Research, 2004. **32**(22).

36. Tolstrup, N., et al., *OligoDesign: optimal design of LNA (locked nucleic acid) oligonucleotide capture probes for gene expression profiling.* Nucleic Acids Research, 2003. **31**(13): p. 3758-3762.

37. Jepsen, J.S., M.D. Sorensen, and J. Wengel, *Locked nucleic acid: A potent nucleic acid analog in therapeutics and biotechnology.* Oligonucleotides, 2004. **14**(2): p. 130-146.

38. Yezhelyev, M.V., et al., *Proton-sponge coated quantum dots for siRNA delivery and intracellular imaging.* Journal of the American Chemical Society, 2008. **130**(28): p. 9006-9012.

CHAPTER 6

DETERMINING THE EFFECT OF IRON OXIDE NANOPARTICLE SIZE ON ANTAGOMIR DELIVERY

6.1 Introduction

Size is one of the key features of nanotechnology and gives rise to the unique properties of this class of material. It enables materials to interact specifically with biological molecules and structures and to have properties distinct from their bulk phase, such as fluorescence in semiconductor quantum dots or superparamagnetism in iron oxide nanoparticles [1-3]. Even within the nanometer range, however, size is an important factor that influences how materials behave, particularly in drug delivery applications. Size has been reported to influence almost every aspect of particle function including degradation, flow properties, clearance, biodistribution, level of uptake, and uptake mechanisms [4-12]. For instance, studies have shown that smaller nanoparticles (< 20 nm) can be excreted renally, medium sized nanoparticles (30-150 nm) have accumulated in the bone marrow, heart, kidney and stomach, while large particles (150-300 nm) accumulate in the liver and spleen by the reticuloendothelial system (RES) [9, 13-18]. This has led to a focus on the use of particles smaller than 100 nm for optimal drug delivery applications.

Past studies have also indicated size effects of nanoparticles at the cellular level, specifically with regards to intracellular uptake. Using Poly(lactic-co-glycolic acid)-copolymer nanoparticles to deliver pDNA, Amidon et al. reported seeing highest uptake for particles with a mean diameter of 100 nm [19]. Labhasetwar et al. showed using another cell line that cellular uptake for these same particles was

highest for particles with mean diameters of 70 nm as compared to those with mean diameters of 200 nm [20]. Yao et al. prepared PEI nanogel-pDNA complexes of 38, 75, 87, 121, 132, and 167 nm and found complexes of 75 nm and 87 nm exhibited the highest transfection efficiencies [21-23].

Studies investigating how size affects uptake have also been performed for inorganic nanoparticles. Chan et al. evaluated intracellular uptake of 14, 50, and 74 nm anionic gold nanoparticles and reported 50nm particles yielding the best intracellular uptake [24]. Xia et al., on the other hand, evaluated 15 and 45 nm gold nanospheres and 33 and 55nm gold nanocages and reported that the smaller particles had superior cellular uptake for both nanospheres and nanocages, regardless of nanoparticle coating [25]. The conflicting results of these two studies may be due to confounding factors such as nanoparticle coating, adsorption of serum proteins onto the nanoparticles, and cell type. Chan et al. used negatively charged citrate coated gold, which is not able to enter cells due to its charge and can only enter once coated with serum proteins. Xia et al., on the other hand, used a positively charged poly(allylamine hydrochloride) coating.

It is clear that further studies need to be conducted to evaluate how nanoparticle size affects internalization and, more specifically, nucleic acid transfection. In this chapter, we will prepare and use DPTA-coated iron oxide nanoparticles with hydrodynamic diameters of 40, 80, 150, and 200nm to evaluate how nanoparticle size affects antagomir delivery. We will begin by reacting the carboxyl-coated SPIONs with DPTA, monitoring the reaction progress, and characterizing the reacted particles, including their DNA binding properties. SPIONs will then be used to transfect PC-3 cells with antagomir against miR-222, a cancer-

associated miRNA. TEM and fluorescence imaging will also be used to study the transfection process further.

6.2 Methods

Materials

Water-soluble 50nm, 100nm, and 200nm iron oxide nanoparticles with a glucuronic acid matrix coating were purchased from Chemicell GmbH (Berlin, Germany). Particle sizes were found to differ slightly from the size reported by the manufacturer and varied depending on lot. Two different batches of 50nm particles were found to have sizes of approximately 40nm and 80nm. The 100nm particles had a hydrodynamic size of 150nm and the 200nm particles had a hydrodynamic size of 200nm. DPTA was purchased from Sigma-Aldrich (St. Louis, MO).

Particle Conjugation and Purification

Glucuronic acid-coated iron oxide nanoparticles were conjugated to DPTA amine molecules by carbodiimide reaction. Amines were added at an excess to each of 40, 80, 150, and 200 nm particles. Because addition of amines raised the pH, pH was adjusted back to 5.5 for each reaction mixture. EDC was then added and the reaction mixture was allowed to incubate at room temperature for 1 hour. The pH of the mixture was raised to >8 by addition of NaOH to quench any reactive O-acylisourea intermediates and incubated for 10 minutes. The zeta potential was then measured for each particle sample (Zetasizer Nano ZS90, Malvern Instruments, Worcestershire, UK). Sequential lowering the pH to 5.5, addition of EDC, raising the pH > 8, and zeta potential measurement was repeated until the zeta potential stabilized for all samples, indicating saturation of the nanoparticle surface with

amines. Particles were purified by either ultracentrifugation at 100,000 rpm (40nm particles) or by magnetism (80, 150, and 200nm particles). Magnetic purification was performed by applying samples on a permanent neodymium block magnet (K&J Magnetics, Inc, Jamison, PA). DLS measurements were also performed on the Zetasizer Nano instrument.

DNA Binding

For DNA binding studies, 6pmol of fluorescein-labeled DNA was incubated in 1X MOPS buffer (pH 7) with varying amounts of amine-conjugated SPION. The particles and DNA were allowed to complex overnight (12-18hours) at 4C. For aggregation/particle sizing experiments, the hydrodynamic sizes of the complexes were then determined by DLS. For DNA binding capacity experiments, the complexes were mixed with a 5X bromophenol blue loading buffer (400 ul solution prepared by mixing 200 ul 10X MOPS, 150 ul 1% bromophenol blue in water, and 50 ul 50% glycerol) and loaded onto a 0.8% agarose/0.1% Tween-20 gel in 1X MOPS. Gels were run for 15min at 120V in a and subsequently imaged with a UV transillumination system (BioRad, Hercules, CA).

DNA Transfection

PC-3 cells were grown in RPMI 1640 buffer and plated on a 96-well plate at about 5000 cells/well. Different sized IO nanoparticles were incubated overnight with LNA antagomirs against miR-222 at the following IO:LNA ratios, according to binding capacities determined in DNA binding experiments: 1:50 for 40 nm particles, 1:20 for 80 nm particles, 1:200 for 100 nm particles, and 1:5000 for 200 nm particles. Antagomirs had the sequence 5'- accCagTagCcaGatGtaGct-3' where capitalized bases are LNA-modified (Integrated DNA Technologies, Coralville, IA). Following

overnight incubation, complexes were diluted in Opti-MEM (Invitrogen) to appropriate concentrations for cell transfection.

After 24 hours of cell growth on the 96-well plate, cells were washed in PBS and delivery agents were added to yield a 40nM LNA concentration in Opti-MEM buffer (Invitrogen). Cells were incubated with delivery agents for 4hrs before washing in PBS. Twenty-four hours post-transfection, cells were lysed and RNA enriched for short sequences was collected using the miRvana RNA Isolation Kit (Ambion). All transfections were carried out in triplicate.

Real-Time PCR and Data Analysis

RNA samples were reverse transcribed using the Taqman® MicroRNA Reverse Transcription Kit (Applied Biosystems, Foster City, CA). Real-time PCR was the performed on the reverse transcription product using the TaqMan MicroRNA Assay according to the manufacturer's instructions (Applied Biosystems). Data was normalized by U6B small nuclear RNA as an endogenous control (RNU6B, from Applied Biosystems, Foster City, CA). After normalizing expression data to RNU6B, data was further normalized to no transfection control. Student t-test was performed to test for significance.

TEM Imaging

For TEM observation of conjugated nanoparticles, 5 uL of the samples were pipetted onto a carbon TEM grid. The solvents were slowly wicked away with filter paper after 15 minutes and the grids were then counterstained with a 1% phophotungstic acid solution (pH adjusted to 6) for 30 seconds. The staining solution was slowly wicked away and allowed to dry. Grids were then imaged by TEM (H-600, Hitachi, Japan) operating at an acceleration voltage of 80 kV.

For TEM examination of the monolayer cells, cells cultured in 6-well tissue culture plates were incubated with antagomir-nanoparticle complexes for four hour before being replaced with full media. Cells were fixed 24 hours post-transfection by incubating overnight in 2.5% glutaraldehyde in 0.1 M cacodylate buffer (pH 7.2) at 4C. Cells were then washed with the same buffer and post-fixed in 1% buffered osmium tetroxide, dehydrated through a graded ethanol series to 100%, and embedded in Eponate 12 resin (Ted Pella Inc., Redding, CA). Ultrathin sections were cut on a Leica UC6rt Ultramicrotome (Leica Microsystems, Bannockburn, IL) at 70-80nm, and counter-stained with 4% aqueous uranyl acetate and 2% lead citrate. Sections were examined using a Hitachi H-7500 transmission electron microscope (Hitachi High Technologies of America, Inc., Pleasanton, CA) equipped with a Gatan BioScan CCD camera.

Bulk Fluorescence Measurements

Bulk absorbance measurements were performed using a spectrophotometer (Shimadzu UV-2401PC, Kyoto, Japan). Bulk emission measurements were performed using a standard fluorometer (FluoMax, Jobin Yvon, Edison, NJ). Fluorescence quenching of TYE665-labeled antagomir by SPIONs was performed by comparing emissions of a volume of fluorescent antagomir-SPION complex and a volume of free fluorescent antagomir with equal concentration.

Fluorescence Imaging

For fluorescence imaging studies, nanoparticle-LNA complexes were prepared and transfection performed as per the Transfection method described above, except using a TYE665-conjugated LNA oligonucleotide in place of the regular LNA and growing cells in LabTek II chamber slides rather than a 96-well

plate. Cells were washed in 1X PBS 4 hours after nanoparticle-LNA complex exposure and then incubated with full medium. Twenty-four hours post-transfection, cells were washed twice briefly in PBS and fixed and permeabilized for 20 min in 4% paraformaldehyde supplemented with 0.1% Triton X-100. After briefly washing twice in PBS, blocking buffer (5% goat serum/2% BSA in 1X PBS) was added for 1 hour. Cells were washed again twice for 5 min each in 0.2% BSA/1X PBS before adding primary antibody against LAMP1 (Abgent, San Diego, CA) at a 6.25 ug/ml concentration diluted in 1% BSA/1X PBS for 45 minutes. Cells were washed 2X5 min again in 0.2% BSA/1X PBS and then incubated in Alexa Fluor 568-conjugated goat anti-rabbit secondary antibody (Invitrogen, Carlsbad, CA) at a 5ug/ml concentration in 2% BSA/1X PBS. Cells were then washed 2X5min in PBS before DAPI counterstaining. Slides were then mounted and coverslipped for imaging on a Zeiss LSM 510 META confocal microscope. Images were analyzed using NIH Image J software [26].

6.3 Results and Discussion

To investigate how nanoparticle size affects the transfection process, a panel of 4 nanoparticle sizes were evaluated: 40nm, 80nm, 150nm, and 200nm in hydrodynamic diameter (Figure 6.1). Particles were composed of inorganic magnetite cores coated with a glucuronic acid polymer coating, with the exception of the 200nm particles, which had cores composed of maghemite. TEM images showed that the 40nm and 80nm particles had cores which were approximately 10 nm in diameter, indicating they had a relatively thick polymer coating. Zeta potential measurements showed a highly negative particle surface charge for all samples, in agreement with the carboxyl groups on the glucuronic acid polymer coating. Zeta

was less negative for the smaller particles (-20.2mV and -28.0mV for 40nm and 80nm, respectively) and increased with particles size (-32.9mV and -36.2mV for 150nm and 200nm, respectively).

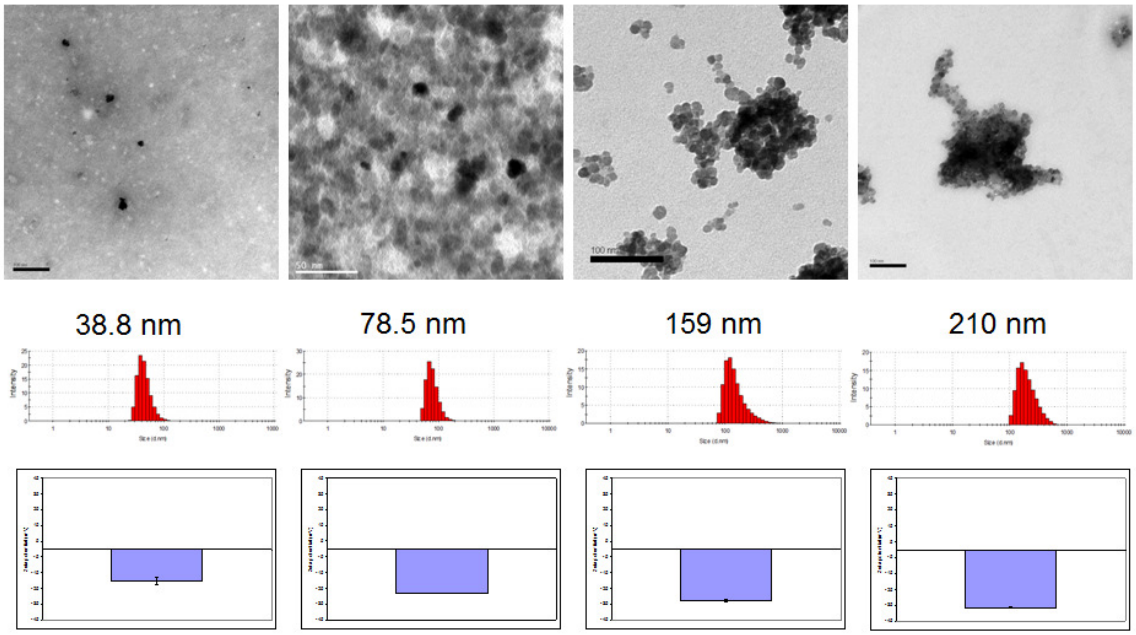

Figure 6.1: TEM, DLS, and zeta potential measurements for 40, 80, 150, and 200 nm SPIONs.

To functionalize particles with transfection ability, they were reacted with DPTA, an amine molecule that we have previously demonstrated to be useful for oligonucleotide transfection. Figure 6.2 shows the reaction procedure. Carboxyl-coated nanoparticles were reacted with DPTA through carbodiimide chemistry. The reaction should yield particles containing amide linkages to both a secondary and tertiary amine. Because EDC chemistry is difficult to control and does not give a 100% yield, we peformed the reaction iteratively until almost all the carboxyl groups

had been reacted. This was important to ensure that different levels of amine coating was not a variable in our analysis.

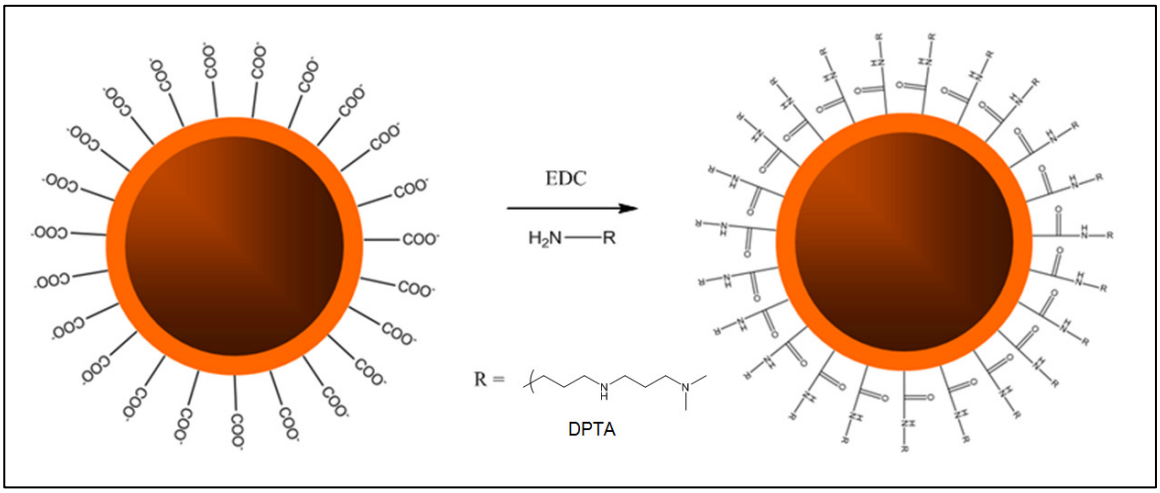

Figure 6.2: Reaction scheme for modifying carboxyl-coated SPIONS with DPTA amine molecules. Reaction was the same for all SPION sizes.

Because the reaction involved the polymer coating converting from carboxyl groups to amine groups—and hence from a negative charge to a positive charge—reaction progress could be monitored by zeta potential. The reaction was performed iteratively until the zeta plateaued, indicating saturation of the nanoparticle surface with DPTA (Figure 6.3). Particles all seemed to saturate at a zeta potential that was about the same in magnitude but opposite in sign from their original zetas. For instance 40nm particles had a charge of -20.2 pre-reaction and saturated at a zeta of around +20mV. Particle sizes were also assayed by dynamic light scattering (DLS). Results showed that particle sizes did not change significantly with reaction, indicating particle stability (Figure 6.4). Sizes did seem to decrease slightly after reaction, possibly due to unreacted carboxyl groups buried in the polymer layer interacting electrostatically with the amines on the surface.

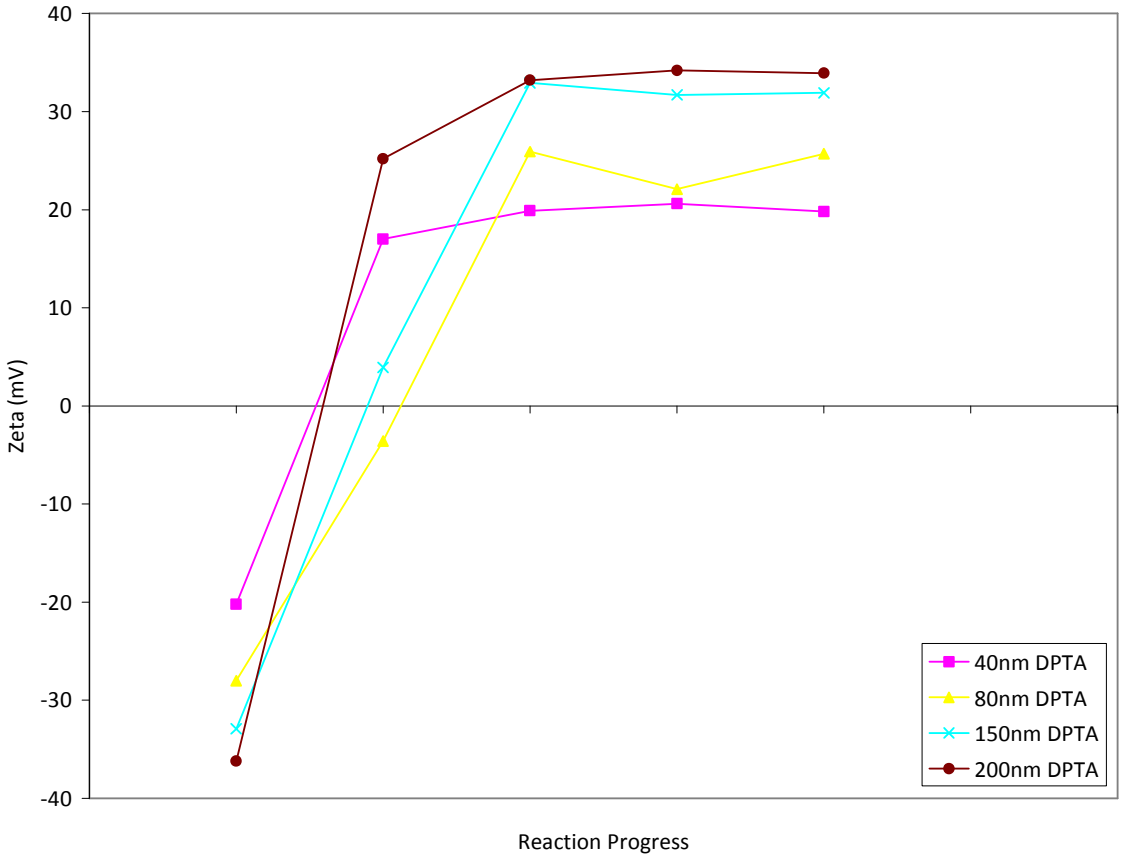

Figure 6.3: Zeta potential measurements to evaluate extent of amine reaction onto SPIONs. Zeta saturation was taken to indicate saturation of particle surface with amines.

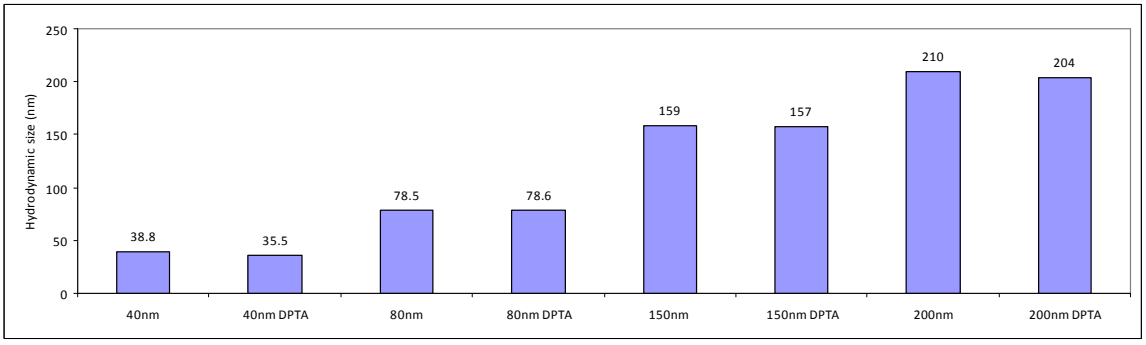

Figure 6.4: Hydrodynamic size of SPIONs before and after amine conjugation.

DNA-Nanoparticle Binding

With the particle size panel prepared and reacted with DPTA, we next investigated their DNA binding characteristics. One advantage of using cationic amines as a nanoparticle coating is the ability to electrostatically bind to DNA, which is anionic due to its phosphate groups. The number of DNA molecules each nanoparticle can bind is important to determine the appropriate DNA-SPION ratio to use for oligonucleotide transfection. To do this, nanoparticles were incubated with a fluorescein-labeled 21-mer single stranded DNA at different ratios. This DNA was identical to the oligonucleotide to be used for transfection except it contained no LNA-modified nucleotides. After incubation, the mixtures of SPION-fluorescently-labeled DNA (FDNA) were loaded onto an agarose gel and electrophoresis was performed. Results for the four nanoparticle sizes are shown in Figure 6.5.

The first lane in all gels contained only fluorescein-labeled DNA. As expected, the DNA migrated down the gel towards the cathode due to its negatively charged phosphate groups. The remaining bands contained identical amounts of DNA but had increasing amounts of nanoparticles to match the labeled ratios. For the 40 nm particles, the DNA band is quite strong at a 500:1 DNA:IO ratio, indicating that most of the DNA remained unbound. As the amount of IO is increased, the DNA band begins to fade until at a 50:1 ratio, all of the DNA appears to be bound. 80 nm particles bound 50 DNA/particle, 150 nm particles bound 200 DNA/particle, and 200 nm particles bound 5000 DNA/particle. Interestingly, the 40 nm and 80 nm particles bound similar amounts of DNA. It is unclear why this was the case but may be due to the two samples having similar core sizes. The DNA-SPION ratios determined by this experiment will be used for antagomir transfection.

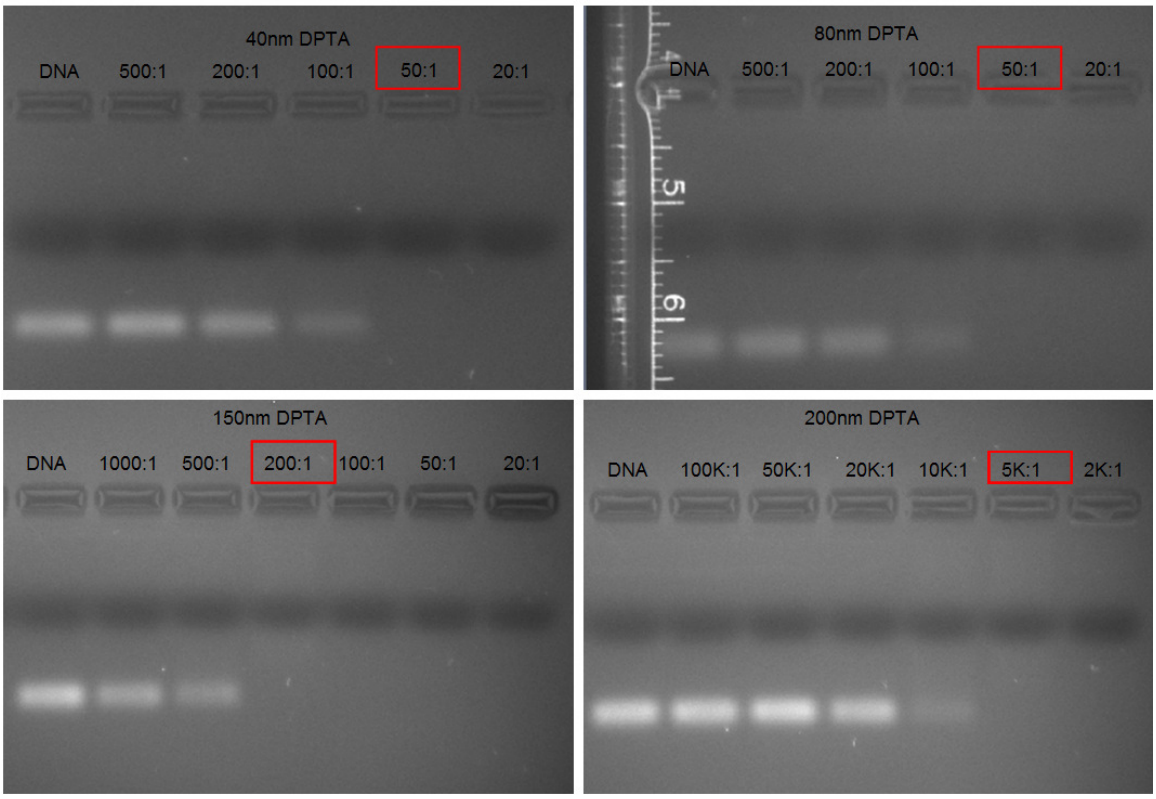

Figure 6.5: Gel electrophoresis assays showing oligonucleotide loading onto amine-coated SPIONs. Ratios indicate DNA:SPION ratios. Ratios boxed in red indicate lowest ratio at which all DNA appeared bound.

Transfection

With the DNA binding capacity determined for each particle size, we used the nanoparticles for transfecting PC-3 cells with an antagomir against miR-222, an oncogenic microRNA. Particle-antagomir complexes were incubated with cells at a 40 nM antagomir concentration and SPION concentrations to achieve the appropriate DNA-SPION ratios as determined by the DNA binding experiments. Transfection was assayed by real-time PCR 24 hours post-transfection; the results are shown in Figure 6.6. 40 nm particles had the highest antagonism, with miR-222 expression 51% of the no transfection control (NTC). 80nm particles had the next best gene antagonism, with miR-222 expression 72% of the control. Transfection

using 150 nm and 200 nm particles did not seem to have a statistically significant effect on miR-222 expression. The expression differences between the 40 nm and 80 nm particles was statistically significant.

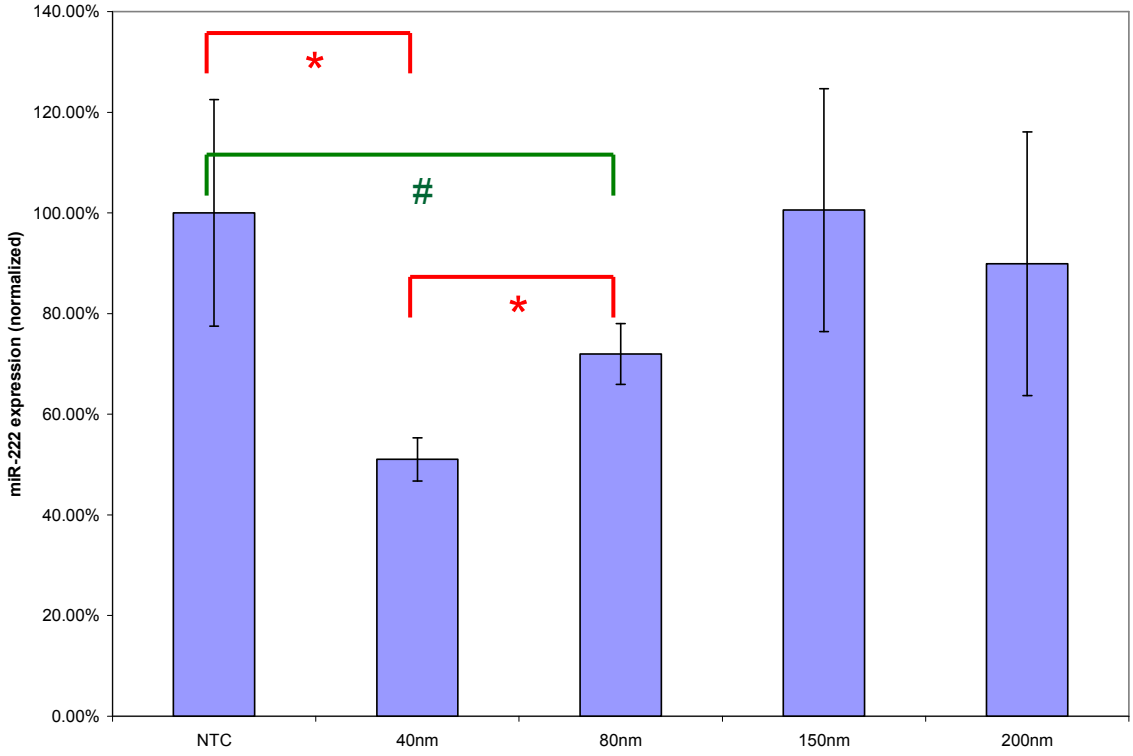

Figure 6.6: Real-time PCR data showing mir-222 expression for cells after antagomir transfection with different size SPIONs. Data shows comparative c_T values, with RNU6B as endogenous control, normalized to NTC. NTC = no transfection control. * : $p < 0.05$; # : $p = 0.0527$ by one-tailed t-test.

TEM Imaging

To further explore how the SPIONs enable transfection, particle-DNA complexes were again incubated with PC-3 cells. Twenty-four hours post-transfection, cells were fixed and imaged by TEM (Figure 6.7). The data shows that all particles tested entered into cells and localized inside endosomes. Relatively large numbers of particles seemed to be internalized for both the 40 nm and 80 nm sizes, with some endosomes containing several dozen particles. While the 150 nm and 200 nm particles were also internalized, relatively fewer were inside each endosome, with many containing fewer than 10. This is in agreement with past studies showing that particles larger than 100 nm exhibit decreased cellular internalization. Indeed, Figure 6.7 shows that several 200 nm particles were not internalized and remained bound to the cell membrane. This was not observed for the 40 nm and 80 nm particles.

Particles also appeared to cause rupture of endosomes, possibly through the proton sponge effect. This occurs when proton buffering groups, such as amines, are internalized by cells into intracellular compartments such as endosomes or lysosomes. The pH normally decreases in these compartments but amine groups such as those on our SPIONs can be protonated to buffer the acidic environment. This causes cells to pump additional H^+ to acidify the endosomal compartment. This, however, is accompanied by endosomal Cl- accumulation, which causes osmotic swelling and/or lysis of the endosome or lysosome [27-29]. Rupture of endosomal compartments containing nanoparticles is apparent in Figure 6.7, particularly for the 40 nm and 80 nm particles. Late endosomes are typically uniformly dark-colored by TEM using the staining procedures used for this experiment. The endosomes containing 40 nm and 80 nm particles, however, have some light-colored areas on

the interior of the endosomes and endosomal membranes appear to have some breakage. Light-colored regions are particularly apparent in images for the 80nm SPIONs and suggest areas where the endosomal contents were leaked into the cytosol. Interestingly, it was not clear whether any nanoparticles themselves entered the cytosol. This would suggest that antagomirs may detach from SPIONs inside lysosomes and migrate themselves into the cytosol where they may antagonize miR-222. TEM images also showed some endosomal rupture for the 150 nm and 200 nm SPIONs although some endosomes also appeared intact (e.g. zoomed-in TEM image of 150 nm particles). Overall, the TEM studies show that amine-coated SPIONs, particularly with 40 nm and 80 nm diameters, enter cells and disrupt endosomes, supporting the transfection results. Endosomal disruption is less clear for the larger particles but fewer particles seem to be internalized.

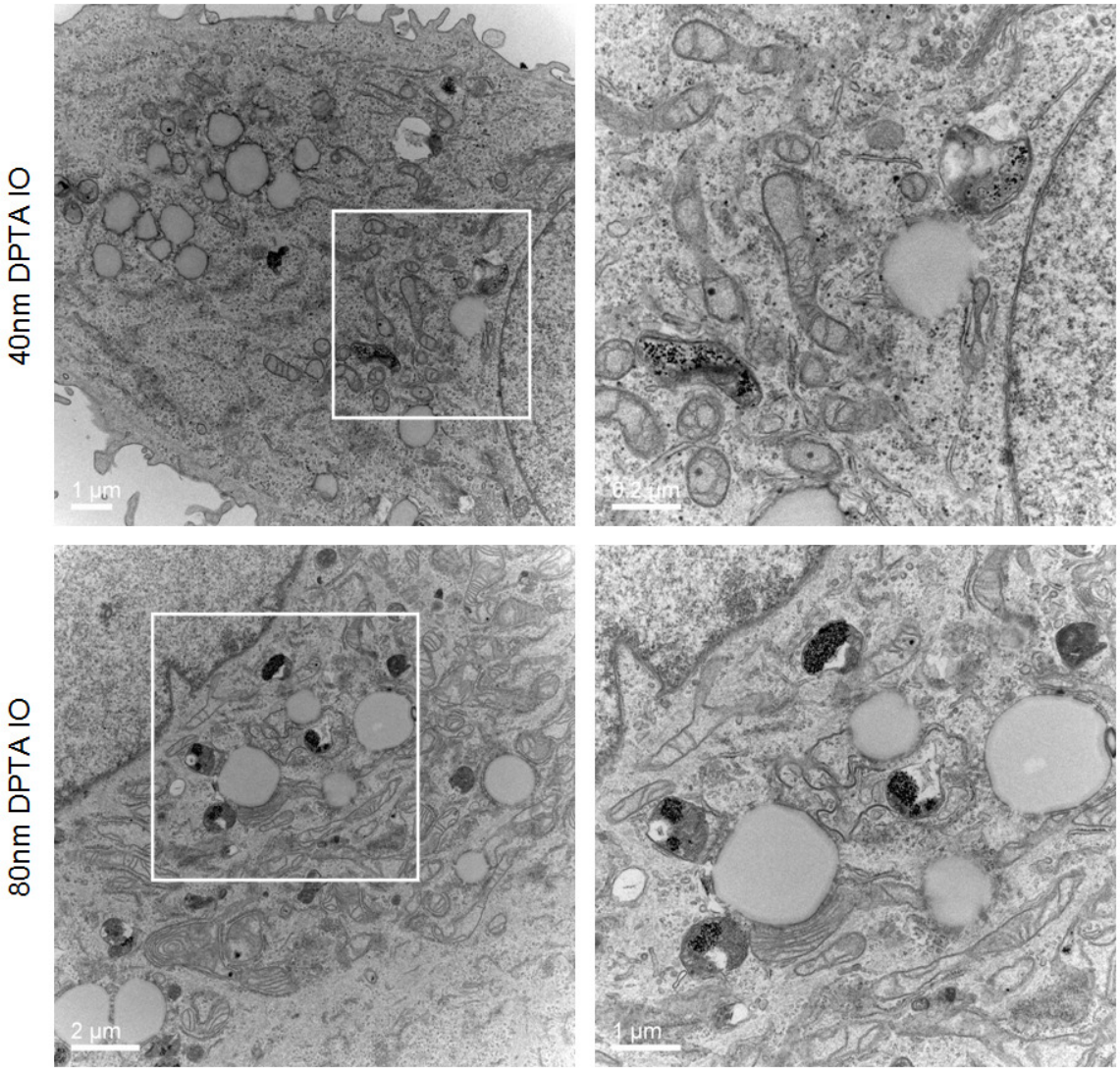

Figure 6.7: TEM images of PC-3 cells after SPION delivery of antagomir. Images on right are enlarged sections of images on the left, as indicated by the box.

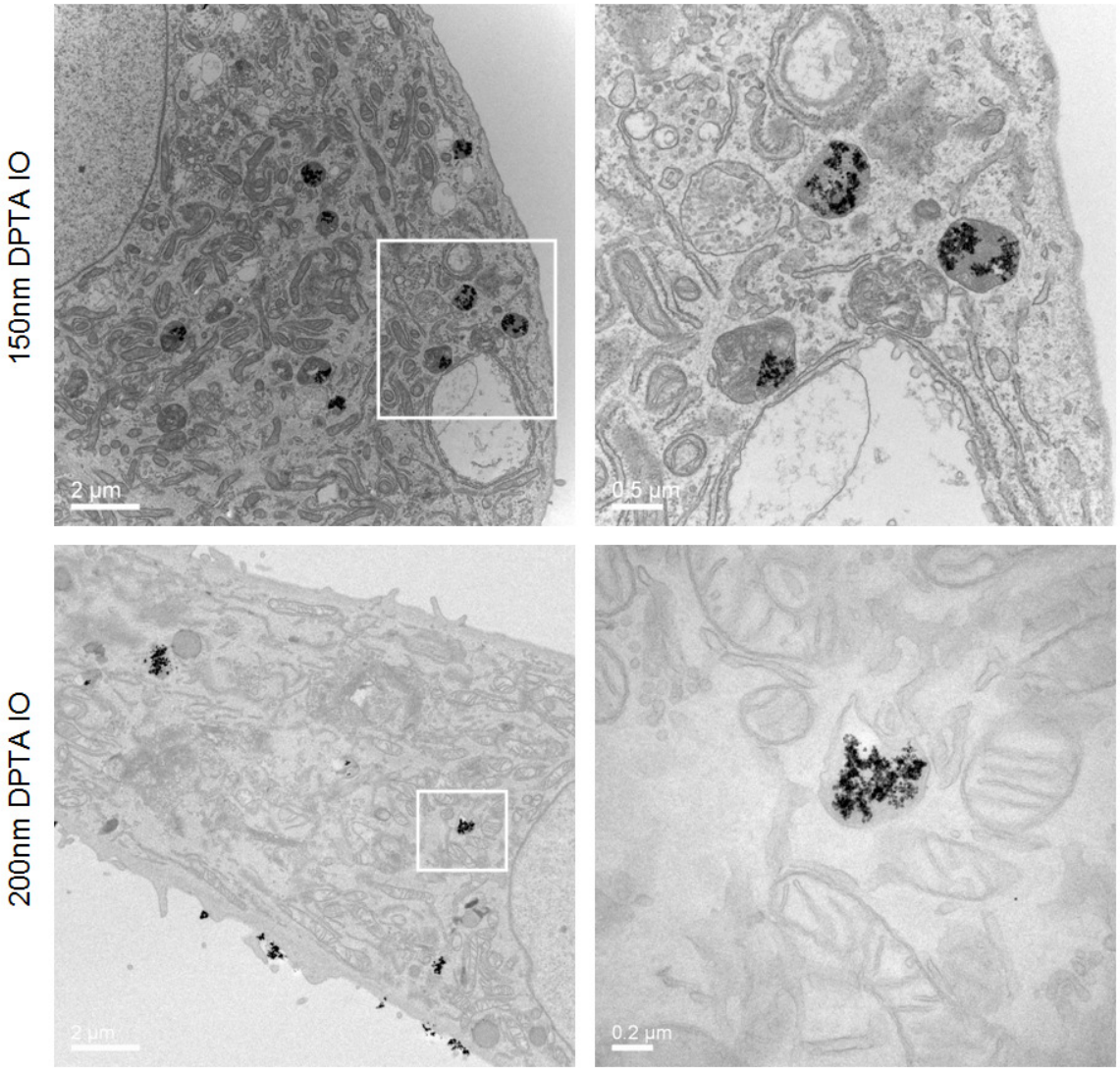

Figure 6.7 (continued)

Fluorescence Imaging

While TEM images allowed us to track the SPIONs, we also wanted to track the fate of antagomirs inside the cell. We thus used TYE665-labeled LNA antagomirs and delivered them with our panel of SPIONs of different sizes into PC-3 cells.

First, however, we investigated the spectral properties of our labeled antagomirs, nanoparticles, as well as their complex. TYE665 has similar spectral properties as Cy5, with a maximum absorption at 557nm and a maximum emission at 563nm. SPIONs, however, have a relatively broad and high absorption across the visible spectrum (Figure 6.8). It was thus possible that upon electrostatic association of the particles with TYE665-labeled antagomir that the SPIONs would quench TYE fluorescence. To test whether fluorescence quenching occurs upon complex formation, we incubated TYE665-labeled antagomirs with SPIONs at molar ratios matching those used for cellular transfection. Emission spectra was measured for either fluorescently labeled antagomir (FLNA) alone or for fluorescently-labeled antagomirs incubated with SPIONs. Figure 6.9 shows that for all sizes tested, fluorescence quenching was observed. Integrated TYE665 intensities showed that 40 nm, 80 nm, and 150 nm particles all decreased fluorescence by about 95%. 200 nm particles lowered fluorescence by a smaller amount, about 80%, possibly due to the relatively high antagomir:SPION ratio of 5000:1.

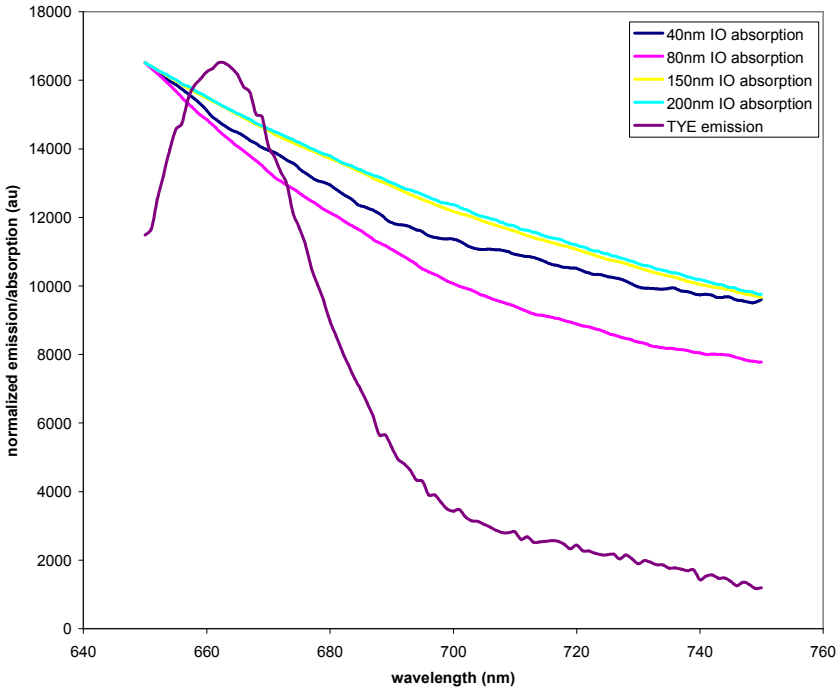

Figure 6.8: Emission and absorbance spectra of FLNA and SPIONS, respectively.

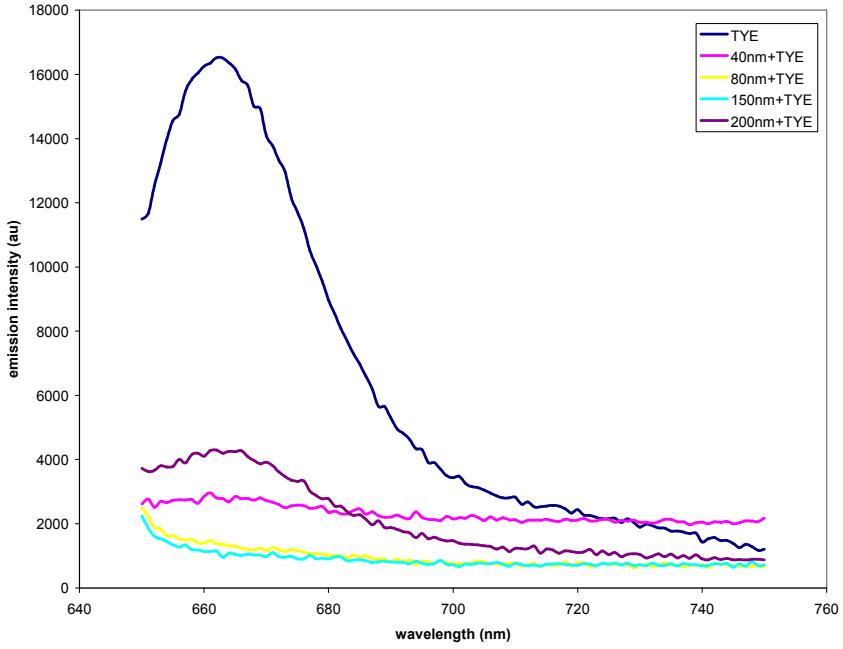

Figure 6.9: Emission of free FLNA and FLNA complexed with 100% DPTA SPION of different sizes.

The observance of fluorescence quenching upon FLNA-SPION complex formation suggests that TYE665 signal will not be observed as long as the antagomirs remain associated with their nanoparticle carriers. Signal should only be observed once antagomirs are unloaded. We thus prepared TYE665-antagomir-SPION complexes and used them to transfect PC-3 cells again. Cells were fixed both 4 hours and 24 hours post transfection and imaged. Figure 6.10 shows composite images containing both the DAPI and TYE665 channels. At 4 hours, no TYE665 signal was observed for any of the nanoparticle sizes. At 24 hours, however, a faint signal was observed for both the 40nm and 80nm particle sizes. This is in agreement with transfection data indicating that both 40nm and 80nm particles were able to effectively deliver antagomirs into cells to decrease miR-222 expression. The 150 nm and 200 nm particles were not able to result in miR-222 antagonism. Similarly, free antagomirs were not detected inside cells by fluorescence imaging. Overall, the data agrees with transfection data indicating that 40 nm and 80 nm particles are able to transfect antagomirs into cells and suggests that antagomirs detach from particles at least 4 hours post-transfection.

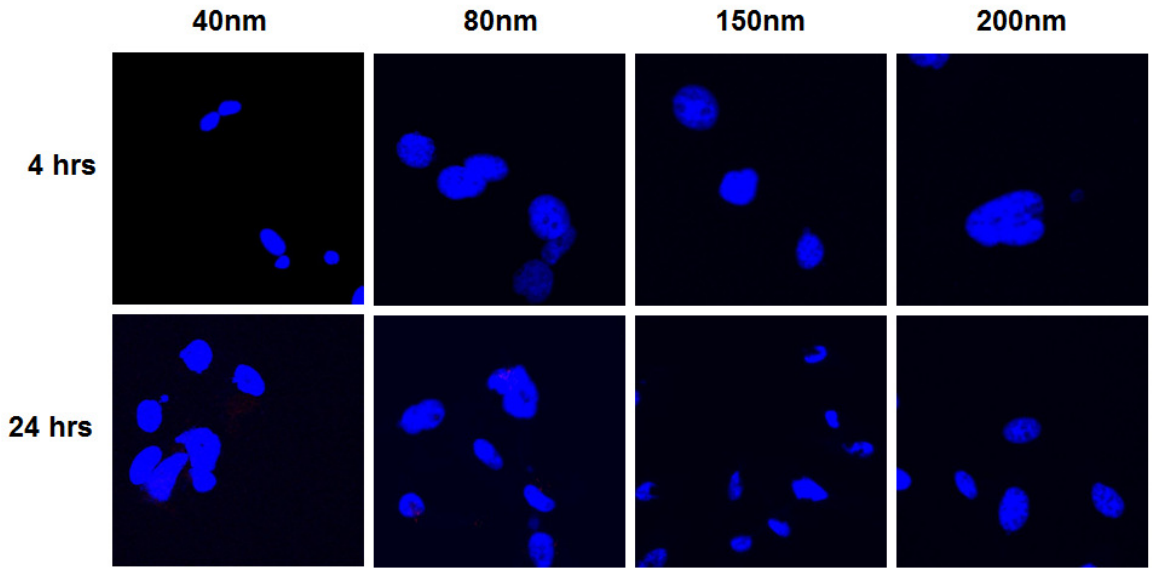

Figure 6.10: Fluorescence imaging showing DAPI (blue) and FLNA (red) channels for PC-3 cells transfected with FLNA-SPION complexes. Note that faint red signal can be observed in the 40 nm and 80 nm images at 24 hours.

In conclusion, we have investigated the effect of nanoparticle size on antagomir transfection into cells. Our results indicate that smaller particles may achieve greater miR-222 antagonism: both 40 nm and 80 nm SPIONs were able to achieve a statistically significant decrease in miR-222 expression with 40 nm particles performing better than 80 nm particles. Larger particles such as our 150 nm and 200 nm particles were not able to achieve a detectable knockdown in miR-222 at all. The underlying explanation for this observed difference is yet unknown but may have to do with differences in ability to be internalized by cells, to rupture intracellular lysosomal compartments, and perhaps to even leave these compartments themselves. For instance, our data suggests that larger particles such as the 200 nm SPIONs may not be able to enter cells as efficienty as smaller particles such as the 40 nm and 80 nm SPION. Several 200 nm SPIONs were detected to remain bound to the cell membrane by TEM as long as 24 hours post-

transfection. This was not observed for the smaller particles with the exception of some small-particle aggregates. Fluorescence data for TYE665-tagged antagomirs confirmed transfection data, with only 40 nm and 80 nm particles exhibiting signal indicating that antagomirs had detached from their nanoparticle carriers. While debate still exists on optimal nanoparticle sizes for cellular internalization, our study examines overall gene antagonism, for which factors such cellular internalization as well as breaching intracellular barriers and releasing drug cargo are all involved. For this purpose, our study suggests that smaller particles are superior.

Of course, the smallest size investigated in this chapter was 40 nm. It may therefore be worthwhile to study the efficiencies of particles even smaller than this to see if maximum gene knockdown occurs at a specific nanoparticle size or if gene knockdown always improves with decreasing size.

6.4 References

1. Smith, A.M. and S.M. Nie, *Chemical analysis and cellular imaging with quantum dots.* Analyst, 2004. **129**(8): p. 672-677.

2. Mailander, V. and K. Landfester, *Interaction of Nanoparticles with Cells.* Biomacromolecules, 2009. **10**(9): p. 2379-2400.

3. Smith, A.M., X.H. Gao, and S.M. Nie, *Quantum dot nanocrystals for in vivo molecular and cellular imaging.* Photochemistry and Photobiology, 2004. **80**(3): p. 377-385.

4. Panyam, J., et al., *Polymer degradation and in vitro release of a model protein from poly(D,L-lactide-co-glycolide) nano- and microparticles.* Journal of Controlled Release, 2003. **92**(1-2): p. 173-187.

5. Dunne, M., O.I. Corrigan, and Z. Ramtoola, *Influence of particle size and dissolution conditions on the degradation properties of polylactide-co-glycolide particles.* Biomaterials, 2000. **21**(16): p. 1659-1668.

6. Goldsmith, H.L. and V.T. Turitto, *RHEOLOGICAL ASPECTS OF THROMBOSIS AND HEMOSTASIS - BASIC PRINCIPLES AND APPLICATIONS - ICTH-REPORT - SUBCOMMITTEE ON RHEOLOGY OF THE INTERNATIONAL COMMITTEE ON THROMBOSIS AND HEMOSTASIS.* Thrombosis and Haemostasis, 1986. **55**(3): p. 415-435.

7. Patil, V.R.S., et al., *Particle diameter influences adhesion under flow.* Biophysical Journal, 2001. **80**(4): p. 1733-1743.

8. Lamprecht, A., U. Schafer, and C.M. Lehr, *Size-dependent bioadhesion of micro- and nanoparticulate carriers to the inflamed colonic mucosa.* Pharmaceutical Research, 2001. **18**(6): p. 788-793.

9. Moghimi, S.M., A.C. Hunter, and J.C. Murray, *Long-circulating and target-specific nanoparticles: Theory to practice.* Pharmacological Reviews, 2001. **53**(2): p. 283-318.

10. Illum, L., et al., *BLOOD CLEARANCE AND ORGAN DEPOSITION OF INTRAVENOUSLY ADMINISTERED COLLOIDAL PARTICLES - THE EFFECTS OF PARTICLE-SIZE, NATURE AND SHAPE.* International Journal of Pharmaceutics, 1982. **12**(2-3): p. 135-146.

11. Champion, J.A., Y.K. Katare, and S. Mitragotri, *Particle shape: A new design parameter for micro- and nanoscale drug delivery carriers.* Journal of Controlled Release, 2007. **121**(1-2): p. 3-9.

12. Sonavane, G., K. Tomoda, and K. Makino, *Biodistribution of colloidal gold nanoparticles after intravenous administration: Effect of particle size.* Colloids and Surfaces B-Biointerfaces, 2008. **66**(2): p. 274-280.

13. Veiseh, O., J.W. Gunn, and M.Q. Zhang, *Design and fabrication of magnetic nanoparticles for targeted drug delivery and imaging.* Advanced Drug Delivery Reviews, 2010. **62**(3): p. 284-304.

14. Choi, H.S., et al., *Renal clearance of quantum dots.* Nature Biotechnology, 2007. **25**(10): p. 1165-1170.

15. Banerjee, T., et al., *Preparation, characterization and biodistribution of ultrafine chitosan nanoparticles.* International Journal of Pharmaceutics, 2002. **243**(1-2): p. 93-105.

16. Moghimi, S.M., *EXPLOITING BONE-MARROW MICROVASCULAR STRUCTURE FOR DRUG-DELIVERY AND FUTURE THERAPIES.* Advanced Drug Delivery Reviews, 1995. **17**(1): p. 61-73.

17. Moghimi, S.M., *MECHANISMS OF SPLENIC CLEARANCE OF BLOOD-CELLS AND PARTICLES - TOWARDS DEVELOPMENT OF NEW SPLENOTROPIC AGENTS.* Advanced Drug Delivery Reviews, 1995. **17**(1): p. 103-115.

18. Moghimi, S.M. and A.C. Hunter, *Capture of stealth nanoparticles by the body's defences.* Critical Reviews in Therapeutic Drug Carrier Systems, 2001. **18**(6): p. 527-550.

19. Desai, M.P., et al., *The mechanism of uptake of biodegradable microparticles in Caco-2 cells is size dependent.* Pharmaceutical Research, 1997. **14**(11): p. 1568-1573.

20. Prabha, S., et al., *Size-dependency of nanoparticle-mediated gene transfection: studies with fractionated nanoparticles.* International Journal of Pharmaceutics, 2002. **244**(1-2): p. 105-115.

21. Xu, D.M., et al., *Size-dependent properties of M-PEIs nanogels for gene delivery in cancer cells.* International Journal of Pharmaceutics, 2007. **338**(1-2): p. 291-296.

22. Xu, D.M., et al., *Preparation of polyethyleneimine nanogels via photo-Fenton reaction.* Radiation Physics and Chemistry, 2007. **76**(10): p. 1606-1611.

23. Mintzer, M.A. and E.E. Simanek, *Nonviral Vectors for Gene Delivery.* Chemical Reviews, 2009. **109**(2): p. 259-302.

24. Chithrani, B.D., A.A. Ghazani, and W.C.W. Chan, *Determining the size and shape dependence of gold nanoparticle uptake into mammalian cells.* Nano Letters, 2006. **6**(4): p. 662-668.

25. Cho, E.C., et al., *The Effects of Size, Shape, and Surface Functional Group of Gold Nanostructures on Their Adsorption and Internalization by Cells.* Small, 2010. **6**(4): p. 517-522.

26. Rasband, W.S., *ImageJ 1.42q*, NIH.

27. Behr, J.P., *GENE-TRANSFER WITH SYNTHETIC CATIONIC AMPHIPHILES - PROSPECTS FOR GENE-THERAPY.* Bioconjugate Chemistry, 1994. **5**(5): p. 382-389.

28. Haensler, J. and F.C. Szoka, *POLYAMIDOAMINE CASCADE POLYMERS MEDIATE EFFICIENT TRANSFECTION OF CELLS IN CULTURE.* Bioconjugate Chemistry, 1993. **4**(5): p. 372-379.

29. Sonawane, N.D., F.C. Szoka, and A.S. Verkman, *Chloride accumulation and swelling in endosomes enhances DNA transfer by polyamine-DNA polyplexes.* Journal of Biological Chemistry, 2003. **278**(45): p. 44826-44831.

CHAPTER 7

SUMMARY AND FUTURE DIRECTIONS

7.1 Summary

In this dissertation, we have described methods for utilizing nanotechnology for cancer diagnostic and therapeutic applications. In Chapter 1 we gave an overview of cancer as a genetic disease with enormous complexity. This genetic nature calls for improved methods for the analysis of nucleic acids and delivery of nucleic acid drugs. We proposed nanotechnology as a tool that provides tremendous opportunity for addressing this need for both its ability to interact with biological systems at the molecular level as well as for the unique properties exhibited by materials at this length scale.

In Chapter 2, we continued discussing nanotechnology in more detail, giving some background on both quantum dots as well as iron oxide nanoparticles. We also gave background on the specific applications to be explored in the subsequent chapters, namely nucleic acid detection and oligonucleotide delivery.

Chapter 3 presented a method to semi-quantitatively detect a cancer-associated DNA sequence in solution using a sandwich assay involving quantum dots bound onto single magnetic microbeads. We were able to demonstrate sensitivity down to femtomolar values.

In Chapter 4, we showed that we could prepare different amine-coated SPIONs using EDC reaction. We showed that we could conjugate amine molecules onto carboxyl-coated SPIONs and monitored reaction progress by measuring zeta

potential. Conjugated particles were stable and discrete, demonstrated by their hydrodynamic diameters being unchanged from their preconjugated forms. Further, they remained stable even after addition of negatively-charged oligonucleotides. Gel binding studies indicated that all particles had oligonucleotide binding capacities of at least 50 DNA/SPION.

In Chapter 5, we demonstrated the efficacy of amine-coated iron oxide nanoparticles for the intracellular delivery of antagomirs against miR-222. From the panel of 12 particle coatings that were tested, we found that those containing imidazole were superior to those containing 3A or DPTA. In fact, it appeared that increasing imidazole content resulted in increasing gene knockdown, with 100% imidazole showing the best miR-222 antagonism, of around 75%. Imaging studies showed that particles were able to enter cells and become sequestered in endosomal compartments. They were able to rupture endosomes, presumably through the proton-sponge effect, but did not appear to leave the endosomes themselves. Instead, the antagomirs appeared to dissociate from their nanoparticle carriers and escape alone into the cytosol.

We investigated the effect of nanoparticle size on antagomir transfection into cells in Chapter 6. Our results indicated that smaller particles may achieve greater gene knockdown: both 40 nm and 80 nm SPIONs were able to achieve a statistically significant decrease in miR-222 expression, with 40 nm particles performing better than 80 nm particles. Larger particles such as our 150 nm and 200 nm particles were not able to achieve a detectable knockdown in miR-222 at all. TEM data suggested that larger particles such as the 200 nm SPIONs may not be able to enter cells efficienty as several of these particles remained bound to the cell membrane as long as 24 hours post-transfection. This was not observed for the smaller particles.

Fluorescence imaging experiments using FLNA confirmed transfection data, with only 40 nm and 80 nm particles exhibiting signal indicating that antagomirs had detached from their nanoparticle carriers.

7.2 Future Directions

Improving Sensitivity Limit of Bead-Based Nucleic Acid Detection

Our study utilizing MMBs and QDs to detect DNA in solution was able to achieve sensitivity down 200 fM. This is quite remarkable considering that the QD coatings were considerably negatively charged, as evidenced by their migration down the gel in electrophoresis experiments, even without incubation to DNA (lane '0' in Figure 3.2). Previous studies have shown that charged QD coatings exhibit significantly more nonspecific binding than uncharged QD coatings [1]. This may partially explain the existence of some signal even in samples where no target DNA was added (Figure 3.4C).

In the study, we used approximately 200,000 magnetic beads per detection assay and were able to detect DNA at 200 fM sensitivity. This translates into a detection sensitivity of approximately 100 target DNA per MMB. The sensitivity limit may therefore also be improved by using fewer MMBs per assay.

Multiplexed Biomolecule Detection Using MMBs

We have demonstrated detection of only target DNA using one color of QD. One advantage of QDs, however, is multiplexing as they can be made in multiple colors and have broad absorption spectra combined with narrow emission spectra

[2]. Future work, therefore may investigate the use of multicolored quantum dots for multiplex detection of a panel of CNA markers.

Alternatively, surface-enhanced Raman spectroscopy (SERS)-active gold nanoparticles can be used instead of QDs. SERS-active particles exhibit even greater sensitivity than QDs and have narrower spectra, enabling greater multiplexing potential [3, 4]. Furthermore, similar experiments have been performed to detect proteins using MMBs and QDs [5]. Multplexing studies could thus be performed to examine the use of this assay for the simultaneous detection of both DNA and protein biomarkers.

SPION Delivery of Nucleic Acids

While we have identified imidazole as a superior amine molecule for delivery of oligonucleotides, studies need to be performed to investigate further the differences in performance between imidazole and non-imidazole containing particles as the exact reason for this observed performance difference is yet unclear. It may be due to the chemical properties of imidazole, with its relatively lower pK_a and thus improved proton buffering ability and lower cationic charge at neutral pH. These properties may render imidazole an enhanced ability to rupture endosomes through the proton sponge effect or to release antagomirs into the cell relative to its higher pK_a counterparts.

Studies may also explore the use of other amine molecules with other pK_a values for oligonucleotide delivery. The current study demonstrated that imidazole was superior to tertiary amines and DPTA; however this does not mean that imidazole is the optimal amine molecule. Other amine molecules can be synthesized to represent other pK_as, both lower and slightly higher than that of imidazole.

Particles coated with 100% of each of these amines could be tested and evaluated for gene knockdown efficiency.

We also demonstrated in this dissertation that smaller particles perform better than larger particles for oligonucleotide transfection. The smallest particle used, however, was 40 nm in hydrodynamic diameter. It would thus be interesting to test particles even smaller than this to evaluate their transfection efficiencies. In Appendix A, we describe the use of quantum dots of approximately 25 nm in hydrodynamic size. These particles exhibited antagonism of around 90%, which is superior to the 40 nm SPIONs. This difference, however, may not be attributed to size alone as the particles also had different starting surface chemistries (i.e. polyglucuronic acid coating for SPIONs and polymaleic anhydride coating for QDs).

In Vivo Delivery

The ultimate goal of oligonucleotide delivery is to enable clinical application of these promising new drugs. The in vivo biological environment, however, is much more complex than the in vitro one that was studied here. Successful in vivo delivery will have to address many complex issues such as blood-nanoparticle interactions, immune response, biodistribution, pharmacokinetics, and toxicity. While SPIONs are currently approved for use in the clinic, the use of a different polymer coating (polyglucuronic acid coating versus polydextran for FDA-approved SPIONs) may imply different biological behavior and will thus need to be studied.

Lastly, other useful properties of iron oxide nanoparticles such as their ability to be used for therapy by hyperthermia or for imaging by MRI were discussed in Chapter 2 of this dissertation but did not fall within the scope of this study. The

potential for multifunctionality by these drug delivery vehicles is a major advantage and should be explored in future work.

7.3 References

1. Kairdolf, B.A., et al., *Minimizing nonspecific cellular binding of quantum dots with hydroxyl-derivatizied surface coatings.* Analytical Chemistry, 2008. **80**(8): p. 3029-3034.

2. Smith, A.M., et al., *Multicolor quantum dots for molecular diagnostics of cancer.* Expert Review of Molecular Diagnostics, 2006. **6**(2): p. 231-244.

3. Zavaleta, C.L., et al., *Multiplexed imaging of surface enhanced Raman scattering nanotags in living mice using noninvasive Raman spectroscopy.* Proceedings of the National Academy of Sciences of the United States of America, 2009. **106**(32): p. 13511-13516.

4. Qian, X.M. and S.M. Nie, *Single-molecule and single-nanoparticle SERS: from fundamental mechanisms to biomedical applications.* Chemical Society Reviews, 2008. **37**(5): p. 912-920.

5. Agrawal, A., T. Sathe, and S.M. Nie, *Single-bead immunoassays using magnetic microparticles and spectral-shifting quantum dots.* Journal of Agricultural and Food Chemistry, 2007. **55**(10): p. 3778-3782.

APPENDIX A

ANTAGOMIR DELIVERY AND REAL-TIME OPTICAL IMAGING USING AMINE-COATED QUANTUM DOTS

A.1 Introduction

We have included this appendix to give further data on intracellular antagomir delivery by nanoparticles, this time with quantum dots. The QDs are coated with an amine polymer that enables both antagomir binding and intracellular release. The QD core enables real-time tracking of delivery and allows optical visualization in live cells. Real-time PCR indicated miRNA knockdown of nearly 90%.

A.2 Methods

Materials

Agarose, octadecene (ODE; 90%), octadecylamine (ODA), poly(maleic anhydride-alt-1-octadecene) (Mn 7300 Da), *N,N*-dimethyldipropylenetriamine (DPTA), 4-(dimethylamino)pyridine (DMAP), and fluorescein-labeled oligonucleotide were purchased from Sigma. LNA-modified oligonucleotides were purchased from Integrated DNA Technologies (Coralville, IA).

Quantum Dot Synthesis

Cadmium selenide QDs of diameter 4.5 nm were synthesized in a coordinating solvent following previously published procedures [1]. After purification via precipitation from methanol, the QDs were resuspended in a mixture of ODE and ODA, and then capped with a shell of CdS (2 monolayers) and then ZnS (2

monolayers) at 230C under argon, using organometallic precursors [2-4]. These ODA-passivated QDs were stored as a crude mixture at 4C and purified using repeated extractions in hexane–methanol, followed by precipitation with acetone prior to use.

Quantum Dot Water Solubilization

Poly(maleic anhydride-alt-1-octadecene) was reacted with DPTA with DMAP as a catalyst overnight at room temperature. The reacted polymer was precipitated in acetone and isolated by evaporation. Reacted polymer was mixed with QDs (1000:1 molar ratio) in chloroform for six hours, after which the solvent was evaporated under a slight vacuum. The dried film was resuspended in borate buffer, ultracentrifuged to remove excess polymer, and then stored at 4C in the dark.

QD-Nucleic Acid Complexing

QDs encapsulated with DPTA-modified polymer were complexed with nucleic acids by mixing and then incubating for 1 hour at 4C. For DNA binding studies, QDs were complexed with fluorescein-labeled oligonucleotide by incubating in water. For cell imaging and transfection studies, QDs were complexed with LNA by incubating in Opti-MEM.

DNA Binding Assay

QDs were complexed with dye-labeled oligonucleotide as described above. All samples contained 0.675 nmol of dye-labeled oligonucleotide and the QD concentration was varied. The samples were added to a 0.8% agarose gel supplemented with 0.1% Tween-20 in 1X MOPS buffer. Electrophoresis was

performed for 20 min at 105 V with the gel wells near the anode. Gels were imaged with a UV macro-imaging system.

Cell Imaging and Transfection

PC-3 cells (ATCC, Manassas, VA) were cultured in RPMI-1640 supplemented with 10% fetal bovine serum at 37C and 5% CO_2.

For imaging studies, cells were plated in full medium in LabTek II chamber slides and grown for 24 hours to about 20% confluency. The following day, media was removed, the cells were rinsed once with 1X PBS and incubated with either PEI-LNA or QD-LNA complexes in Opti-MEM at 37C. Cells were then imaged with a Nikon epifluorescence microscope using 488 nm laser excitation, a long pass filter, and a CCD camera.

For cell transfection, cells were plated in a 96-well format and grown for 24 hours to 60-80% confluency. Media was then removed and the cells rinsed with 1X PBS. Either PEI-LNA or QD-LNA complexes in Opti-MEM were then added and the cells incubated at 37C. The PEI-LNA or QD-LNA solution was removed after 4 hours. Cells were then rinsed again with 1X PBS and incubated in regular culture medium at 37C. Short RNA was isolated twenty-four hours after LNA addition using the miRvana RNA Isolation Kit (Ambion, Austin, TX). RNA purity and concentration were quantified on a spectrophotometer (Shimadzu UV-2401PC, Kyoto, Japan). Cells were transfected in triplicate.

RNA samples were reverse transcribed using the TaqMan MicroRNA Reverse Transcription Kit according to the manufacturer's instruction (Applied Biosystems, Foster City, CA). Real-time PCR was then performed using the Taqman MicroRNA assay (Applied Biosystems, Foster City, CA).

A.3 Results and Discussion

Nanoparticle Synthesis and Characterization

The QDs prepared for this study had a core-shell structure of CdSe/CdS/ZnS. These particles have been shown to be highly luminescent and have greater photostability than CdSe cores, CdSe/CdS core/shells, and CdSe/ZnS QDs, presumably due to improved lattice matching between the highly-strained CdSe core and ZnS shell with interim layers of CdS [2, 3, 5, 6]. These QDs were roughly 6.5 nm in diameter, with a fluorescent emission peak at 630 nm (Figure 1), 24 nm full-width-at-half maximum, nearly 80% quantum yield, and were passivated by octadecylamine [7].

QDs were then coated with a monolayer of an amphiphilic polymer to render them water-soluble. Fifty percent of the exposed hydrophilic groups was composed of carboxylic acid and the other fifty percent was composed of DPTA. Figure 1 shows the structure of the polymer along with a transmission electron micrograph and dynamic light scattering (DLS) data of the polymer-coated QD. The particles had a diameter of roughly 18nm by DLS. There was a correlation between the size of the QDs on TEM grids and their size from DLS measurements, but this relationship was not quantitative, most likely due to the fact that nanoparticles and their surrounding polymers adopt different conformations when spread and dried as thin films, compared to those in aqueous solution. This is also undoubtedly as a result of the fundamental difference between nanoparticle hydrodynamic size measured by DLS and the electron density observed in TEM. Zeta potential measurements indicated the particles had a surface charge of +10 mV at around neutral pH. Although half of the surface functional groups are carboxylic acids,

which should be negatively charged, each DPTA moiety contributes a secondary amine, which should be positively charged, and a tertiary amine. The positive surface charge may be a result of the equilibrium of protonated and unprotonated groups—most but not necessarily all of the carboxylic acids may be deprotonated—and of the proximity of the various groups to the surface—the carboxyl groups are more buried within the surface whereas the amines are located further out on the surface.

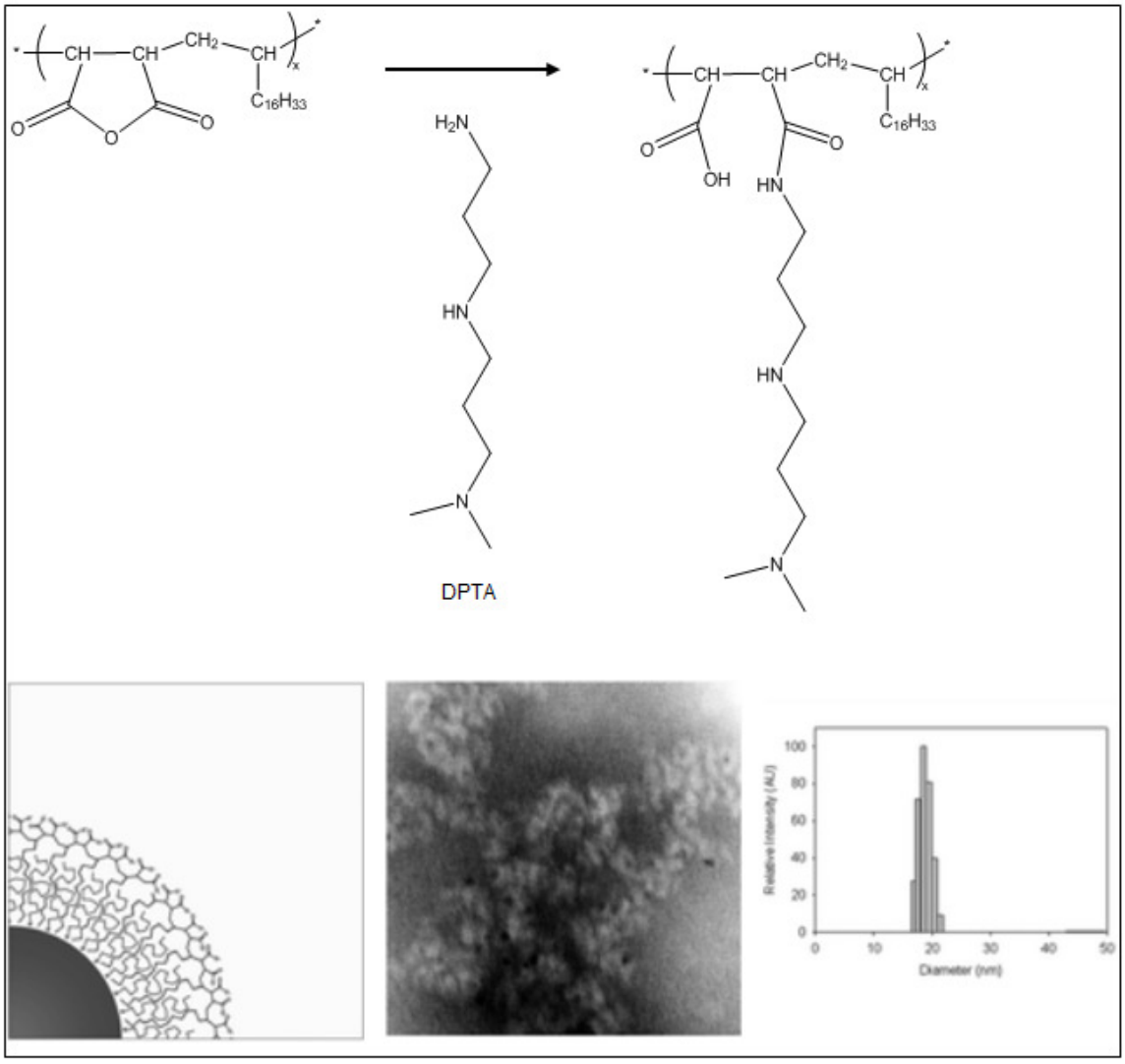

Figure A.1: Reaction of QD polymer coat and characterization of coated QDs.

Nucleic Acid Delivery

The balance of functional groups is very important for nanoparticles to overcome the three key challenges to the cellular delivery of nucleic acids. First, nanoparticles have to bind to the nucleic acid; second, they must transport the nucleic acid into the cell cytoplasm; and third, they must release the nucleic acid. We overcame the first obstacle by rendering our particles positively charged, thus allowing electrostatic binding to nucleic acids through their negatively charged

phosphate groups. Because we were interested in the delivery of short nucleic acids such as siRNA and antisense, we tested binding of our QDs to a 13-base pair strand of DNA. Various ratios of QD:DNA were tested from 1:100 to 1:1 and imaged via gel electrophoresis (Figure 2). As we increased the relative amount of QDs, we saw increased binding of the DNA until the QD surface was saturated at a 1:2 ratio. There was no observable enhancement of DNA binding when the ratio was increased to 1:1. Interestingly, while the QDs were positively charged, they did not migrate toward the negative electrode but instead remained in the loading well, possibly due to the large size of these particles.

Figure A.2: Gel electrophoresis assay showing oligonucleotide loading onto amine-coated QDs. Ratios indicate DNA:QD feed ratios.

We next wanted to examine the ability of QDs to enter cells. One of the advantages of using a quantum dot as a core nanoparticle is the ability to track delivery via fluorescence. PC-3 cells were incubated with 20nM concentration of QDs and images were taken at varying time points (Figure 3). Twenty nM was chosen because we wanted to use the concentration that gives a 1:2 QD:LNA ratio, which would be half the typical LNA concentration in anti-miR experiments, 40nM. QDs were observed to bind to the surface of the cell at 15min post incubation. This may be due to electrostatic interactions between the positive surface charge of the QDs and the negative charge of the cell membrane conferred by its phospholipids. After one hour, some of the nanoparticles appear to be localized in the interior of the cell but there is still strong fluorescence on the cell border. At 3 hours, almost all of the nanoparticles are inside the cell and fluorescence around the cell membrane is no longer observed. Fluorescence of the intracellular QDs at 3 hours are punctate in appearance, suggesting that they are localized in endosomes. It is worthy to note that no membrane-specific ligands are attached to the QDs and hence they are nonspecifically endocytosed. Nevertheless, a significant amount of QDs appear to be uptaken by the cells.

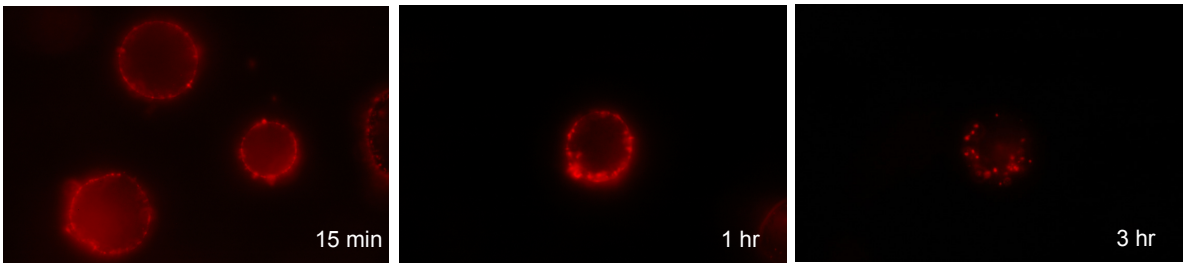

Figure A.3: Fluorescence imaging of PC-3 cells transfected with QD-antagomir complexes.

To check the final step of nucleic acid release, and to verify that our nanoparticles can be used for delivery of nucleic acids, we delivered an LNA sequence designed to knockdown miR-222 in PC-3 cells using QDs, and assayed knockdown of the microRNA using real-time PCR. Figure 4 shows that we are able to obtain close to 90% knockdown of the miRNA target with the QDs whereas only 60% knockdown is achieved using PEI. Interestingly, increased knockdown is observed with increasing QD concentration. This is in agreement with our gel electrophoresis data indicating that only at a 1:2 QD:DNA ratio is all the DNA bound to the QD. Also in agreement, there is no statistically significant improvement in knockdown at a ratio of 1:1.

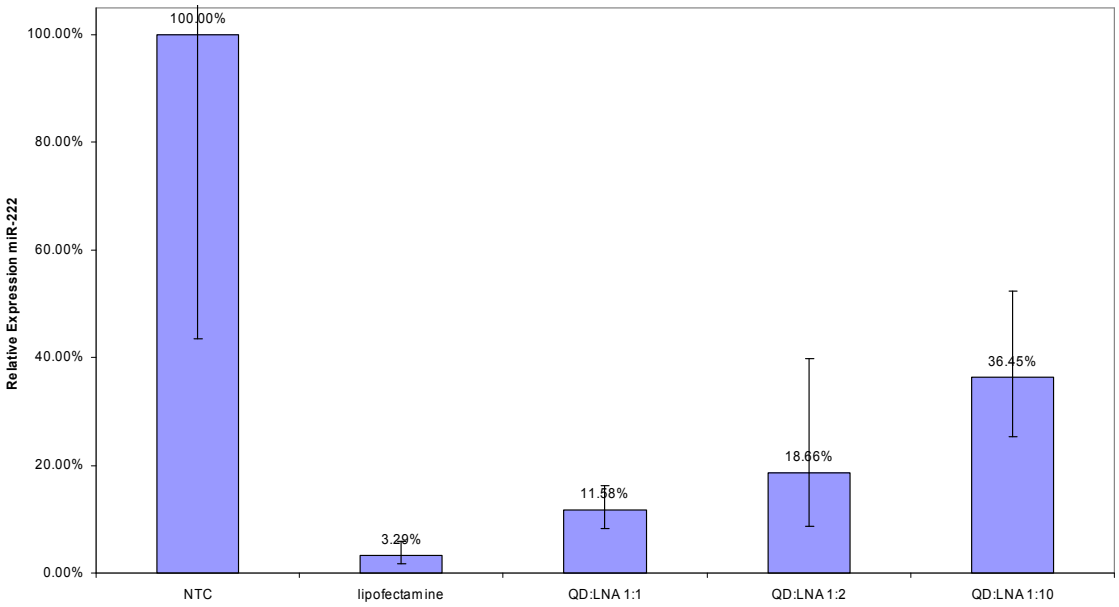

Figure A.4: Real-time PCR data showing miR-222 expression after tranfection of antagomir-QD complexes.

Our imaging studies indicated that upon cellular uptake, our QDs were localized in endosomes; however, our transfection experiments indicated that the LNA was able to enter the cytosol, where it could then interact with its miRNA targets. We believe the LNA enters endosomes with the QDs but then escape into the cytosol via the proton sponge effect. The tertiary amines on the DPTA-modified polymer coating should provide pH buffering capacity to achieve this much like the tertiary amines of PEI. The balance of carboxyl and secondary amine groups then provide the necessary binding strength to both attach to and release the LNA at the appropriate locations.

A.4 References

1. Qu, L.H. and X.G. Peng, *Control of photoluminescence properties of CdSe nanocrystals in growth.* Journal of the American Chemical Society, 2002. **124**(9): p. 2049-2055.

2. Xie, R.G., et al., *Synthesis and characterization of highly luminescent CdSe-Core CdS/Zn0.5Cd0.5S/ZnS multishell nanocrystals.* Journal of the American Chemical Society, 2005. **127**(20): p. 7480-7488.

3. Talapin, D.V., et al., *CdSe/CdS/ZnS and CdSe/ZnSe/ZnS core-shell-shell nanocrystals.* Journal of Physical Chemistry B, 2004. **108**(49): p. 18826-18831.

4. Li, J.J., et al., *Large-scale synthesis of nearly monodisperse CdSe/CdS core/shell nanocrystals using air-stable reagents via successive ion layer adsorption and reaction.* Journal of the American Chemical Society, 2003. **125**(41): p. 12567-12575.

5. Manna, L., et al., *Epitaxial growth and photochemical annealing of graded CdS/ZnS shells on colloidal CdSe nanorods.* Journal of the American Chemical Society, 2002. **124**(24): p. 7136-7145.

6. Bleuse, J., S. Carayon, and P. Reiss, *Optical properties of core/multishell CdSe/Zn(S,Se) nanocrystals.* Physica E-Low-Dimensional Systems & Nanostructures, 2004. **21**(2-4): p. 331-335.

7. Smith, A.M., et al., *A systematic examination of surface coatings on the optical and chemical properties of semiconductor quantum dots.* Physical Chemistry Chemical Physics, 2006. **8**(33): p. 3895-3903.

VITA

CHRISTOPHER SHEN

Christopher Shen was born in Taipei, Taiwan. He moved with his family to Guam at the age of four, where he attended preschool. He moved again with his family to Sacramento, California at age five where he lived until graduating from Rio Americano High School. He received his B.S. with high honors in Bioengineering from the University of California, Berkeley in 2003. He joined the Wallace H. Coulter Department of Biomedical Engineering in August 2005 to pursue a doctoral degree in the joint program at Georgia Tech and Emory University. He holds a certificate in technology commercialization from the Georgia Tech College of Management through the TI:GER (Technology Innovation: Generating Economic Results) program.